THE EFFECT OF DEFORMATION RATE ON THE DAMAGE TOLERANCES OF NOMEX HONEYCOMB CORED COMPOSITE SANDWICHES

**A Thesis Submitted to
the Graduate School of
İzmir Institute of Technology
in Partial Fulfillment of the Requirements for the Degree of**

MASTER OF SCIENCE

in Mechanical Engineering

**by
Muhammet ÇELİK**

June 2021

İZMİR

ACKNOWLEDGMENTS

ABSTRACT

THE EFFECT OF DEFORMATION RATE ON THE DAMAGE TOLERANCES OF NOMEX HONEYCOMB CORED COMPOSITE SANDWICHES

The impact response and damage tolerance of E-glass/epoxy faces and Nomex honeycomb core sandwich were determined experimentally at different velocities (0-40 ms^{-1}). Concentrated quasi-static indentation force (CQIF), low-velocity impact (LVI) and high-velocity impact (HVI) tests were performed sequentially using a universal test machine, a drop weight tester and a modified Split Hopkinson Pressure Bar system using a hemispherical indenter with a diameter of 16 mm. Velocity was increased by reducing the mass of the indenter in HVI. HVI was performed at the same impact energies (3-33 J) as LVI. Although CQIF and LVI showed similar damage modes, front face damage initiation and perforation occurred at higher energies in LVI, which was ascribed to the rate sensitivity of the face material. When the front face was penetrated at 10 J, residual strength was found to reduce 60%. The flexural waves and core shear were observed to become dominant above 40 J. Barely visible damage was identified below 10 J with a dent depth less than 1 mm, the damage area less than 50 mm^2 and an NRS of ~0.8. Visible damage occurred between 50-400 mm^2 damage areas when the front face was perforated (10-39 J). Discrete source damage was detected between 400-800 mm^2 where full-penetration and core shear occurred (>40 J). Although damage areas in HVI were smaller than those of LVI at the same energies, compression after impact tests showed almost no effect of velocity on NRS, except HVI tested coupon showed a slightly higher mean NRS at 5.5 J.

ÖZET

NOMEX BAL PETEĞİ DOLGULU KOMPOZİT SANDVİÇLERDE DEFORMASYON HIZININ HASAR TOLERANSINA ETKİSİ

E-cam/epoksi yüzey tabakalı ile Nomex bal peteği dolgulu sandviç yapının çarpma tepkisi ve hasar toleransı farklı çarpma hızlarında (0-40 ms^{-1}) deneysel olarak belirlendi. 16 mm çaplı yarı küre darbe ucu kullanılarak statik-eşdeğer delme, düşük hızlı çarpma (DHÇ) ve yüksek hızlı çarpma (YHÇ) testleri, sırasıyla konvansiyonel test cihazı, düşen ağırlık test cihazı ve modifiye edilmiş split-Hopkinson Basınç Bar sistemi kullanılarak gerçekleştirildi. YHÇ'lerde çarpma ucun kütlesi düşürülerek hız arttırılmıştır. YHÇ, DHÇ ile aynı enerjirinde gerçekleştirilmiştir (3-33 J).YSD ile DHÇ testleri benzer hasarlar sergilerken ön yüzey tabakasındaki malzemenin hız duyarlılığından dolayı YHÇ testlerinde çarpma yüz tabakasında hasar başlangıcı ve delinmesi daha yüksek enerjilerde gerçekleşir. 10 J'de ön yüzey tabakasının delinmesiyle artık dayanımın %60 azaldığı bulunmuştur. 40 J'nin üzerinde, eğilme dalgaları dolguda boyuna kesme etkileri baskın hâle geldiği gözlemlenmiştir. 10 J'nin altı 1 mm'den az göçük derinliği, 50 mm^2'den az hasar alanı ve ~0.8'lik normalleştirilmiş artık dayanımı (NAD) sergilediğinden zor görülebilen hasar olarak tespit edildi. Görünür çarpma hasarı 10-39 J'de ön yüzey delinerek 50-400 mm^2 hasarla gerçekleşir. 400-800 mm^2 arasındaki hasar, tam delinmenin ve dolguda kesmelerin gerçekleştiği (>40 J) ayrı kaynak hasarı olarak bulundu. YHÇ'deki hasar alanları, aynı enerjilerde DHÇ'ninkinden daha küçük olmasına karşın, çarpma sonrası basma testleri, YHÇ test kuponunun 5.5 J'de biraz daha yüksek NAD göstermesi dışında, hızın NAD üzerine neredeyse hiç etkisi olmadı.

TABLE OF CONTENTS

LIST OF FIGURES

LIST OF TABLES

CHAPTER 1

INTRODUCTION

1.1. Introduction

The transportation sector is the second-largest energy consuming business sector and also the source of CO_2-emission, according to a report published by European Commission (2020) (Figures 1.1a and 1.1b)[1]. In parallel with this, the use of light weight materials and their constructions in diverse industries have recently been increased significantly to reduce energy consumption and CO_2-emission. The currently available light weight materials and structures are shown in Figure 1.2, which is the well-known Ashby's strength-density chart of engineering materials. As is seen in the same figure, the group of structures, so-called cellular structures, including foams, lattices and honeycombs, are the lightest, but at the same time, the weakest ones among engineering materials. Cellular structures are particularly too weak to be used in their monolithic forms. However, when used as cores between two light weight composite face sheets such as fibre-reinforced plastic composite (FRPC) in sandwich structures, they increase the thickness of the structure, making the structure more resistant to bending loads and more mass-efficient as compared with monolithic counterparts. Sandwich construction is one of the widely used methods of reducing the weight of structural parts[2].
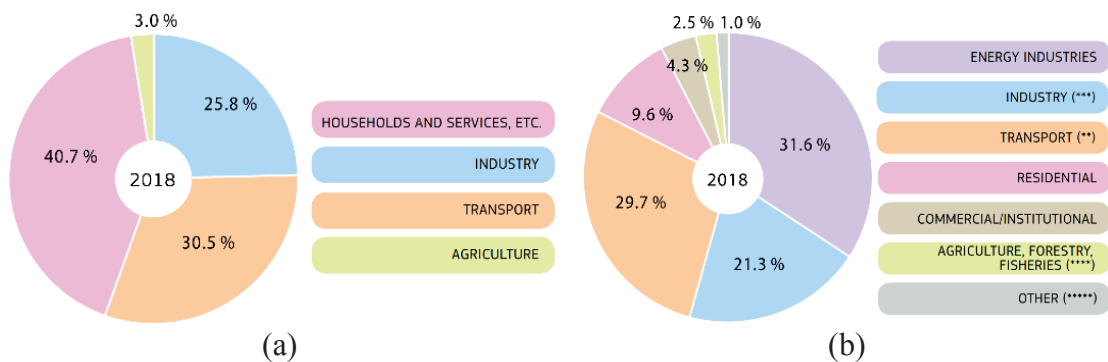
Figure 1.1. (a) The energy consumption[1] and (b) CO_2-emission in Europe[1]
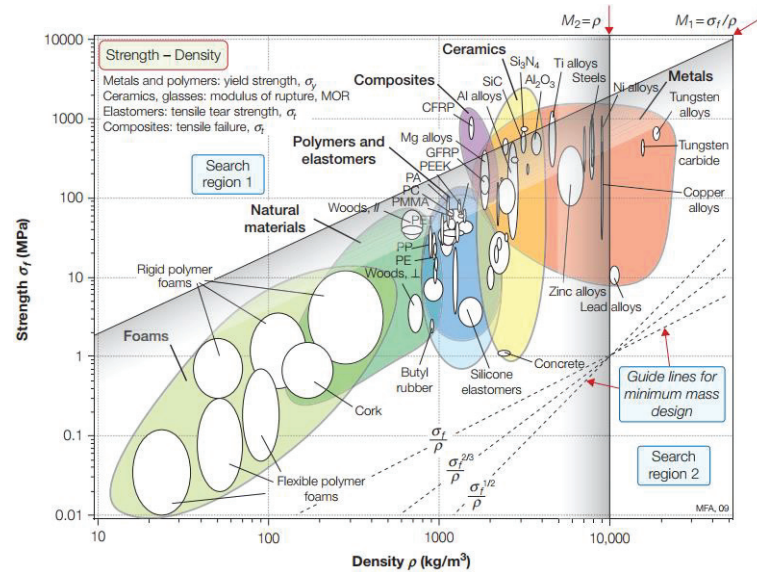
Figure 1.2. The strength-density chart of engineering materials[3]

The initial use of composite structures in the aerospace industry was limited to non-critical structural components. The research results focused on improving overall global response have made composites the primary choice for critical applications. An example of the composite sandwich structure is the Nomex honeycomb/FRPC sandwich, it has been widely used in the aerospace, defense and automotive industries as structural components due to its high stiffness-to-weight ratio, excellent corrosion resistance and good thermal insulation properties and fatigue resistance.[4]

A particular use of the Nomex honeycomb/FRPC sandwich is in the airborne radome (radar dome).[5] The radome body skin (Figure 1.3) should protect radar antenna from environments such as weather and big aerodynamic loads, and at the same time, it should be transparent to microwaves.[6] The Nomex honeycomb/FRPC sandwich is an appropriate structure to be used in the radome body skin.[5] The strong composite face sheets provide rigidity to the body skin, and the Nomex honeycomb provides resistance to bending loads. Both the composite face sheets and Nomex honeycomb are also transparent to microwaves. The radome body skin may be exposed to impact loads from hailstone, bird and foreign objects. The common way of determining the impact response of these structures is to apply a low-velocity impact (LVI) test based on the ASTM D7136 / D7136M - 20: *Standard Test Method for Measuring the Damage Resistance of a Fiber-Reinforced Polymer Matrix Composite to a Drop-Weight Impact Event*[7]. The impact velocities in LVI tests are relatively low (1-5 ms^{-1}) as compared with those in actual

impact events. However, there have been limited work in the literature on the impact resistance of such sandwiches at the velocities higher than those in the LVI tests. One reason for that is the lack of a suitable impact test method at these velocities. The primary aim of this thesis is to determine the impact resistance and damage tolerance of a Nomex honeycomb/Glass FRPC sandwich at the velocities in the LVI test and also at the velocities higher than those of LVI tests. The thesis also seeks to develop a high-velocity impact (HVI) test method for sandwiches and composite plates by keeping the same impact energies with the LVI tests.
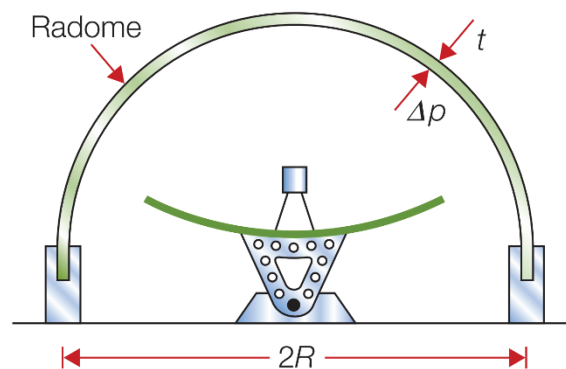
Figure 1.3. The schematic of radome [8]

1.2. Sandwich Structure

1.2.1. Structure

A sandwich structure is similar to an I-beam (Figure 1.4a and 1.4b). The face sheets carry bending loads just like the flanges of the I-beam, and the core carries shear loads like the web of the I-beam.[9] [10] [11] The core-to-face sheet adhesive provides integrity with superior torsional and bending rigidity. Three directions are noted in a sandwich structure: the in-plane Length (L), the Width (W) directions, and the out-of-plane (T). Typical cores for sandwiches include web, honeycomb, foam and wood (Figure 1.4c).
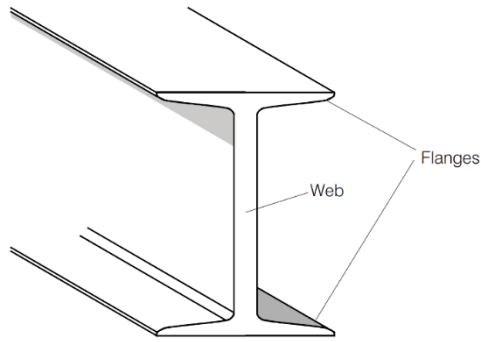
(a)
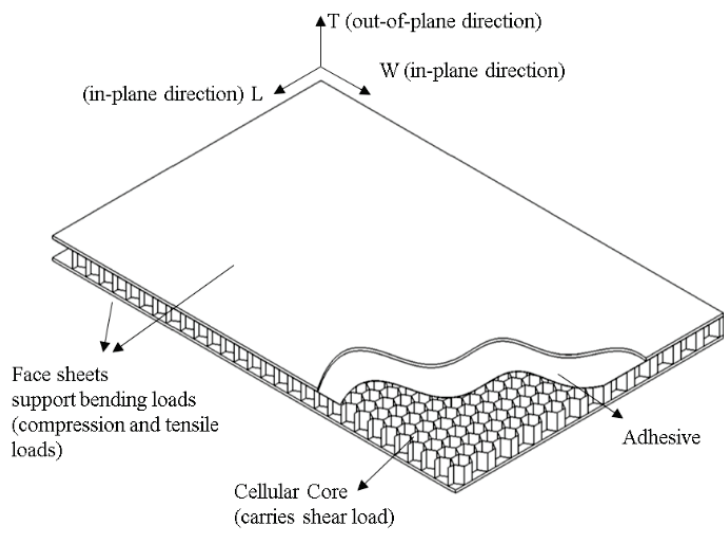
(b)
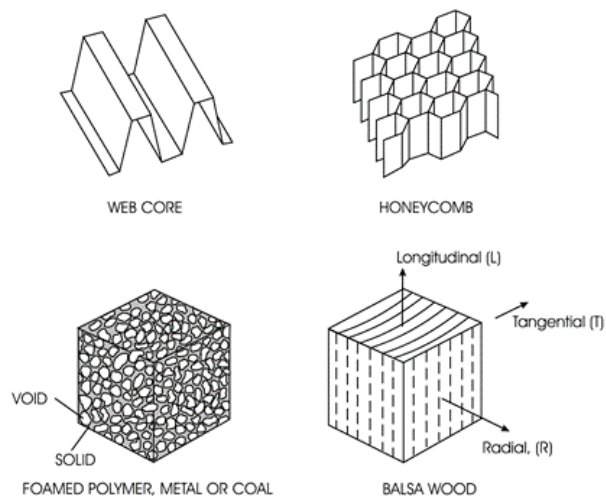
(c)

Figure 1.4. (a) I-beam[10] (b) the sandwich structure, and (c) core types [12]

4

1.2.2. Nomex Honeycombs

The modern honeycomb core (HC) has been produced since the 1930s and made of metallic (i.e. aluminium, stainless steel, titanium) or non-metallic (i.e. fiberglass, Nomex, Kraft paper) materials.[13] [14] Nomex honeycomb core (NHC) has superior mechanical properties and physical properties (such as flame retardant and thermal insulation), making them the focus of research in the 2000s. Therefore, there are many studies on the mechanical properties of NHC (elastic properties, bending, crushing, buckling and yield behaviour), compressive strength in the in-plane and out-of-plane directions, and impact resistance.[4] NHC's geometric parameters and directions are shown in Figure 1.5. The XY-plane in this figure is referred to as the in-plane properties of the HC; the y-direction contains out-of-plane properties; the x-direction is called the ribbon or length direction, and the z-direction is called the core thickness direction. The strongest stiffness and strength are found in the out-of-plane direction, and the weakest properties are in the in-plane direction.[15] The strength and young moduli of the ribbon are higher than the width direction (Figures 1.6a and 1.6b). The size of the core influences the elastic moduli of NHC.[16] In-plane elastic properties depend on the corner angle and the ratio of wall thickness to length.[17] Wall thickness affects the in-plane properties of the NHC.[18] The density to the size of cells ratio affects the in-plane and out-of-plane NHC strengths.[19] The adhesives between the double cell wall play a role in the out-of-plane strength.[20] Simultaneously, the resin coating volume increases the collapse strength of the NHC, which decreases collapse strain.[21] NHC subjected to the combined shear-compression loads indicates two failures: the plastic buckling and extension fracture of the cell wall.[22] The out-of-plane compression strength depends on the strain rate property of the phenolic resin and the inertial stabilization of the NHC walls.[23] Buckling properties of NHC depend on boundary conditions.[24]
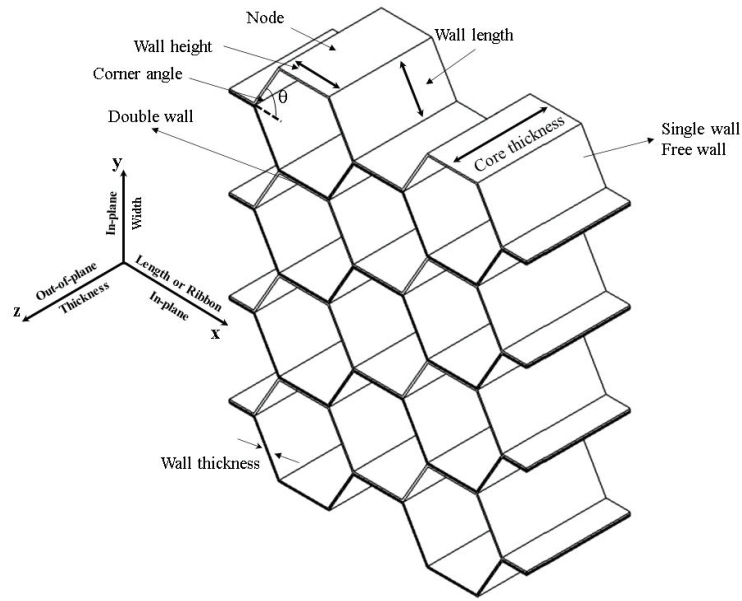
Figure 1.5. NHC's geometric parameters

<div align="center">(a)</div>

<div align="center">(b)</div>
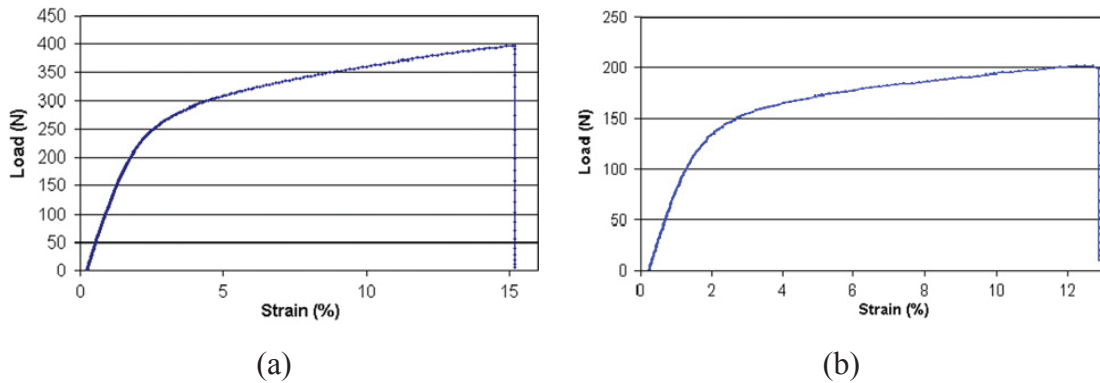
Figure 1.6. (a) ribbon tensile strength[16] and (b) transverse tensile strength of NHC[16]

Figure 1.7a shows the typical compressive behaviour of NHC. The curve divided into four regions. In the region AB, elastic deformation of NHC occurs. The brittle fracture of phenolic resin and/or honeycomb core buckling initiation is seen in the region BC. The energy absorption capacity of NHC is determined by the region CD as the most energy is absorbed in this region. This region is also called the collapse phase/plateau region since the core buckling occurs (Figure 1.7b). After point D, the core collapse finishes (Figure 1.7c), and energy absorption efficiency decreases significantly.[19]

(a)

(b)

(c)
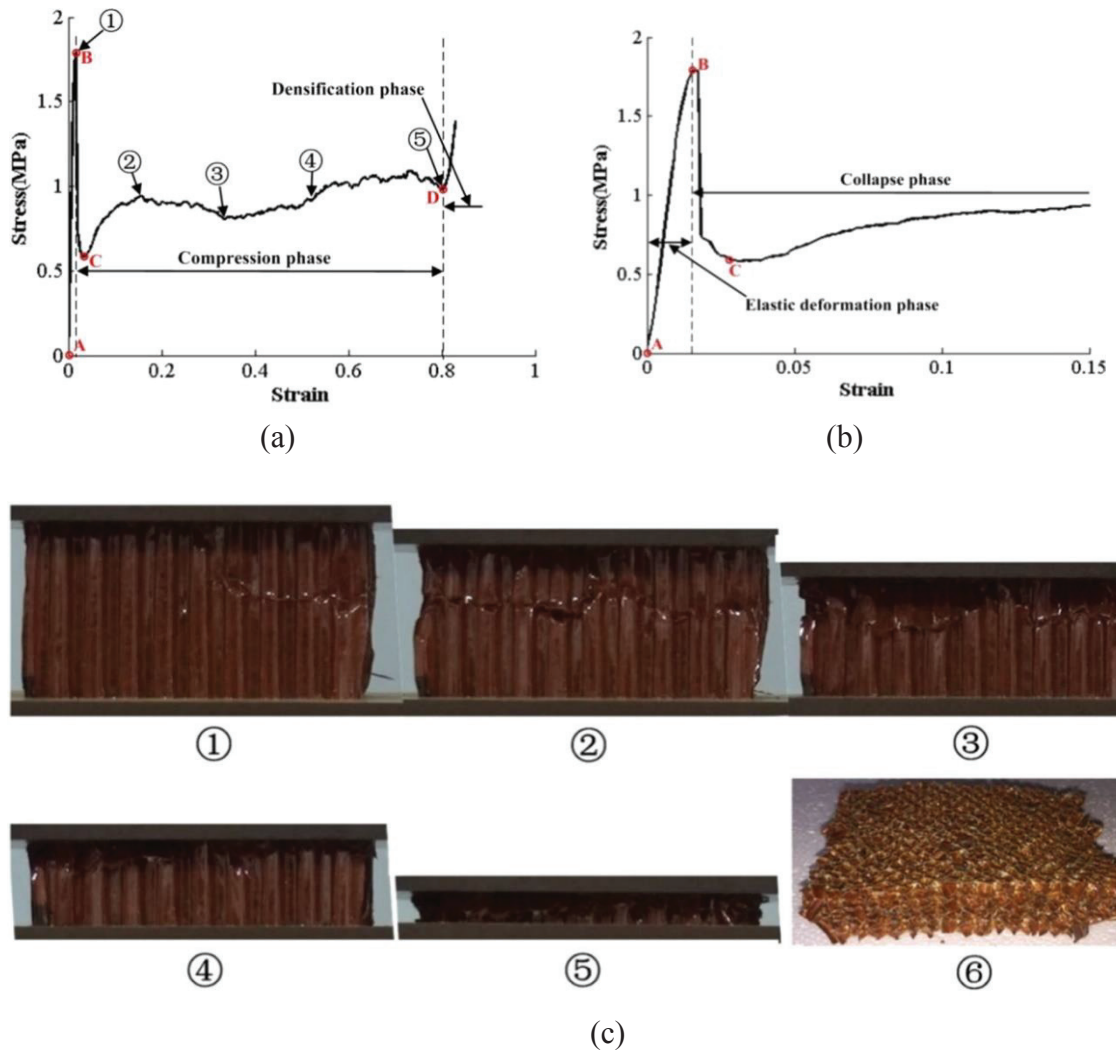
Figure 1.7. Out-of-plane behaviour of NHC (a) stress-strain curve (b) elastic
deformation region on the curve, and (c) core's failure modes under
different load-strain[19]

1.2.3. Honeycomb Manufacturing

There are mainly two methods for HC processing: expansion and corrugation. The corrugation process divided into three stages (Figure 1.8a). Firstly, the sheet of Nomex paper is formed by using corrugating rolls. Then, the stacked corrugated sheets are bonded and cured together. Finally, the corrugated block is processed into the design structure. This method does not include expansion.

In the expansion process, roll paper is cut to the sheets, and adhesive lies on node

lines of the sheets (Figure 1.8b). Then, the sheets are stacked together to form a Honeycomb Before Expansion Block. The Honeycomb Before Expansion Block is cured and cut to design thickness. Finally, the block expands to the designed cell shape. Expansion is a widely used method for the production of aluminium and Nomex honeycomb cores.

(a)

(b)
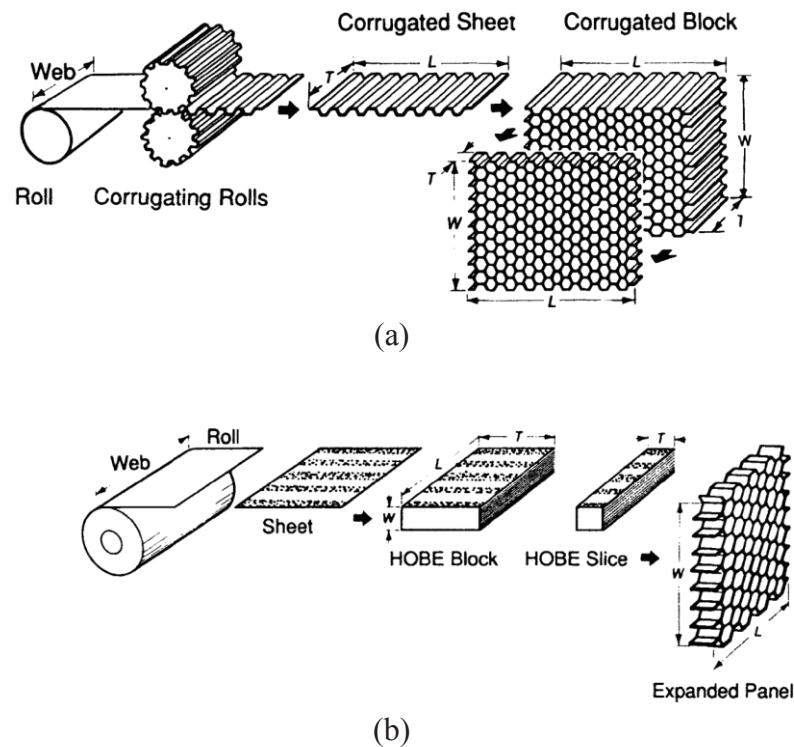
Figure 1.8. (a) Corrugation and (b) expansion manufacturing process [25]

1.2.4. Manufacturing of Sandwich Composite

Open-cell core sandwich structures can be manufactured by two methods: using multiple cure cycles or co-curing techniques in one step. In the multiple cure cycles, composite face sheets are cured first and then face sheets, and the core is bonded using an adhesive. That method is conventional manufacturing and includes complex steps; therefore, the cost is more expensive, and cycle time is high. Also, the sandwich structure manufactured have more defects such as bondline discrepancies and core crushing.

During co-curing techniques, face sheets cured and bonded onto the processed core at the same time. In these techniques, there are many quality issues such as distortion of the plies, matrix porous because of insufficient pressure, dispersion of the resin into open-cells of the core. The quality inspections of sandwich structures produced by this method may be inconvenient to evaluate using non-destructive inspection (NDI).

Still, no manufacturing method contains ideal porosity, the ply distortion, core crushing, resin entering the open-cells etc. A general manufacture method for all cores is also not possible because entering the resin into open-cells depends on many factors such as viscosity of the resin, pressure difference, core surface energy, resin additives etc.[26] Heated press and vacuum bag processing methods are commonly used to manufacture honeycomb sandwich structures. The heated press method is commonly chosen for structures with a flat, simple geometry (Figure 1.9a). Prepreg facing fibers and core may be co-cured by using a press. Also, the adhesive may be used.

Complex parts are manufactured using vacuum bag processing (Figure 1.9b). The fabric stack and the core are sealed using a plastic bag. That is connected at one end to a liquid resin source and at another end to a vacuum pump. Air is extracted, and the sandwich structure takes the shape of the mould. The resin is transferred by the vacuum pump. An oven can be used for curing, and for additional pressure, an autoclave can be used.

(a) (b)
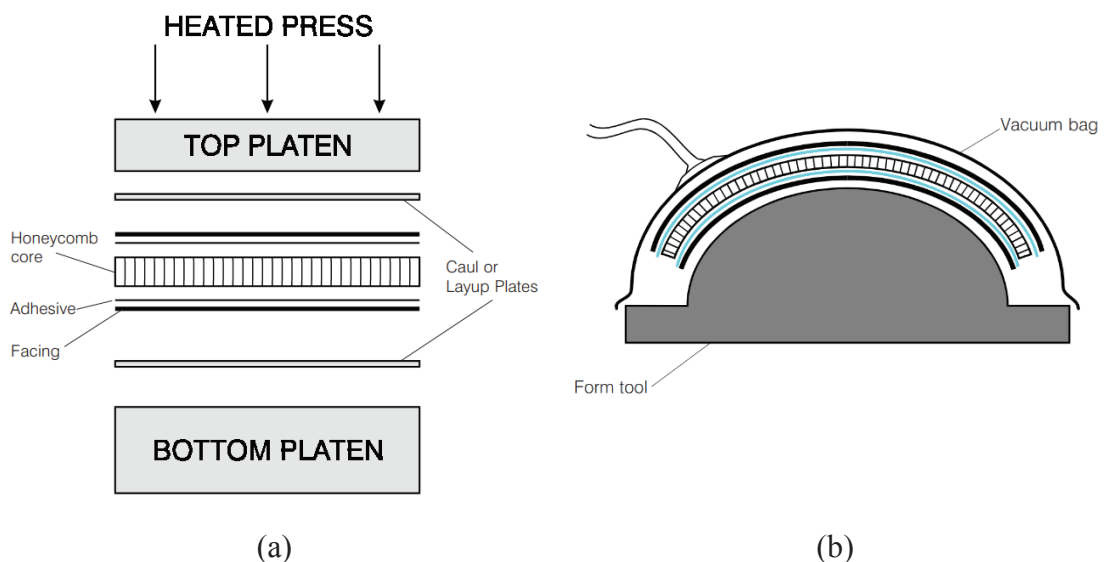
Figure 1.9. (a) heated Press[10] and (b) vacuum Bag Processing[10]

In 2012, the Boeing Company patented a manufacturing method of sandwich structures. In the process, the core covers a pre-stabilizing composite material, and that is called a pre-stabilized core (Figure 1.10a). Then, the pre-stabilized core surround by composite face sheets and the face sheets are cured. Pre-stabilizing of the core is made of two steps. In the first step, after the core is processed to a designed shape and size, the core covers with a pre-stabilizing composite material that may consist of glass or carbon fibers in a resin matrix. In the second step, the core with a pre-stabilizing composite cures in an oven cure cycle under pressure. For pressure, a vacuum bag or an autoclave may be utilized. So that without much change in weight, the strength of pre-stabilizing core section improvement. And during the curing of composite face sheets, the pre-stabilizing core provides higher pressure without the core collapse, which also causes low porosity in face sheets. Pre-stabilizing core prevents to entering of the resin into open-cells.

a) pre-stabilized core

b) Sandwich structure
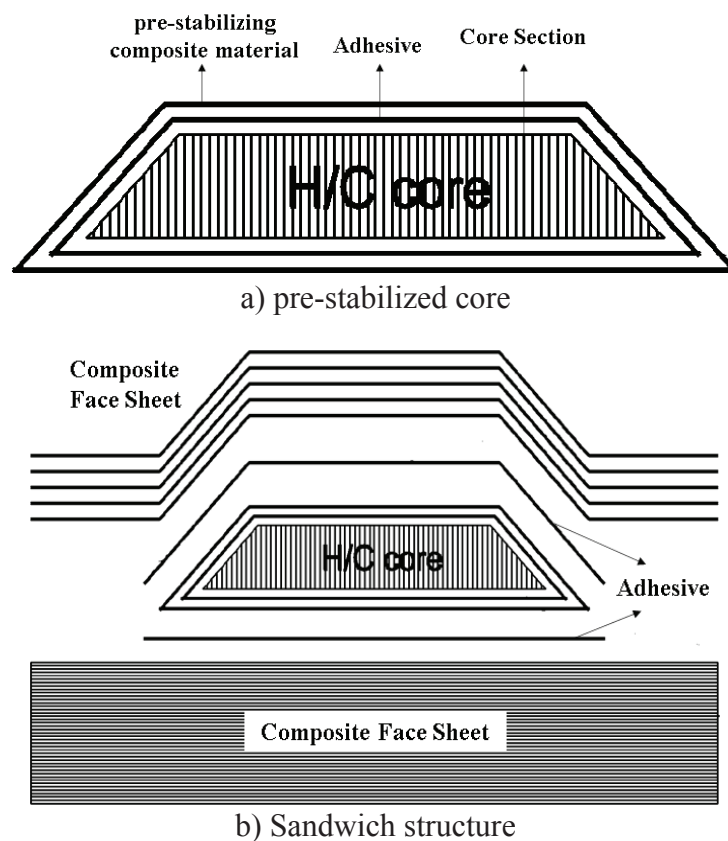
Figure 1.10. (a) corrugation[27] and (b) expansion manufacturing process[27]

1.3. The Impact Damage Resistance and Damage Tolerance of Sandwiches and Testing Methods

FRPCs exhibit a higher stiffness and strength in the in-plane directions since the fibers are aligned in this plane (fiber-dominated). In contrast, fibers cannot contribute to the stiffness and strength of the out-of-plane direction (matrix-dominated). Therefore, in the case of out-of-plane loading, the initial damage of composite face sheet is dominated by matrix cracking and delamination, and the combination of these two failure modes may also result in fiber breakage. FRPCs are, therefore, naturally damage sensitive to the out-of-plane loadings. In sandwiches, additional damages occur, including core crushing and cracking and the debonding of core from face sheet (Figure 1.11). When exposed to out-of-plane loads, sandwich structures lose their structural stiffness, stability and load-carrying capacities and form a dent at the impacted site, as seen in Figure 1.11.
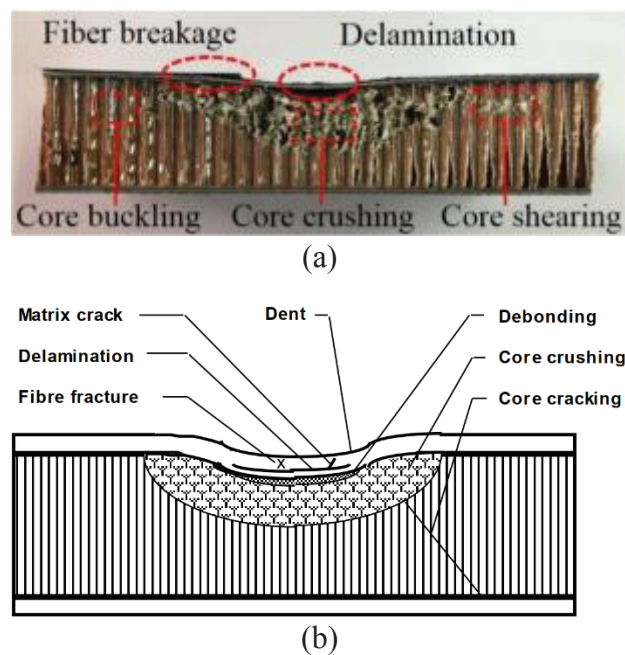
Figure 1.11. The failure modes of FRPC sandwiches in the out-of-plane impact (a) [28] (b) [29]

The sandwich structures used in the aerospace industry may be exposed to the impact loadings during manufacturing and in service through the out-of-plane direction.

These loadings may occur due to dropping tools and hailstone, bird and foreign object impact. Therefore, the impact damage resistance and damage tolerance of sandwiches are important and should be assessed prior to their use as structural elements. Impact damage resistance is defined as the ability of a sandwich structure to resist the damage initiation and/or growth upon applied impact loads, while damage tolerance is defined as the residual load-carrying capability of the impacted sandwich [23, 28, 30-36].

A widely used standard to measure LVI impact damage is the ASTM D7136/ D7136M–20: *Standard Test Method for Measuring the Damage Resistance of a Fiber-Reinforced Polymer Matrix Composite to a Drop-Weight Impact Event*. The quasi-static damage is assessed by the ASTM D6264/D6264M-17: *Standard Test Method for Measuring the Damage Resistance of a Fiber-Reinforced Polymer-Matrix Composite to a Concentrated Quasi-Static Indentation Force*[37]. The LVI damage in sandwiches is determined by the ASTM D7766/D7766M-16: *Standard Practice for Damage Resistance Testing of Sandwich Constructions*[38]. Two standards are widely used to measure the damage tolerances by the Compressive After Impact (CAI) residual strength after face-on impact: 1) (ASTM D7137/D7137M-17: *Standard Test Method for Compressive Residual Strength Properties of Damaged Polymer Matrix Composite Plates*[39]) (Figure 1.12a) 1) and 2) Airbus Method, AiTM 1-0010 (Figure 1.12b). For the edge impacts, the compression fixture of the ASTM D6641/D6641M-16e2: *Standard Test Method for Compressive Properties of Polymer Matrix Composite Materials Using a Combined Loading Compression (CLC) Test Fixture*[40] (Figure 1.12c) is used.

| (a) | (b) | (c) |
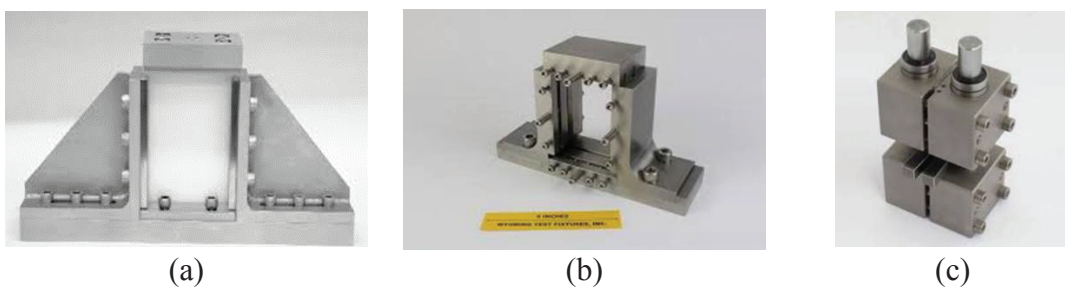
Figure 1.12. The test fixtures of the CAI residual strength after face-on impact (a) ASTM D7137 / D7137M - 17, (b) AiTM 1-0010, and (c) ASTM D6641 / D6641M - 16e2

The impact damages in composites are classified as Barely Visible Impact Damage (BVID), Visible Impact Damage (VID), Obviously Visible Impact Damage (OVID) and Discrete Source Damage (DSD) (Figure 1.13). BVID is the minimum permanent indentation damage that a component must be able to withstand without affecting the structural integrity (the component should sustain ultimate load), and the minimum permanent indentation is usually between 0.25 and 0.5 mm and detected in the visual inspection [41]. BVID may not be visible on a pre-flight inspection or even at scheduled maintenance. If the damage is detected by the service inspection, then the load requirement drops to Limit Load in case of VID or to a near-Limit Load in case of OVID (Figure 1.13). Structure with such damage is only expected to sustain the service environment for a period of time related to the inspection interval. DSD yields larger damages that are detectable without directed inspection and meets the continued safe flight load design values.
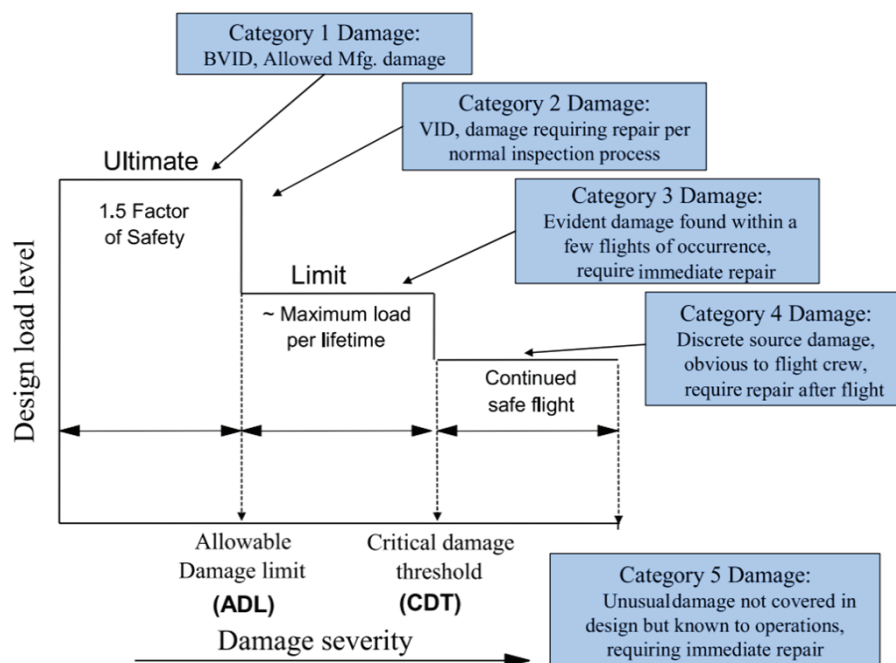
Figure 1.13. The classifications of impact damages on composites[42]

The impact responses of composites are affected by the primary and secondary factors, as shown in Figure 1.14. Resin toughness and fiber architecture are the primary factors affecting the impact resistance and damage tolerance of composites.

13

The secondary factors include environmental conditions, fracture toughness, repeated impacts, impactor geometry, matrix hybridization and stacking sequence. In a sandwich structure, the geometrical parameters such as the thicknesses of face sheets and core, support span and core type are also effective on the impact response. In addition, the material properties, including the elastic modulus of the face sheet, fiber orientation and shear modulus of the core, should also be taken into account in assessing the impact resistance.
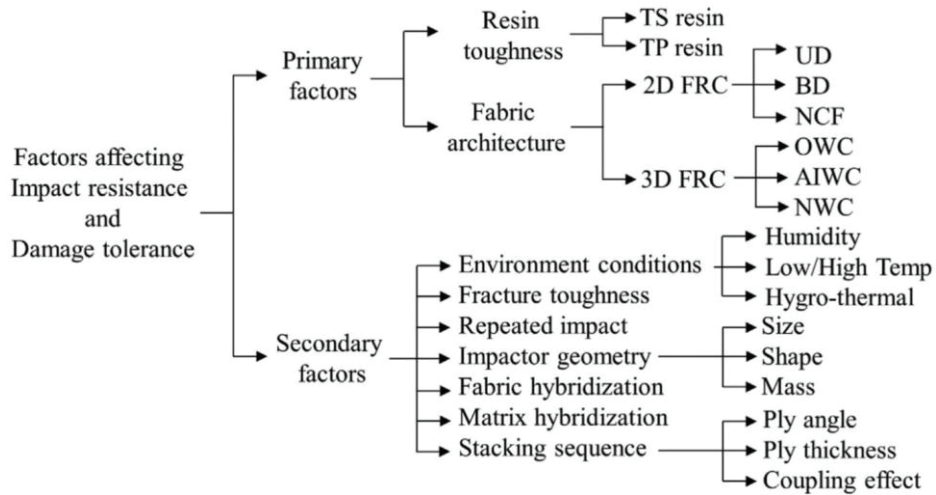
Figure 1.14. Factors affecting the impact resistance and damage tolerance of FRPCs[41]

1.4. The Impact Damage Resistance and Damage Tolerances of The Laminated Composite

The impact damage of laminated composites is mainly controlled by the failure strain of the matrix since the transverse matrix cracking is related to the ductility of the matrix and the mode II interlaminar fracture toughness[43]. As the ductility of a thermoplastic matrix is higher than that of a thermoset matrix, thermoplastic matrix composites are naturally more damage resistance. The mode II interlaminar fracture toughness determines the resistance of laminated composite against delamination type damage initiation and propagation. The interlaminar fracture toughness of thermoplastic composites has also shown to be several times higher than that of thermoset composites.[41]

Gao and Kim (2001)[43] investigated the impact resistance and tolerance of carbon fiber PEEK and epoxy laminated composites. Carbon fiber/PEEK laminated composite

exhibited a high impact resistance and tolerance than the carbon fiber/epoxy composite. A more ductility of the PEEK matrix of the carbon fiber/PEEK composite allowed a more extensive plastic deformation and higher energy absorption. The higher ductility and Mode II interlaminar fracture toughness of the carbon fiber/PEEK composite also caused a higher CAI strength (Figure 1.15a). The strength of carbon/thermoplastic composite is reduced by ~50%. In comparison, the strength of the carbon/epoxy composite by ~70% in the CAI tests at increasing impact energies (Figure 1.15a) and the CAI strain of the carbon/PEEK laminates was found almost twice that of the carbon/epoxy (Figure 1.15b).[44]

(a)   (b)
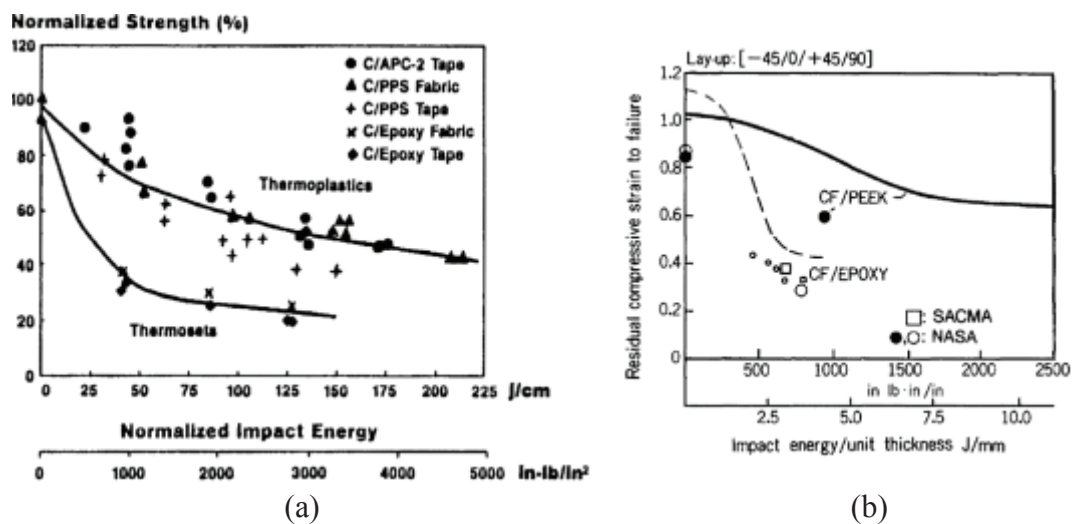
Figure 1.15. Comparison of the (a) CAI strength and (b) strain to failure of thermoplastic and thermoset composites[44]

Since the out-of-plane strength of laminated composites is weaker, the current strategies to improve the impact damage resistance and damage tolerance of laminated composites are mainly based on improving the interlaminar fracture strength. Unidirectional composites are generally poor under transverse loadings and undergo large delamination, fiber failure and matrix damage. 2D woven/bidirectional composites show better impact resistance due to the undulation of yarns; however, their in-plane properties are reduced due to the stress concentrations resulted from the crimping of yarns. Non-Crimp Fabric (NCF) has been developed to improve the impact and delamination resistance of woven fabrics. In NCF, two (bi-axial) or more (multi-axial) layers of fabrics

are stitched through thickness to produce "blankets". Non-crimping increases the in-plane mechanical stiffness and also the impact resistance of the composite. The resistance of laminated composites against delamination can also be increased by stitching, z-pinning and weaving. Stitching and z-pinning prevent the growth of delamination by reducing the crack formation range and crack propagation, acting as bridges to crack; hence, improve the impact resistance of the composite. In general, 3D woven composites have higher damage resistance and tolerance than 2D woven composites, while 2D woven composites have higher damage resistance and tolerance than UD composites.

The effect of stitching on the LVI behavior of carbon fiber fabrics was investigated.[45] The presence of weak resin-rich pockets around stitches formed matrix crack initiation sites upon impact loading. The high stitch density and thick stitch reduced the extent of delamination in the composite by reducing the crack size and crack propagation. Higher stitch density and thickness were shown to be more effective in impeding delamination growth by effectively bridging delamination cracks and arresting crack propagation.

F. Chen and Hodgkinson (2009)[46] compared the impact resistance and tolerance of a 32-ply carbon fiber/epoxy (8552/AS4) laminated and NCF composites with the same (−45/90/0/+45/+45/0/90/−45/+45/90/0/−45/−45/0/90/+45) lay-up and a 3D woven carbon fiber/epoxy composite under LVI and HVI loadings. 3D woven composite showed the highest damage resistance and tolerance in the LVI tests, while NCF composites showed the highest damage resistance in the HVI tests. The reduced damage resistance of the 3D composite in the HVI tests was attributed to the lower in-plane strength of 3D composite and the lower contributions of fibers through thickness direction.

Seltzer et al. (2013)[47] studied LVI tested S2-glass, carbon or a hybrid fiber 2D and 3D epoxy and vinyl ester matrix composites. The energy absorption of 3D composites in the LVI tests was shown twice that of 2D composites, regardless of the type of reinforcement used. The reinforcements in the z-direction in the 3D composite enabled the composite to absorb more energy by maintaining the integrity of the composite and resulted in a deeper indentation by the impactor. This resulted in intensive energy dissipation by tow splitting, fiber breakage, and formation of a plug by out-of-plane shear. The maximum impact load was shown to be related to the tensile fiber fracture at the backside surface, and S2 fibers showed a better performance in that. Bandaru et al. (2017)[48] reported a similar enhanced impact resistance of basalt fabrics when interlacing

the brittle basalt yarns with Kevlar yarns.

Sanchez-Saez et al. (2005)[49] investigated the effect of fiber lay-up on the damage tolerance of the laminated composites with cross-ply, quasi-isotropic and woven configuration. The woven lay-up had the highest CAI strength, and the quasi-isotropic play-up had the lowest. The cross-ply configuration showed an intermediate CAI strength. However, as the impact energy increased, quasi-isotropic play-up showed a less decreasing reduction in the CAI strength. K.K. Singh, N.K. Singh, and Jha (2016)[50] investigated the LVI behavior of symmetric and asymmetric glass fiber reinforced laminated composites. The symmetric laminate absorbed more energy than the asymmetric laminate.

Choi, Wang, and Chang (1992)[51] investigated the effect of stacking sequence, ply orientation, laminate thickness and impactor mass on the impact response of a graphite/epoxy laminate. The impact resistance of the laminate was affected more by the ply orientation and stacking sequence than by the laminate thickness.

R. Olsson (2000)[52] studied the effect of impactor mass on the impact response of composite sheets at different velocity levels. The quasi-static response of composite was shown to be dominated by flexural loads, and the coupon dimensions and boundary conditions were essential parameters affecting the response (Figure 1.16a). On the other side, the LVI response was dominated both by flexural and shear waves (Figure 1.16b). And a three-dimensional wave propagation is seen in the ballistic impact response (Figure 1.16c). Quasi-static forces such as the dropping of heavy tools and the LVI events such as hailstone and runway debris cause BVID, while the ballistic impact events generally cause VID.
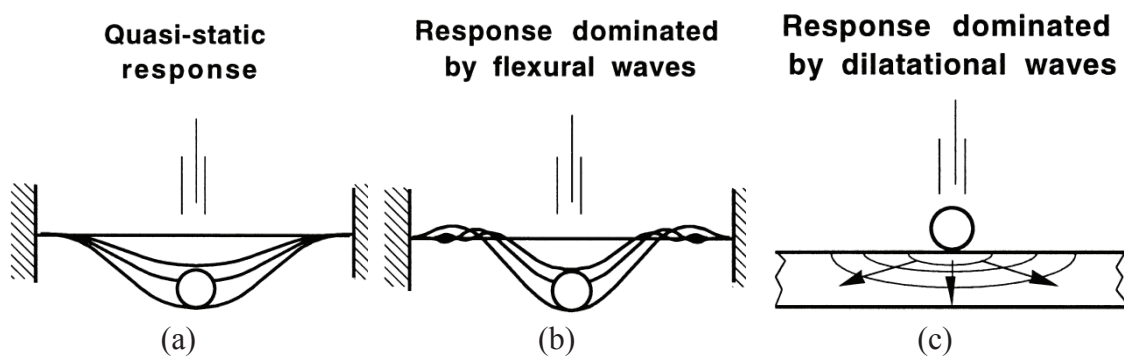
Figure 1.16. (a) quasi-static indentation force (b) low-velocity impact event, and (c) ballistic impact event[52]

The impactor mas and velocity also affect the initiation of damages. A light weight impactor at 45 ms^{-1} was shown to result in an increase peak load and initiate earlier damage than a heavy impactor at 3.65 ms^{-1} in a carbon/epoxy composite plate (Figures 1.17a and 1.17b)[52]. The high-velocity impact was reported to cause a wider delamination area in the composite. Cantwell and Morton (1989)[53] investigated the impact loading response of a carbon fiber reinforced laminate at low and high velocities. In the HVI test, the impact energy was localized at the impact point, while the composite responded overall mode in the LVI test (Figure 1.18a). Thus, structure geometry played an intensive role in the LVI-induced damages. The HVI-induced damage resulted in a larger drop in the after impact strength than the LVI-induced damage (Figure 1.18b).
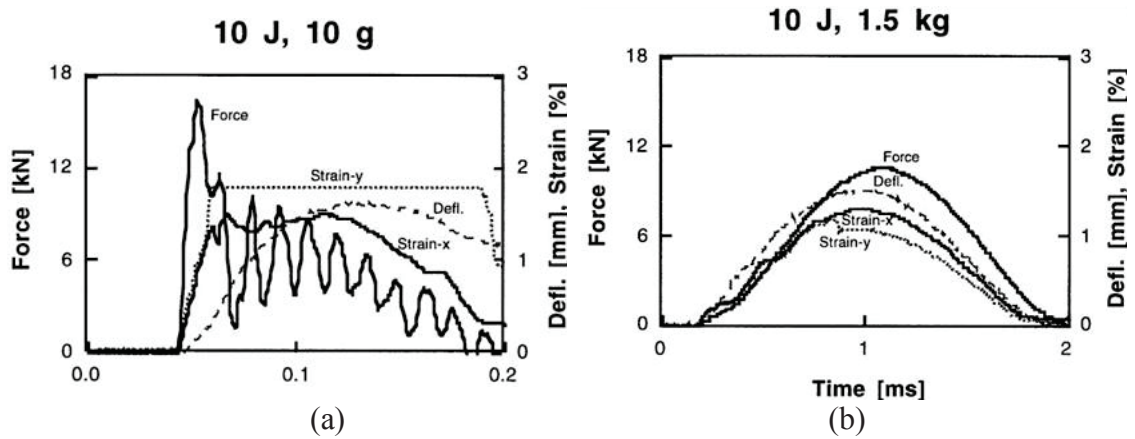
Figure 1.17. The effect of velocity on the damage resistance of a carbon/epoxy composite plate at (a) 45 ms^{-1} and (b) 3.65 ms^{-1} [52]
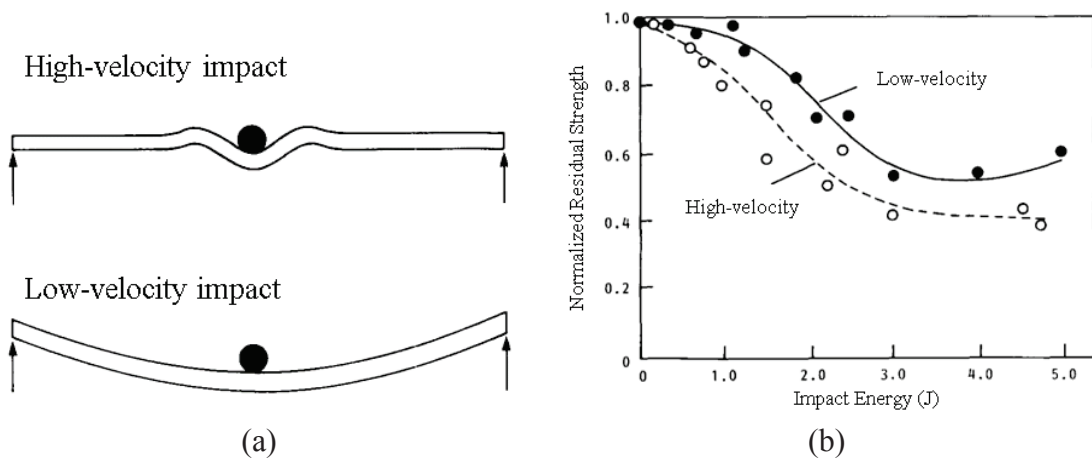
Figure 1.18. HVI and LVI (a) deformations and (b) residual strengths [53]

1.5. The Impact Damage Resistance and Damage Tolerance of Sandwich Structures

Kim and Jun (1992)[54] conducted a study on the delamination area of the laminated composite face sheet sandwich structures subjected to impact. The sandwich structure consisted of carbon/epoxy pre-preg face sheets and a Nomex honeycomb core. Two quasi-isotropic lay-up of a small relative angular orientation (0/45/90/-45)$_s$ and a large relative angular orientation (45/-45/0/90)$_s$ were investigated with low- and high-density cores (48 and 128 kgm^{-3}), respectively. Results showed that the laminates with the small relative angular orientation between adjacent plies tended to be more damage resistant than those of the large relative angular orientation. For the lay-up of small relative angular orientation, the face-sheet showed a smaller delamination area than a laminate of the same lay-up sequence, resulting from the presence of a core. While, for the lay-up of large relative angular orientation, the face sheet of the sandwich plate had a larger delamination area than a laminate of a layup sequence below a particular value of absorbed energy. The sandwich face sheet with a low-density core had a higher delamination area than that with a high-density core under the same impact energy.

Minguet (1991)[55] developed an analytic model for the essential parameters of the core crushing strength, core stiffness and face bending stiffness of sandwiches. Bernard and Lagace (1989)[56] studied the impact response of a (±45/0)$_s$ graphite/epoxy sandwich structure cored with Rohacell foam, Nomex honeycomb and aluminum honeycomb. The largest delamination on the face sheet was at (±45) between the core-face sheet interface for all cores. The sandwich with Nomex honeycomb core had a smaller delamination area than the sandwich with Rohacell foam under the same impact energies. The damage area depended mainly on the impactor diameter up to a specific energy limit. But, when the energy limit exceeded, the energy levels played an intensive role in the damage area. The sandwich with a thicker core had larger damages than those of the sandwich with a thinner core for the same energy level. The number of damaged cells of the Nomex honeycomb sandwich was smaller than that of aluminum honeycomb sandwich.

Aminanda et al. (2009)[57] reported that the load was mainly carried by the vertical edges of the honeycomb core when the sandwich was subjected to compressive load in the out-of-plane direction. Xue et al. (2019)[28] found that the height of Nomex honeycomb

did not affect the maximum impact force of the sandwich; the peak force was shown to be merely dependent on the core wall thickness and core cell size. In contrast, He et al. (2019)[31] showed that the thickness of the face sheet was the most effective geometrical parameter increasing both the structural stiffness and energy absorption of the CFRP-aluminum honeycomb sandwich structures. The cell wall thickness and size were less effective than the thickness of the face sheet regarding the energy absorption. H. Wang, Ramakrishnan, and Shankar (2016)[58] investigated the effect of five different core materials on the impact response of sandwich structures with Al2024-T3 face sheets. The core materials were chosen from low-density Balsa wood, high-density Balsa wood, cork, Polypropylene (PP) honeycomb, and Polystyrene (PS) foam. It was shown that cores played a vital role in the impact resistance of sandwich structures. Compared to the PP honeycomb core, the PP foam core was shown to be a better choice in energy absorption (Figure 1.19a). At the same time, PP honeycomb was more resistance to full-penetration as decreasing the back face sheet deformation (Figure 1.19b). Xie, Jing, et al. (2020)[59] showed that the impact resistance of Nomex honeycomb sandwich structures with aluminum face sheets depended on the core thickness, face sheet thickness, impactor diameter and energy levels. As the core density decreased to a limit, the impact resistance of the sandwich structure decreased, and the impact resistance of honeycomb sandwich structures increased as the face sheet thickness increased. The impactor diameter also played a role in damage behavior. While the sharp impactor caused local damage and penetration at low energy levels, it caused global damage at high energy levels.

(a)   (b)
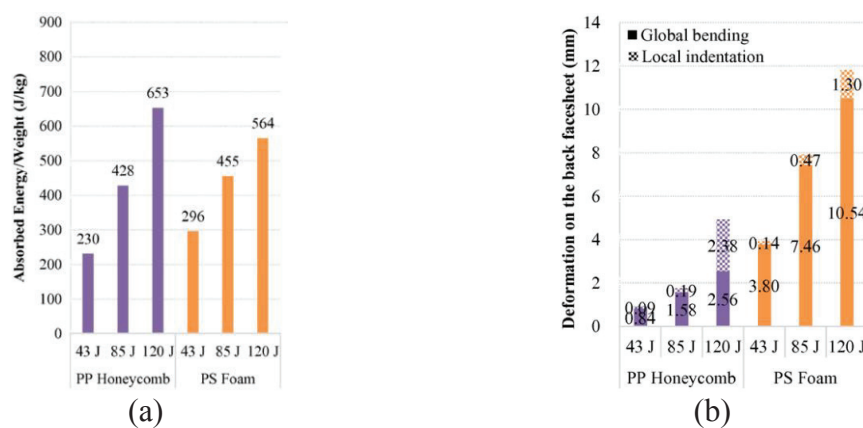
Figure 1.19. (a) Specific energy absorption and (b) back face sheets deformation of Al2024-T3 sandwiches with different cores under variety energy levels [58]

1.6. Motivation

The majority of the studies on the impact resistance and tolerance of sandwiches within the last 10-year focused on the impact energy levels less 10 J, as shown in Figure 1.20a). In the same studies, the impact velocities ranged from 0-3 ms^{-1}, except for one study which was performed at 20 ms^{-1} (Figure 1.20b). About 53% of the studies were on the CFPC, 20% on the aluminum and 10% on the GFRP face-sheet sandwiches (Figure 1.21a). The core was Nomex honeycomb in ~40%, aluminum honeycomb in ~27% and foam in 24% of the studies (Figure 1.21b). The thickness of face sheets ranged 0.45-3.2 mm with a focus in the 0-1 mm range. The core height ranged from 3.81-40 mm. It has also been noted that there were few studies on the effect of impact velocity on the impact response of laminated composites, and there has been no study on the sandwich structures. The primary aim of this thesis is, therefore, to determine the effect of impact velocity on the impact resistance and damage tolerance of a Nomex honeycomb/Glass FRPC sandwich. The thesis also seeks to develop an HVI test method for such sandwiches by keeping the same impact energies with the LVI tests. The experiments performed may be divided into two parts: 1) quasi-static indentation force and low and high-velocity impact response and 2) the compression after impact tests.

(a)
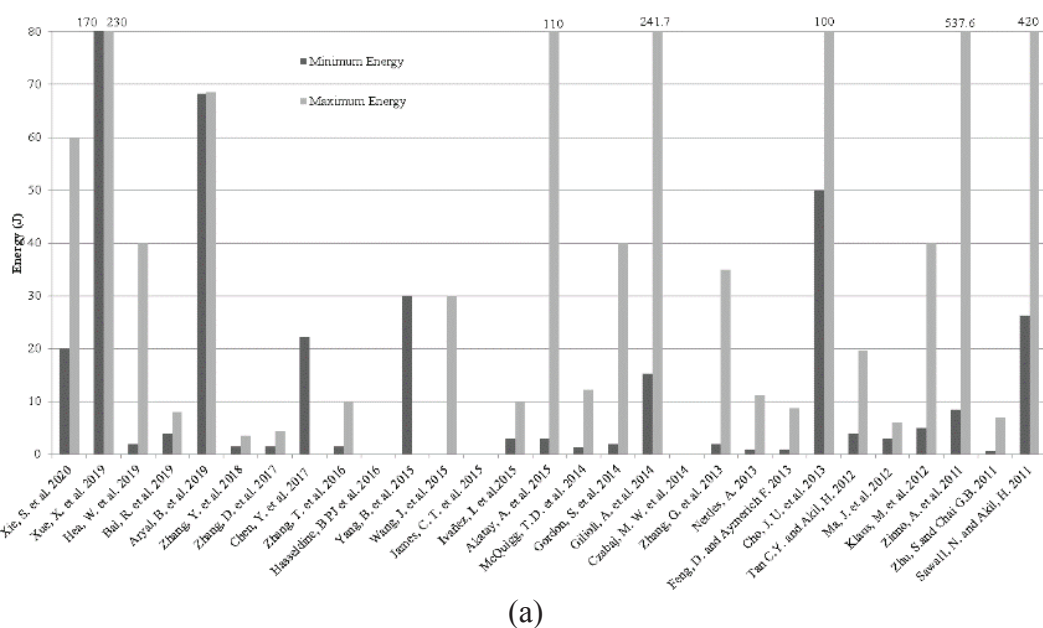
Figure 1.20. (a) The impact velocity levels and (b) energy levels of the studies performed on sandwiches within the last 10-year [2, 23, 28, 31-33, 35, 59-80]

(cont. on next page)
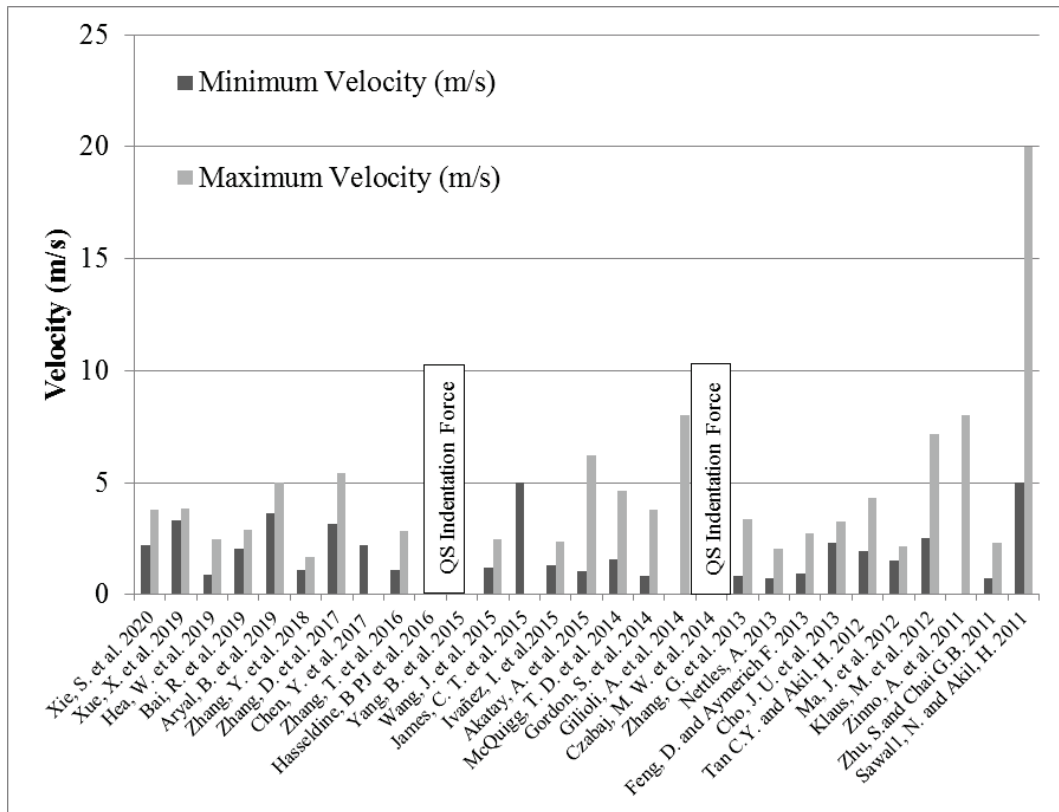
(b)

Figure 1.20 (cont.)
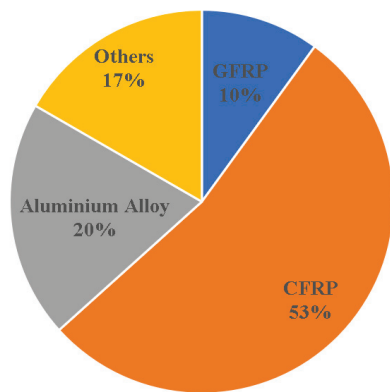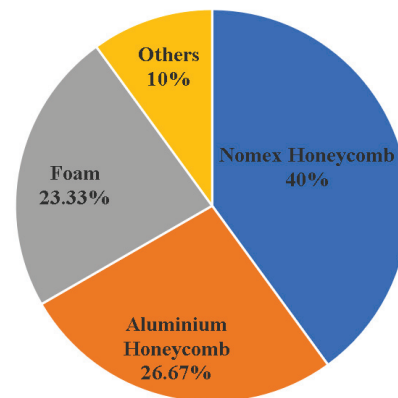
(a)   (b)

Figure 1.21. (a) Face sheet materials, and (b) core materials of the studies performed on sandwiches in the last 10-year

CHAPTER 2

EXPERIMENTAL STUDY

2.1. Materials

The E-glass fiber (7781GL) reinforced epoxy face-sheets and the Nomex honeycomb core sandwich test coupons were provided by ASELSAN. The sandwich construction schematic and the geometrical parameters of the core, and the pictures of a test coupon from the front and back face are shown in Figures 2.1a and 2.1b, respectively. The face sheets were bonded to the core by using an adhesive, as shown in Figure 2.1a. The composite face sheets were made of 8 harness satin weave fabric E-glass pre-impregnated with an epoxy resin type VICOTEX 913. The product designation of the fiber yarn was ECDE 75-1/0, and the fiber areal density was 0.299 kgm^{-2}. The fiber volume fraction of the composite face sheet was 63%, with a cured ply thickness of ~0.22 mm. The curing was performed at 125° C. Breaking strengths of warp and filling directions of the fabric are 99.8 Nmm^{-1} and 78.80 Nmm^{-1}, respectively. The face sheet laminate had a layup of $(0/45/90/-45)_s$ with a sheet thickness (t_f) of 0.88 mm. The mechanical properties of the composite face sheet are tabulated in Table 2.1. The x- (11) and y-direction (22) in the same table correspond to the warp and filling directions (in-plane directions), respectively and 3 to the thickness direction.

The honeycomb (hexagonal cell) core is made of phenolic resin-impregnated aramid paper Nomex. Due to processing technology, two out of hexagonal cell walls have a wall thickness that is twice as much as that of the others, as shown in Figure 2.1a. The geometrical parameters are the length (L), width (W) (ribbon direction), face sheet thickness (t_f), core depth (h_c) core cell wall thickness (t_c) and diameter (d) of a semicircle inscribed in the cell in Figure 2.1a. These parameters for the Nomex core of the investigated sandwich are as follows: L=150 mm, t_f=0.88 mm, h_c=6 mm, t_c=0.1 mm, d=5 mm, and the adhesive layer thickness is 0.001 mm. The mechanical properties of the used Nomex core are further tabulated in Table 3.2. The density of the core is 48 kg m^{-3} with an out-of-plane compressive strength of 1.4-2.2 MPa. The shear strength and modulus in

the L-direction are noted to be higher than that of the W/ribbon direction due to higher cell thickness, as tabulated in the same table. Standard size test coupons 150 mm in length and 100 mm in width based on the ASTM D7766/D7766M–16 were used in both the indentation, LVI, HVI and CAI tests. A total of 60 coupons in 5 batches was received, and 50 coupons were tested. The thickness of each sandwich coupon was measured using a caliper and determined 7.8 mm on average. The thickness of the adhesive was 0.01 mm. In the indentation and low-velocity impact tests, the face sheet that the impactor tip firstly impinges is labelled as the front face sheet (Figure 2.1b). The width of the coupon is the ribbon direction, and the length is the L-direction of the core, as seen in Figure 2.1b.

(a)
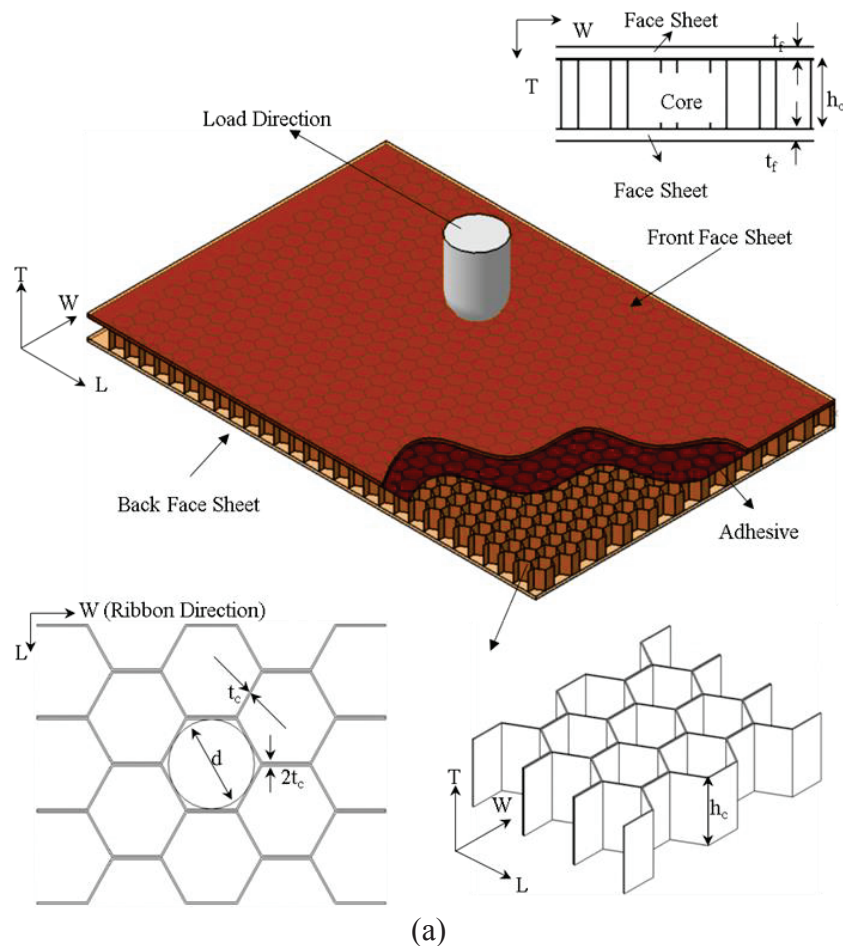
Figure 2.1. (a) The schematic of sandwich construction and geometrical parameters of the core and (b) the pictures of a test coupon from front and back face
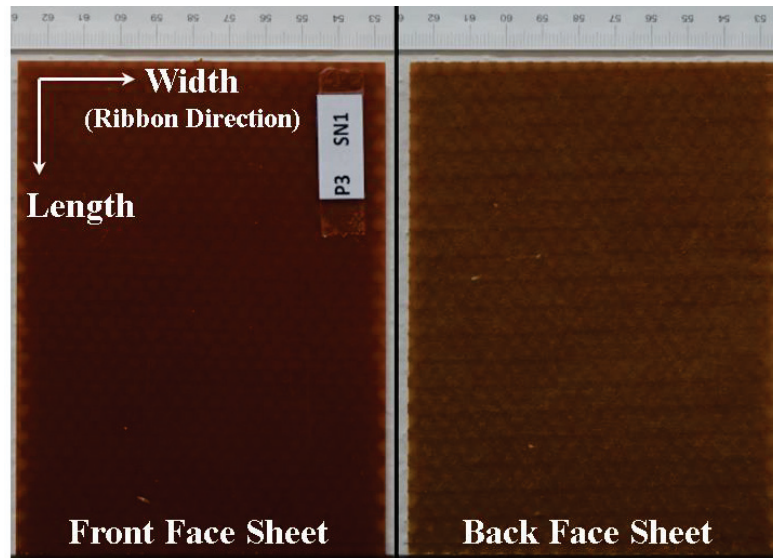
(b)

Figure 2.1. (cont.)

Table 2.1. The mechanical properties of E-glass fiber (7781GL) reinforced epoxy
composite face-sheet

Symbol	Property	Value
X_t	Tensile strength	479.0 MPa
Y_t	Tensile strength	410.7 MPa
X_c	Compressive strength	512.0 MPa
Y_c	Compressive strength	422.5 MPa
E_{11}	Stiffness	22.3 MPa
E_{22}	Stiffness	20.7 MPa
S_{12}	Shear strength	95 MPa
S_{13}, S_{23}	Shear strength	63 MPa
G_{12}, G_{13}, G_{23}	Shear modulus	5.1 GPa
ρ	Density	2.09×10^{-9}-ton mm^{-3}
v_{12}	Poisson's ratio	0.13

Table 2.2. The mechanical properties of Nomex (datasheet values)

Properties	Test Method	Typical/Min Values
Cell Size (mm)	-	5.0
Density (kg/m^3)	MIL-STD-401	48
Compression strength unstabilized/bare (MPa)	MIL-STD-401 DIN 53291	2.2/1.4
Compression strength stabilized (MPa)	MIL-STD-401 DIN 53291	N/A
Plate shear strength/L-direction (MPa)	MIL-STD-401 DIN 53294	1.05/0.75
Plate shear modulus/L-direction (MPa)	MIL-STD-401 DIN 53294	45/30
Plate shear strength/W-direction (MPa)	MIL-STD-401 DIN 53294	0.53/0.40
Plate shear modulus/W-direction (MPa)	MIL-STD-401 DIN 53294	23.5/17.5

2.3. Concentrated Quasi-Static Indentation Tests

Quasi-static indentation tests were performed in a Shimadzu Universal Testing machine. The test is schematically shown in Figure 2.2a. A 16 mm-hemispherical tip indenter, the same as the LVI tests, was used to indent the coupon at a crosshead speed of 1.25 mm min^{-1} in accord with ASTM D6264/D6264M-17. The same support fixture of the ASTM D7136/D7136M-20 was also used in the quasi-static indentation tests to maintain the same boundary conditions with the low-velocity impact tests (Figure 2.2b). Two cameras were used to record the indentation damage at the front and back face sheet (Figure 2.2b). In a typical test, the sandwich coupon is placed on a steel support fixture and centered relative to the cut-out by the guide of the pins on the support fixture. The coupon is then fixed on the support fixture using four rubber-tipped clamps, as shown in Figure 2.2. The clamp tips are positioned approximately at a distance of 25 mm from the coupon edges.

(a)
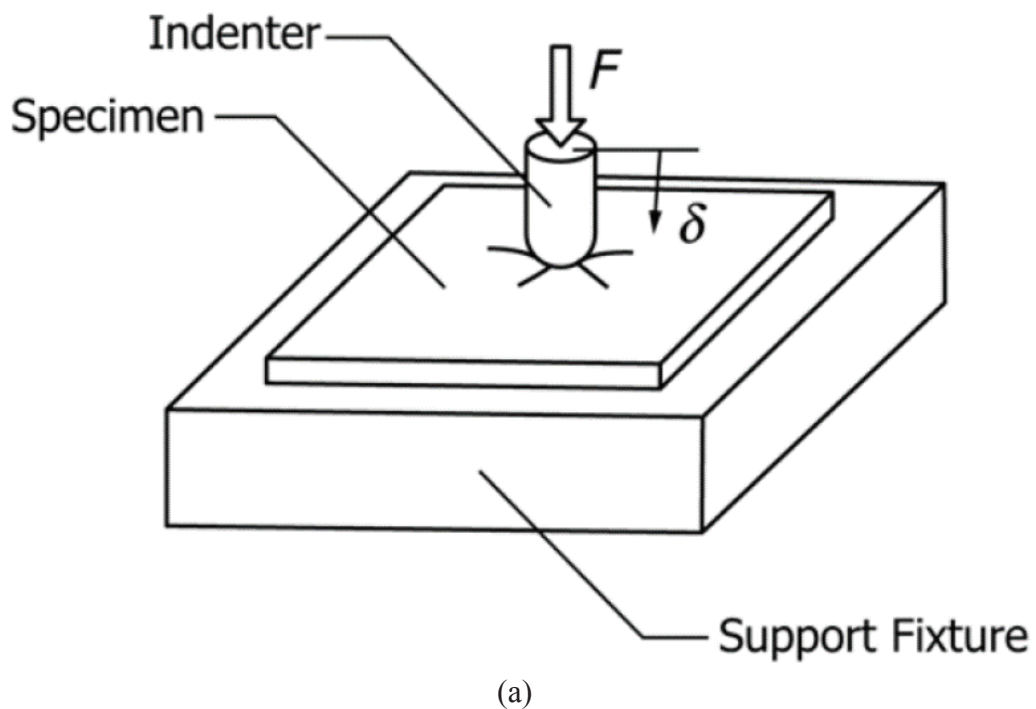
Figure 2.2. (a) Quasi-static indentation test[37] and (b) the test set-up
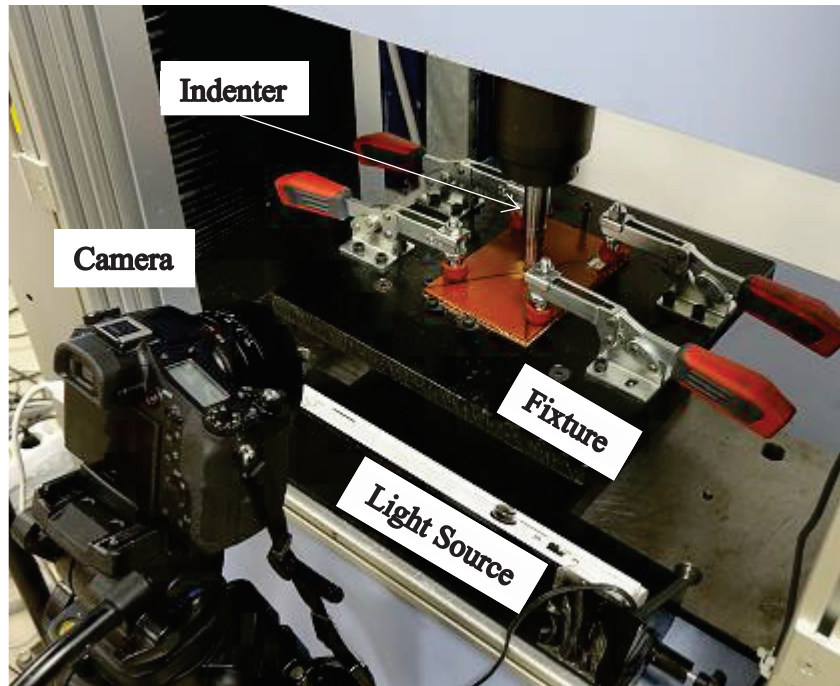
(b)

Figure 2.2. (cont.)

2.4. Low-velocity Impact Tests

The LVI tests were performed on the standard test coupons (Figure 2.3a) using an impact support fixture (Figure 2.3b).[81] The Drop Weight (DW) CEAST Fractovis Plus, later trade named Instron, is shown in Figures 2.4a and 2.4b. DW tester is equipped with carriage mass, an anti-rebound system that prevents more than one impact, guide rail, and the impactor tup with stain gauge (Figure 2.4b). A high-speed camera was used to observe the impact damage of the sandwich coupon. In a typical test, the sandwich coupon is placed into the DW tester steel support fixture. The coupon is centered relative to the cut-out by the guide of the pins on the support fixture. The coupon is fixed on the support fixture using the four rubber-tipped clamps and secured to prevent the indenter rebounding during the impact event. The clamp tips are positioned approximately 25 mm away from the coupon edges. The hemispherical tip with a diameter of 16 mm was used as an impactor, and the total mass of the impactor was 5.79 kg.
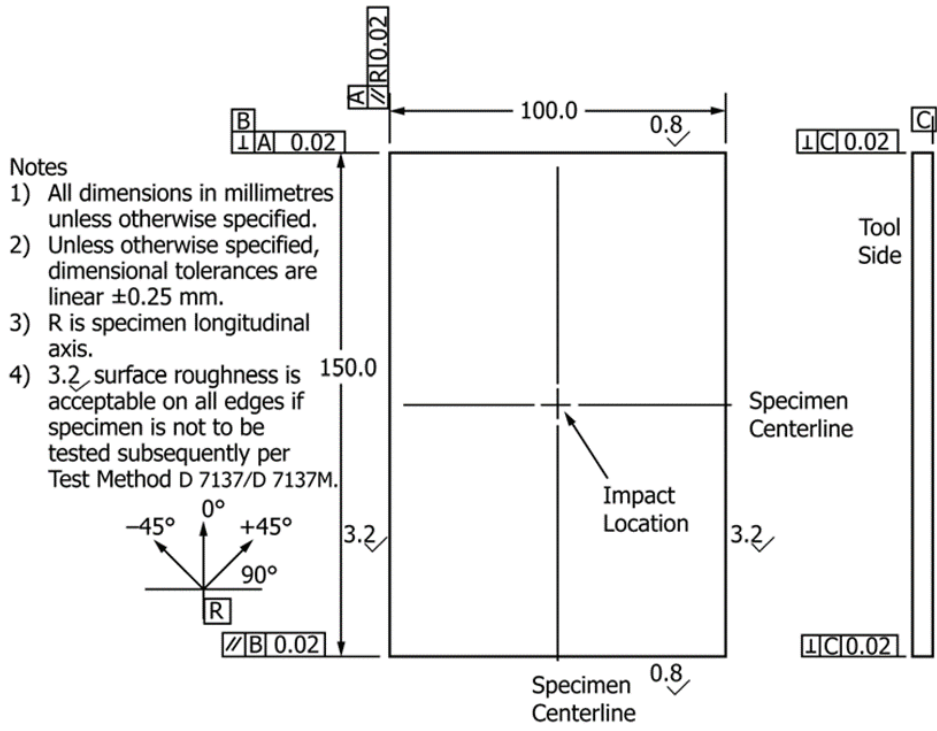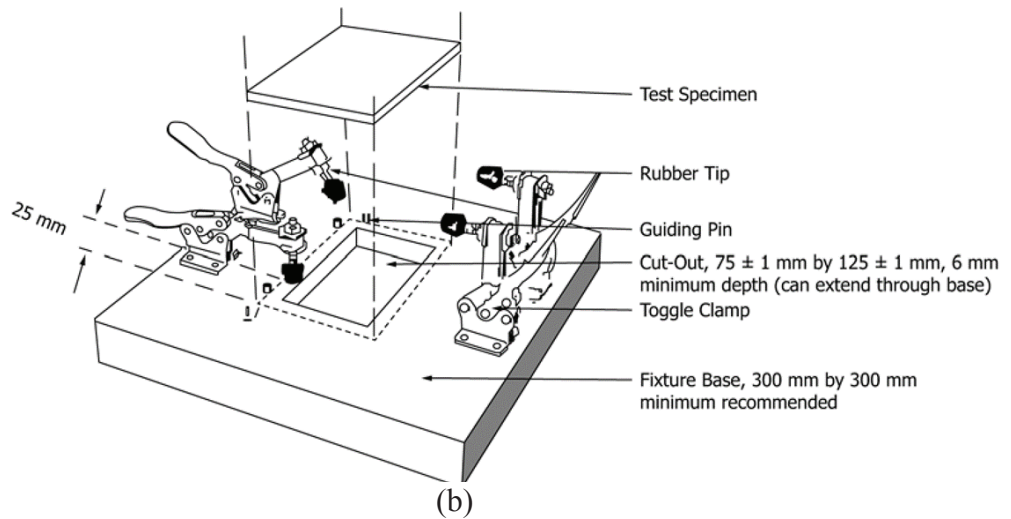
Figure 2.3. (a) DW impact test specimen[7] and (b) impact support fixture[7]
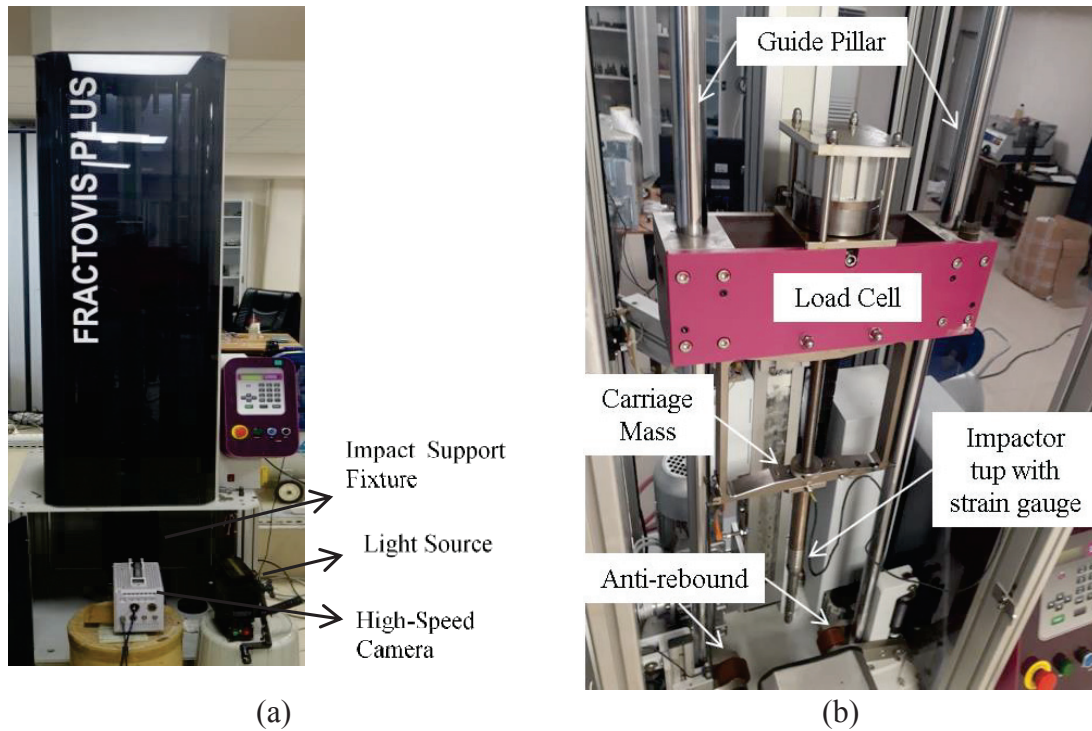
Figure 2.4. CEAST Fractovis Plus DW tester (a) general view and (b) inside

2.5. High-velocity Impact Tests

The HVI tests were performed using the gas-gun set-up of a Split Hopkinson Pressure Bar (SHPB). The HVI test set-up consisted of a gas gun, barrel, hemispherical tip and DW tester steel support fixture (Figures 2.5a and 2.5b). The high-speed camera was used for double purposes. First, it was used to measure the impact velocities, and therefore it was positioned perpendicular to the route of the impactor. Second, it was conveniently placed to observe the impact damage area on the sandwich coupon, as shown in Figure 2.5b. In a typical test, the test coupon is first fixed in the DW tester steel support fixture (Figure 2.5b). The indentation tip is inserted inside the barrel of the gas gun. Releasing the gas of the gas gun fires the tip against the test coupon. The velocity of the used indentation tips varied with the pressure of the sued gas gun. Therefore, preliminary tests were conducted to determine the impact velocities corresponding to the same impact energy level under the DW tester. Three different hemispherical tips with a diameter of 16 mm were used in the HVI test, as depicted in Figure 2.5c. The masses of the tips were 0.026, 0.043 and 0.059 kg. The HVI test indenter mass, impact energy and

impact velocity are tabulated in Table 2.3. As noted in the same table, the impact velocities ranged 15-30 ms⁻¹. A planar impact of the tip in the test was also checked with high-speed camera records.
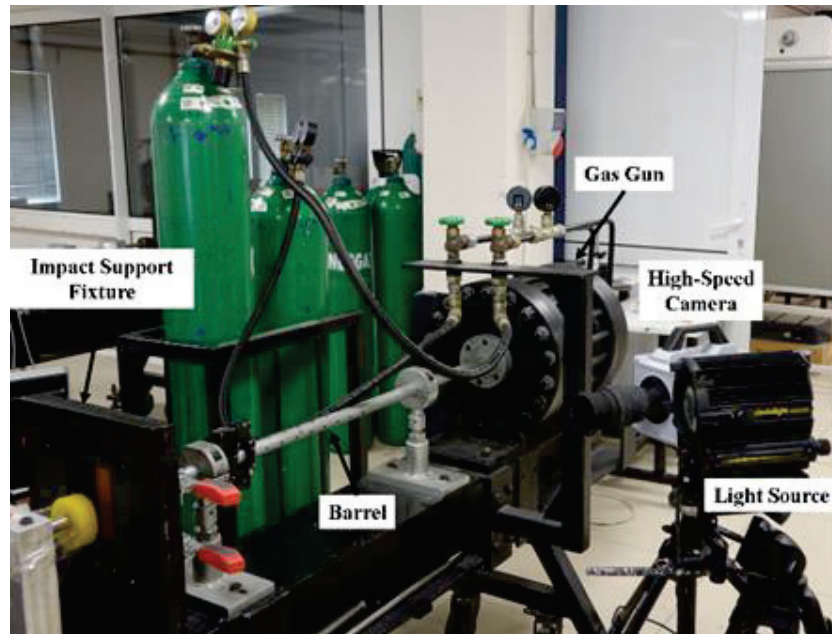
(a)
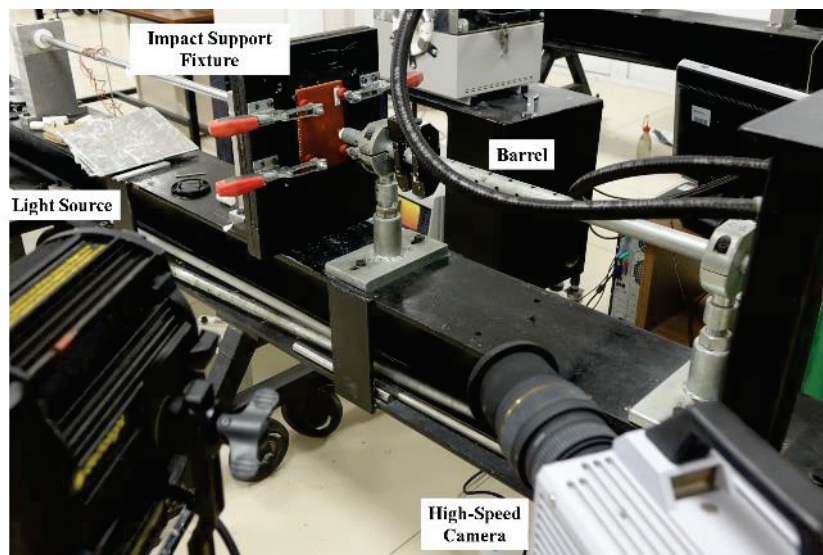
(b)

Figure 2.5. (a) and (b) the SHPB HVI test set-up, and (c) tips

(cont. on next page)
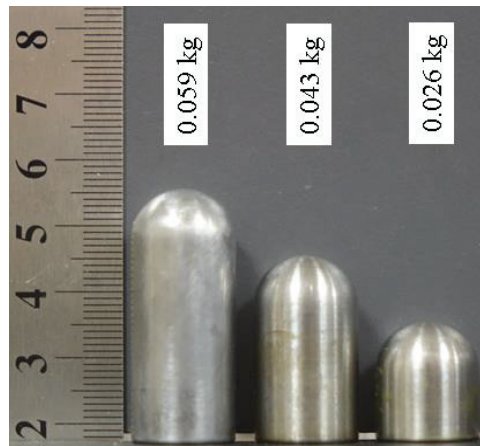
(c)

Figure 2.5. (cont.)

Table 2.3. HVI test indenter mass, impact energy and impact velocity

	Tip mass (kg)	Label	E_i (J)	v_i (ms^{-1})
High-velocity Impact	0.026	HVI 3 J	3	14.5
		HVI 5.5 J	5.5	2
		HVI 11 J	11	29
	0.043	HVI 33.5 J	33.5	27.5
	0.059	HVI 11 J	11	19
		HVI 22 J	22	28

2.6. Damage Determination

At least three coupons were tested at each energy level. The maximum residual indentation depth was immediately measured after the test using a dial indicator shown in Figure 2.6a. The visible planar damage area and diameter were determined based on the ASTM D7136 / D7136M-20. In accord with this standard, the lines with 45 degrees and 135 degrees were drawn along the center of damage area, and the longer length of the two lines was taken as the maximum diameter of the damage area (Figure 2.6b). The lines with 90 degrees and 0 degrees were taken as the length and width, respectively. The damage area, width, length and diameter of the tested coupons were measured using ImageJ software. An example of measurements is shown in Figure 2.6c. In the program, the damage area was enclosed by a solid line, and then the software calculates the area of the enclosed section after entering a calibration length.

(a)
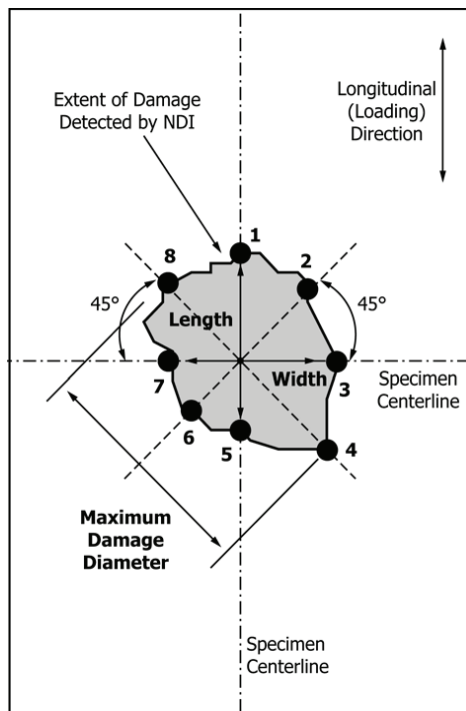
(b)
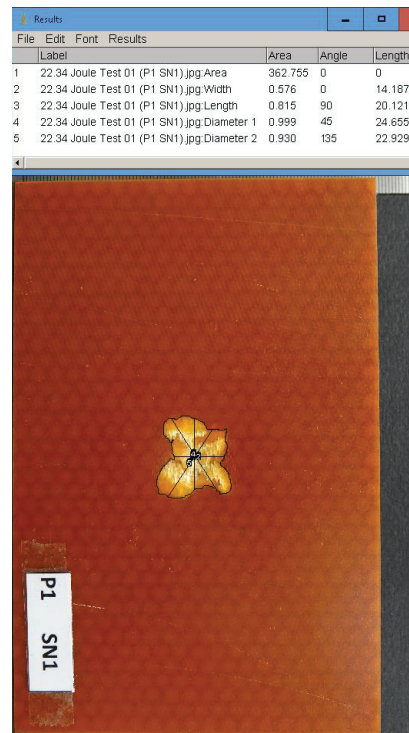
(c)

Figure 2.6. (a) the dial indicator, (b) damage area and diameter determination[7], and (c) a view from the used software to calculate damage area and diameter

2.7. Energy Absorption

The energy absorption (E_A) is

$$E_A = E_K + mg\delta \qquad (2.1)$$

where, E_K is the kinetic energy of the impactor, m is the impactor mass, g is the gravitational acceleration, and δ is the displacement. Figures 2.7a and 2.7b show the impact energy and energy absorption (E_A) versus time curves of sandwich coupons tested at 22.5 and 67 J, respectively. In the low impact energy test, the impactor rebounds (Figure 2.7a), while in the high impact energy test, the impactor fully penetrates the coupon (Figure 2.7b). As seen in the same graphs, the energy absorption is slightly higher than the kinetic energy of the impactor because the potential energy is added to total energy when the impactor impacts the coupon. The energy absorption of the coupons was experimentally calculated as the area under the load-displacement curve up to the displacement at which back face sheet fractures as

$$E_A = \int_0^{\delta_{max}} P_{(\delta)}d\delta \qquad (2.2)$$

where $P_{(\delta)}$ is the force and δ_{max} is the displacement when the back face sheet fractures. The sandwich coupon subjected to the concentrated quasi-static indentation force was fully penetrated, as seen in Figures 2.8a and 2.8b. The energy absorption was calculated in these tests until δ_{max}, as shown in Figure 2.8a. Half-penetration in the LVI tests occurs when the impactor causes fracture at the front face sheet and rebounds. The energy absorption in a half-penetration was calculated by integrating all area under the force-displacement curve, as shown in Figures 2.9a and 2.9b. The maximum integration value gives the absorbed energy value as indicated by an arrow in Figure 2.9b. In full penetration (penetration to both front and back face sheet), the energy absorption was calculated as the area up to the displacement corresponding to the back face sheet fracture (Figures 2.10a and 2.10b). The LVI test indenter mass, impact energy and impact velocity are tabulated in Table 3.4. A constant impactor mass was used in all tests. The impact

velocities as noted in the same table ranged 2.7-4.81 ms^{-1} and the energies 22-65 J. At least three tests were performed at each impact energy.
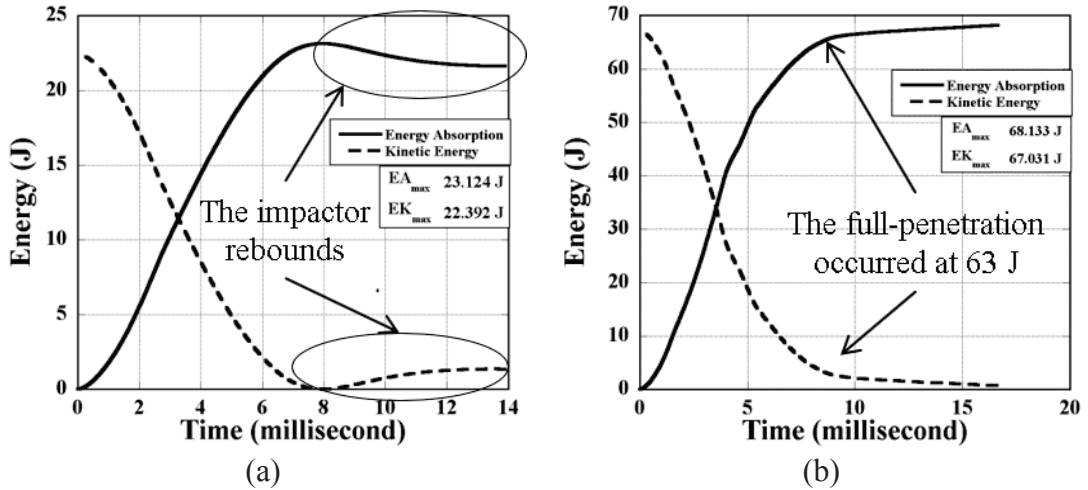
Figure 2.7. The kinetic energy (E_K) and energy absorption (E_A) versus time curves of the sandwich coupons exposed to the LVI at (a) 22 and (b) 67 J
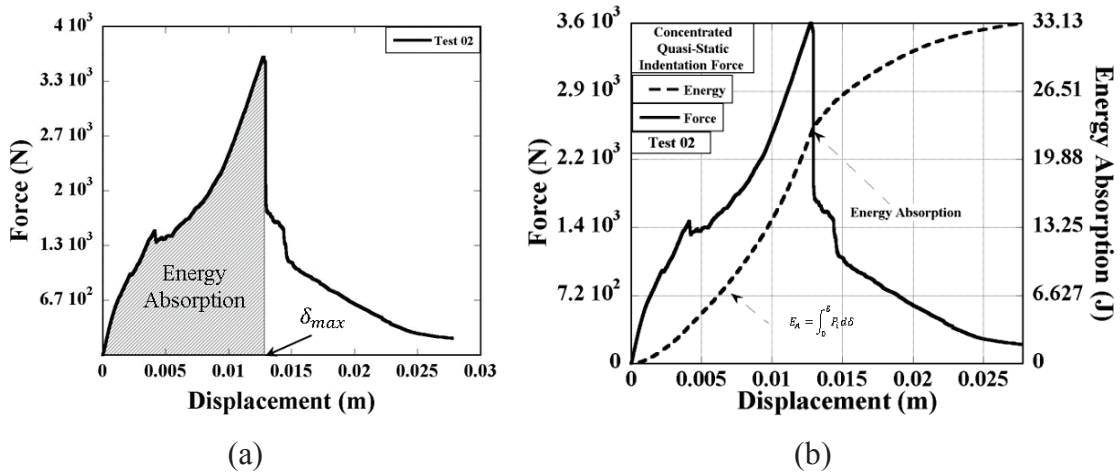
Figure 2.8. (a) force and (b) energy absorption versus displacement curves of a sandwich coupon subjected to the concentrated quasi-static indentation

34
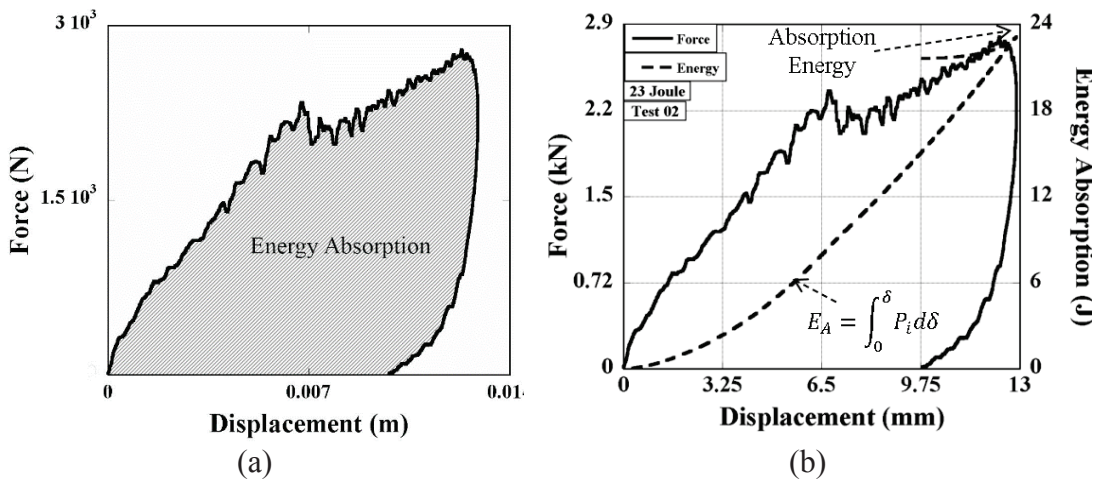
Figure 2.9. An example to half penetration: (a) the area under load-displacement and (b) the absorbed energy
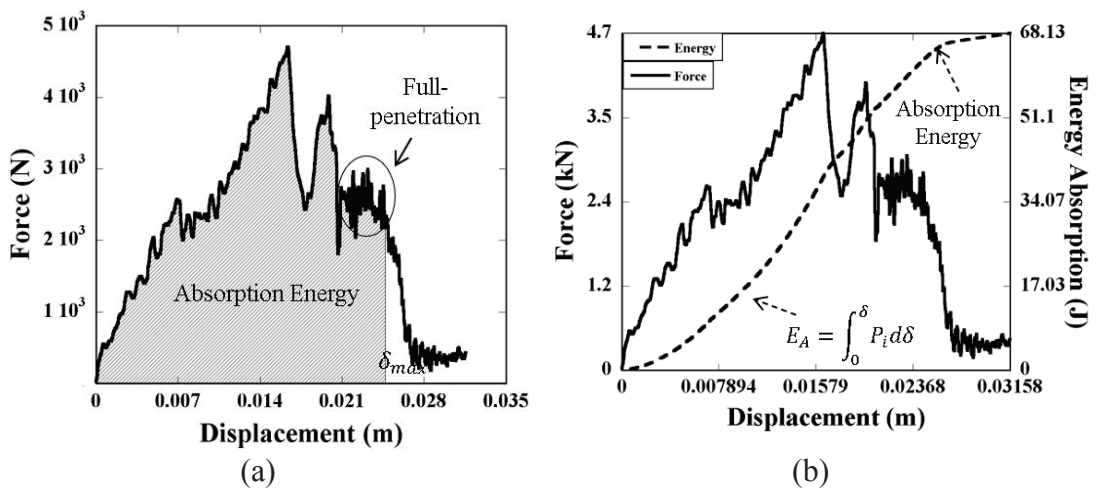
Figure 2.10. An example to a full penetration (a) the area under load-displacement and (b) the absorbed energy

Table 2.4. LVI test indenter mass, impact energy and impact velocity

Test Method	Mass (kg)	Label	E_i (J)	v_i (ms^{-1})	Test
Low-velocity Impact	5.7944	2.8 J Test 01	2.8	1	3
		2.8 J Test 02	2.8	1	
		2.8 J Test 03	2.8	1	
		5.5 J Test 01	5.6	1.4	3
		5.5 J Test 02	5.5	1.4	
		5.5 J Test 03	5.5	1.4	
		11 J Test 01	11	2	3
		11 J Test 02	11	2	
		11 J Test 03	11	2	
		22.5 J Test 01	22.5	2.8	3
		22.5 J Test 02	22.5	2.8	
		22.5 J Test 03	22.5	2.8	
		33.5 J Test 01	33.5	3.4	3
		33.5 J Test 02	33.5	3.4	
		33.5 J Test 03	33.5	3.4	
		39 J Test 01	39	3.7	1
		44.5 J Test 01	44.5	3.9	3
		44.5 J Test 02	44.5	3.9	
		44.5 J Test 03	44.5	3.9	
		56 J Test 01	56	4.4	3
		56 J Test 02	56	4.4	
		56 J Test 03	56	4.4	
		67 J Test 01	67	4.8	3
		67 J Test 02	67	4.8	
		67 J Test 03	67	4.8	

2.8. Compression after Impact Tests

The residual strengths of the intact and impacted sandwich coupons were determined by in-plane compression using compression after impact (CAI) test fixture in accord with ASTM D7137 / D7137M - 17. The schematic of the CAI test fixture is shown in Figure 2.11a. The same sample size was used in the CAI test with indentation tests. The coupons are placed in the CAI fixture, as shown in Figure 2.11b and compressed at a crosshead speed of 1.27 mmmin^{-1} in a Shimadzu Universal Test machine. The displacement was measured using a video extensometer (Figure 2.11b). A preload of 50 N was applied to ensure the contact between the CAI fixture, the sandwich coupon, and the compression test plate. Two cameras were used to record the failure modes of the

front and back face sheet of the sandwich coupons during the CAI test. The tests were stopped when the force dropped by 30% to detect the primary failure mode. The residual strength (σ_{CAI}) is

$$\sigma_{CAI} = \frac{P^{max}}{w\,t} \qquad (2.3)$$

where P^{max} is the maximum in-plane load, w and t are the width and thickness of the sandwich coupon. Normalized residual strength (NRS) is the decrease of the CAI strength of intact coupons compared to undamaged coupons. NRS is

$$NRS = \frac{\sigma_{CAI}^{Damaged}}{\sigma_{CAI}^{Intact}} \qquad (2.4)$$

where, σ_{CAI}^{Intact} is the CAI strength of intact coupon and $\sigma_{CAI}^{Damaged}$ is the CAI strength of the impacted coupon.
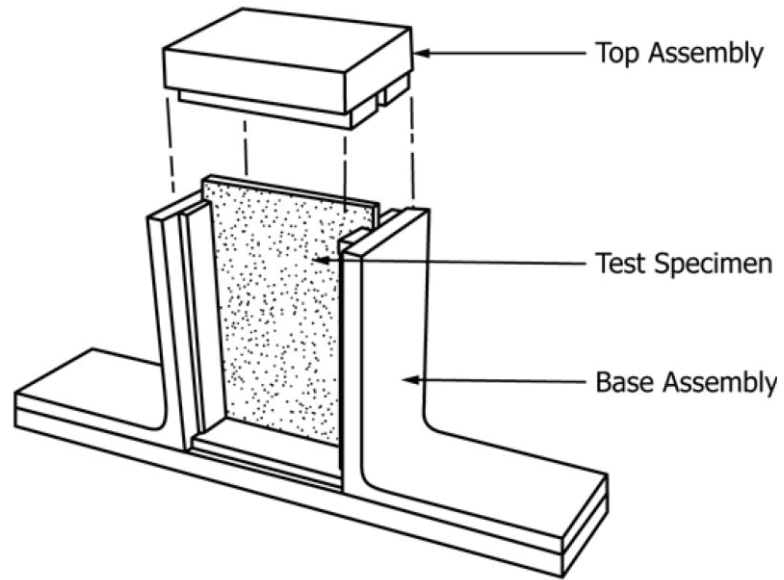
(a)
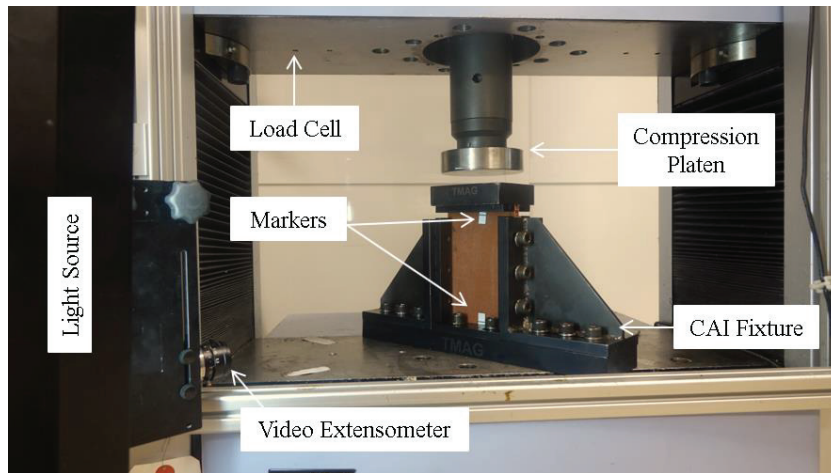
(b)

Figure 2.11. (a) the schematic of compressive residual strength support fixture [39] and (b) CAI test set-up

CHAPTER 3

RESULTS AND DISCUSSION

3.1. Concentrated Quasi-Static Indentation Force

Figure 3.1a shows the representative concentrated quasi-static indentation force and energy versus displacement curves of the tested sandwich coupons. The indentation force-displacement curve is mainly divided into three stages: between 0-A, A-B and B-C, as shown in Figure 3.1a. The damages will be explained sequentially in these stages.

In Stage-I (0-A), the load increases linearly with the displacement until A_0, as shown in Figure 3.1b, with no visible damage up to 0.6 kN. The sandwich structure shows a near-linear elastic behavior until A_0 (Figure 3.1b). The slope of the load-displacement curve is then reduced by 45% until point A_1. The reduction in the stiffness is partly due to the indenter forming initial tensile damage on the front face sheet or initiating a compression deformation of the Nomex core or both occurring simultaneously. The penetration of indenter to the front face sheet starts at about the first peak-force F_1, as shown in Figure 3.1a. Similar observations were also made previously on similar sandwiches [82-85]. The corresponding energy absorption at F_1 is designated as E_1 in Figure 3.1a. In Stage-II (A-B) the first peak-force drops at point A by approximately 10%, and the load fluctuates around a constant force value (Figure 3.1c). The fluctuation is again caused by the damage formation at the front face sheet and core crushing. After that, the indentation force is transferred to the back face sheet. Subsequently, debonding occurs at the interface between the back face sheet-core [82-85]. The full-penetration of the front face sheet occurs when the maximum load (F_{max}) is reached. Before the maximum load, the visible damage (delamination) on the back face sheet is seen. In Stage-III (BC), the load drops suddenly due to full-penetration of the front face sheet, after F_{max}. The corresponding energy absorption at F_{max} is the maximum absorbed energy designated as E_{max}.

Figures 3.2a-3.2c show the force and energy absorption displacement curves and front and back face sheet deformation pictures of three quasi-static indentation tests,

respectively. In all tests, similar fracture modes of the front and back face are seen. The damage areas are similar at the front and back face sheets, as seen in the same figures. The typical damage formed includes fiber and matrix fracture and delamination. The damage is also noted to be larger at the back face sheet in Figures 3.2a-3.2c. In the elastic region, the slope is about 0.65 kN mm^{-1} for all three tests. The values of E_{max} and E_1 are drawn as a function of F_{max} and F_1 in Figure 3.3 for all tested coupons. The statistical analysis results of the test are also shown in the same figure for E_1 and E_{max}. The mean values of E_1 and E_{max} are 4 and 20 J, respectively. E_{max} range 18-22.5 J and E_1 3.5 J-5 J.

F_1	1512.5 N	E_1	3.63 J	$Disp_1$	4.15 mm	t_1	199"
F_{VD}	3545.9 N	E_{VD}	21.58 J	$Disp_{VD}$	12.56 mm	t_{VD}	603"
F_{max}	3624.1 N	E_{max}	22.32 J	$Disp_{max}$	12.77 mm	t_{max}	613"
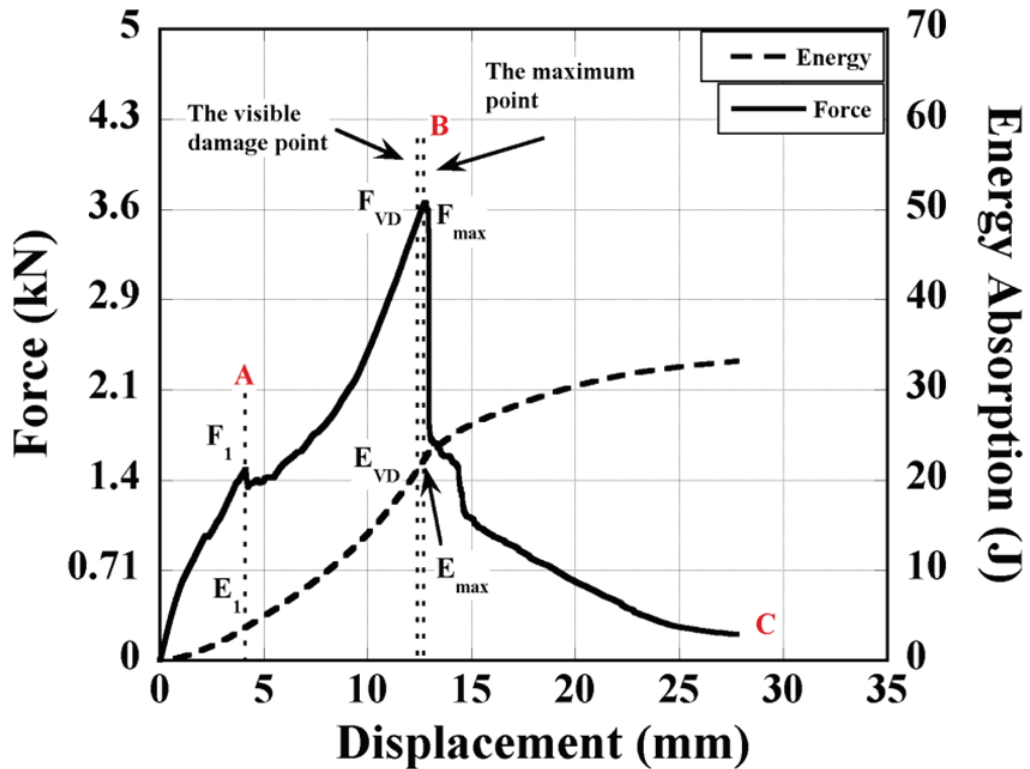
(a)

Figure 3.1. (a) representative force and energy absorption versus displacement curve of quasi-static indentation, (b) between 0-4.2 mm, and (c) between 4.2-12.5 mm displacements

(b)

(c)
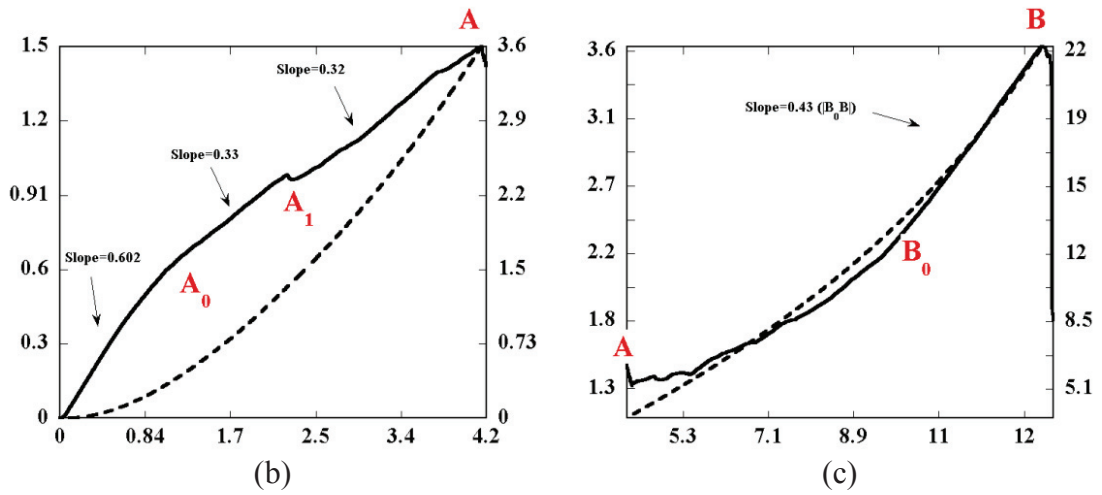
Figure 3.1. (cont.)
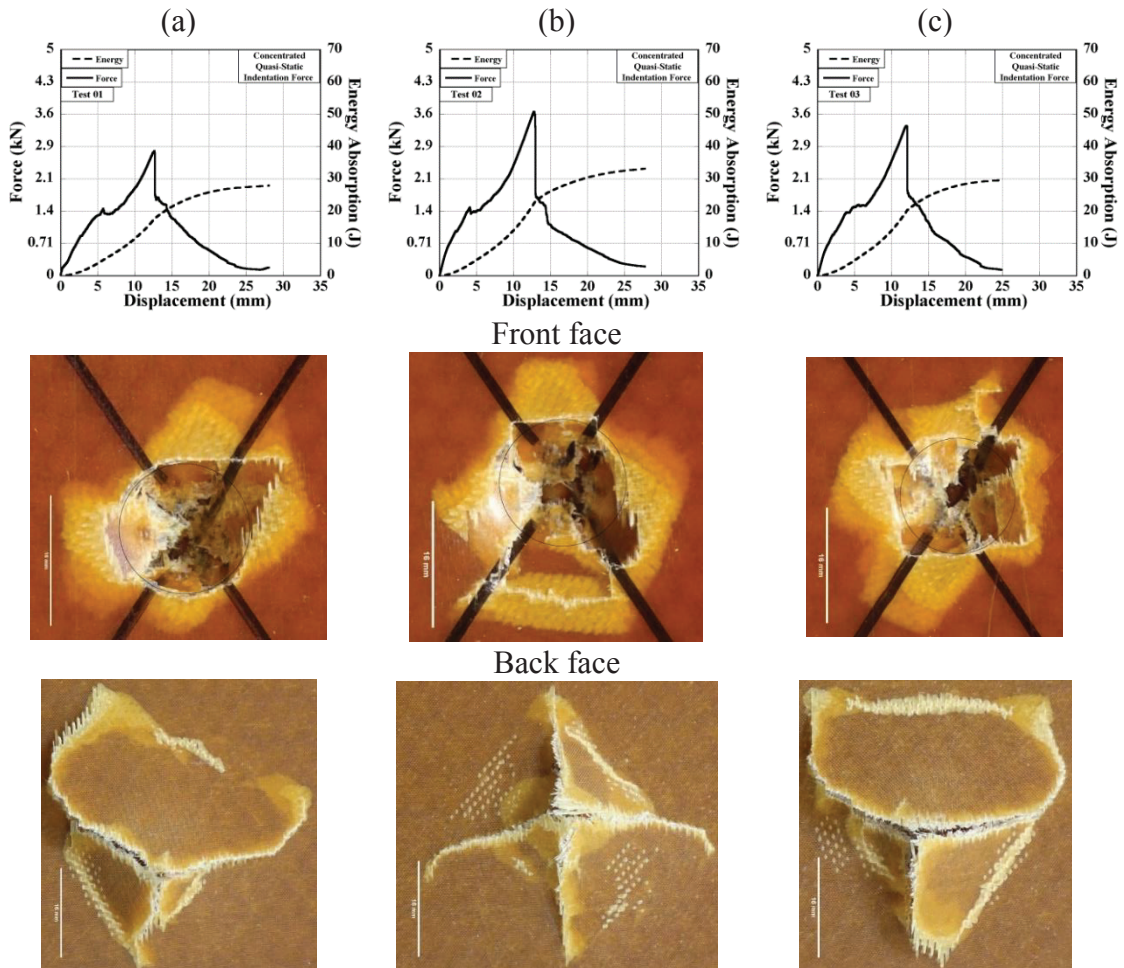
Figure 3.2. The load and energy absorption displacement curves and front and back face sheet pictures of three quasi-static indentation tests: (a) test-1, (b) test-2 and, and (c) test-3
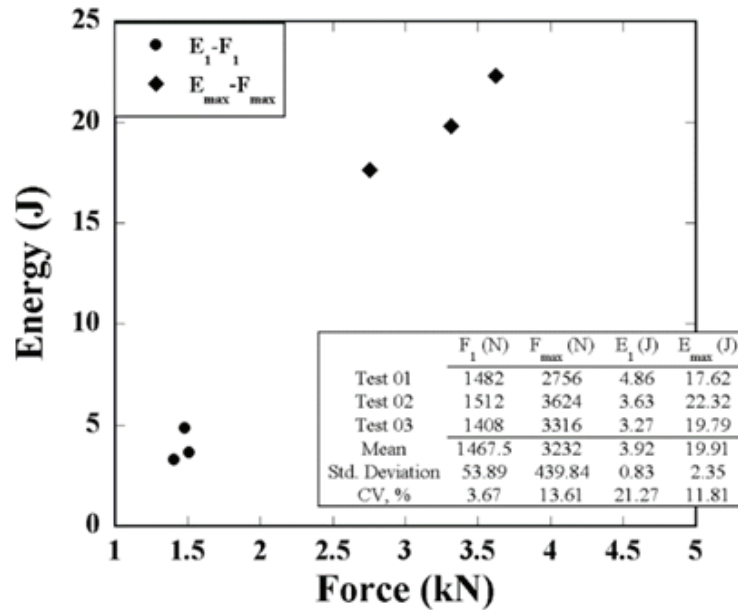
Figure 3.3. The variation of E_1 and E_{max} with F_1 and F_{max} of the coupons subjected to the quasi-static indentation test

3.2. Low-velocity Impact Tests

Figure 3.4a shows the representative LVI test force and energy absorption versus displacement curve of the full-penetrated sandwich coupon. The curve is again divided into three stages, as will be explained below.

Stage-I (0-A) in Figure 3.4a is very similar to the Stage-I of the quasi-static indentation, while the slope of the curve in the elastic region is higher than that of the quasi-static indentation test due to higher strain rates involved in the DW test. The force oscillations are seen in Figure 3.4b in this region result from the stress wave reflections from the back face sheet. Similar to the quasi-static indentation the penetration of the front face sheet by the indenter and core crushing occurs at the first peak-force F_1. Stage-II (A-D) is very similar to the Stage-II of the quasi-static indentation, but the behavior is dominated by the flexural waves and shear responses. Therefore, the dominant damage failure modes are the global core shear, face sheet/core debonding when the maximum force is reached (Figure 3.4b). After that, the load sharply drops to the first peak load value, and the impactor impinges on the back face sheet with an increase in force (Figure 3.4c). The load fluctuates as the impactor impinges on the back face sheet, and the steady

load is due to the penetration of the impactor to the back face sheet. The contact friction effect between the impactor and the failed front face sheet and the sandwich coupon's core results in load fluctuations.[82-85] The first peak force is equal to 2.57 kN, and the back face sheet rupture occurs at an average force of 2.55 kN (Figure 3.4e). In Stage-III (D-E), the load drops suddenly due to full-penetration. The pictures of the response of test coupons to the DW test are shown in Figures 3.5a and 3.5b. In these pictures, the flexural and shear responses of the tested coupon are clearly seen. Not that the flexural response is absent in the case of the quasi-static indentation, as seen in Figures 3.5c and 3.5d.
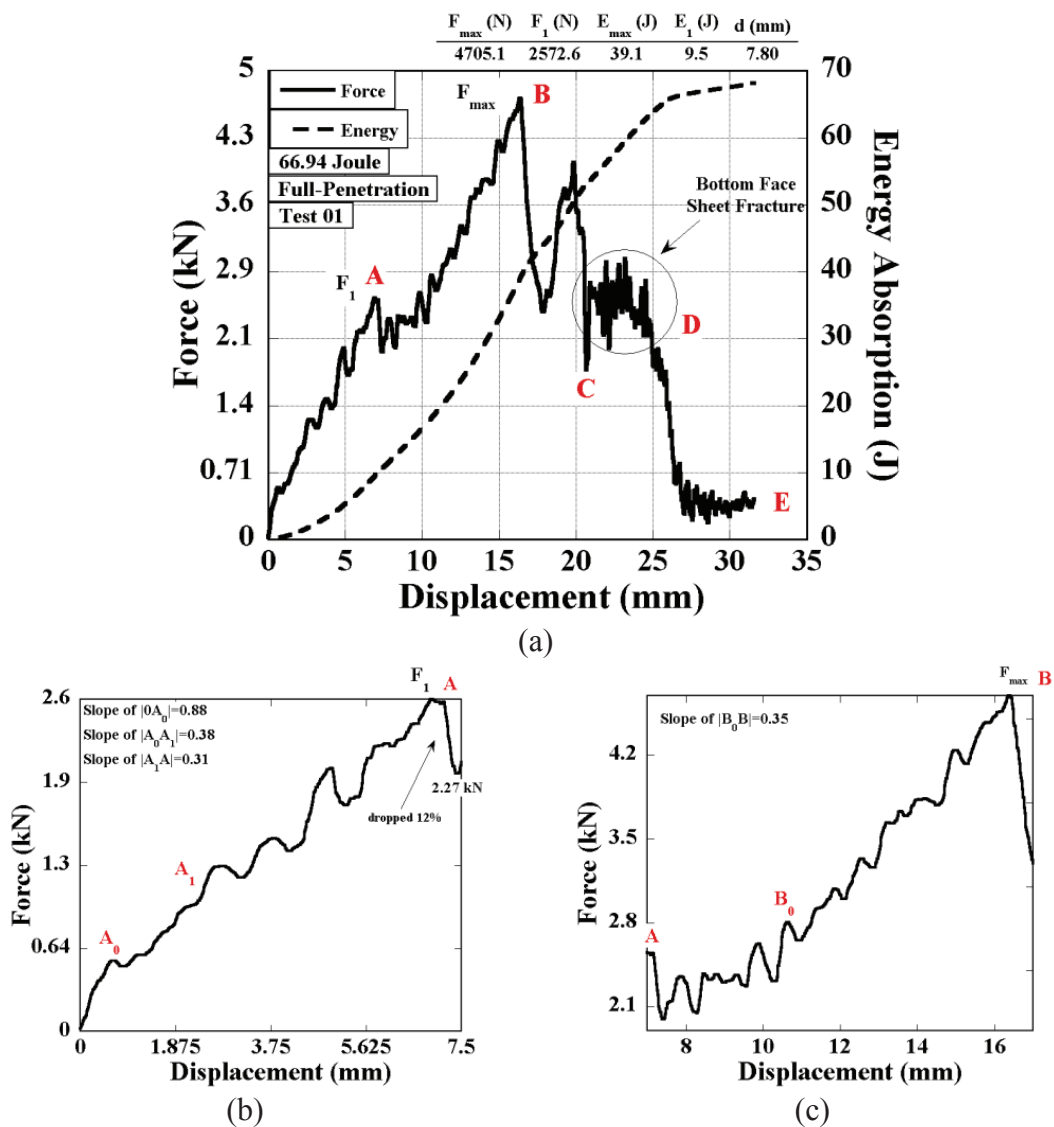
Figure 3.4. (a) Force and energy absorption versus displacement curves of the coupon presented full-penetration at 67 J and force-displacement curves (b) between 0.7-5 mm, (c) between 7-17 mm, (d) between 17-21 mm, and (e) between 20-25 mm

(d)

(e)

Figure 3.4. (cont.)

v:3.16 ms^{-1} — Displacement: 16.4 mm

(a)

Core Shear

v:3.01 ms^{-1} — Displacement: 17.8 mm

(b)

Displacement: 12.8 mm

(c)

Displacement: 13 mm

(d)
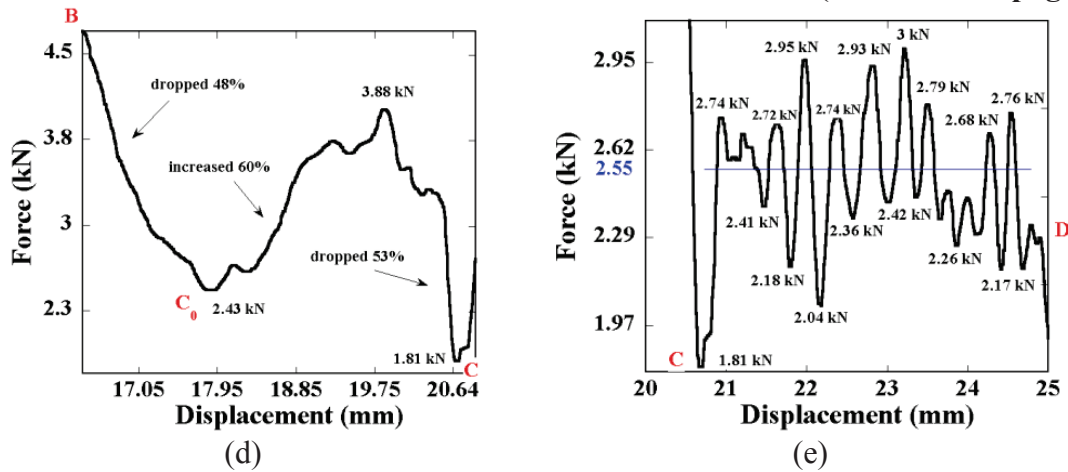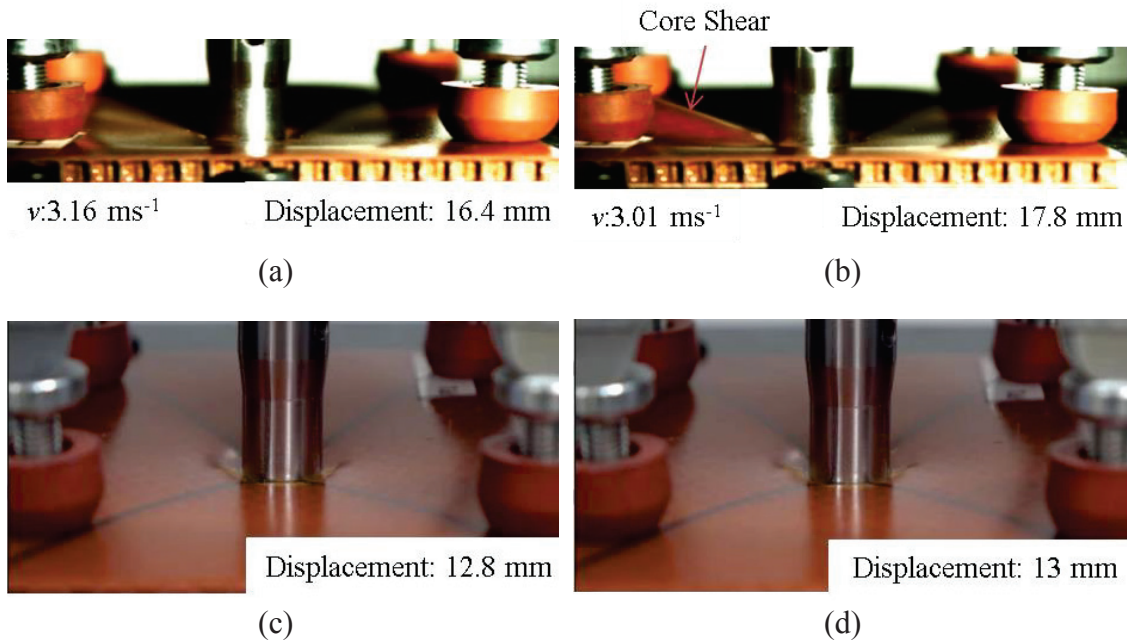
Figure 3.5. The pictures of DW tests Figure (a) and b) shows flexural and shear responses, c), and d) shows a quasi-static behavior response at maximum force

Figures 3.6a and 3.6b shows the force and energy absorption-displacement curves and the front face sheet indentation pictures of the three coupons tested at 2.8 and 5.5 J, respectively. The impact damages at 2.8 and 5.5 J can be categorized as BVID since the measured dent depth is less than 1 mm and the maximum force is less than the first force-

peak at which the indenter penetrates the front face sheet. However, there is delamination type damage at the impact zone of the front faces sheets of the coupons, as seen in Figures 3.6a and 3.6b. However, the delamination zone is more extensive in the coupon tested at 5.5 J than in the coupons tested at 2.8 J. Figures 3.7a-3.7c show the force and energy absorption-displacement curves and the front face indentation pictures of the coupons tested at 11, 22.5 and 33.5 J, respectively. The fracture modes of the front face sheets at three different energy levels are very similar, with an X-shape damage, and no visible damage is detected at the back face sheet until 33.5 J. The tests at 11, 22.5 and 33.5 J can be categorized as the low-energy level since the force is not reached the second force peak at which the indenter starts to penetrate the back face sheet. The values of F_{max}, F_1, E_{max}, E_1, and the dent-depth and damage planar area of the front face sheet increase as the energy increases from 11 to 33.5 J. The back face sheet damage becomes visible in the form of localized fiber splitting when the impact energy is increased to 39 J, as seen in Figure 3.8a. Fiber fracture and delamination are seen in the front face sheet, again with an X-shape. The forces in the tests at 44.5, 56 and 67 J are above the second peak force, and therefore they are categorized as the high-energy impact tests (Figures 3.8b-3.8d). At 44.5 J, two tests show splits/cracks at the back face sheet, while one test shows no visible damage at the back face sheet (Figure 3.8b). Only in one test, the back face sheet shows a fracture at 56 J (Figure 3.8c). One coupon exhibits puncture at the back face sheet, while the other two display splits/cracks at the back face sheet at 67 J (Figure 3.8d).

Figures 3.9a-3.9f show the high-velocity impact test pictures of the impactor and sandwich front face sheet before, at contact and after impact at different energy levels and velocities. After the impact, the impactor rebounds and a near planar impact with the X-shape damage formed on the front face sheets are clearly seen in these pictures.

Front face sheet

(a)

Front face sheet

(b)
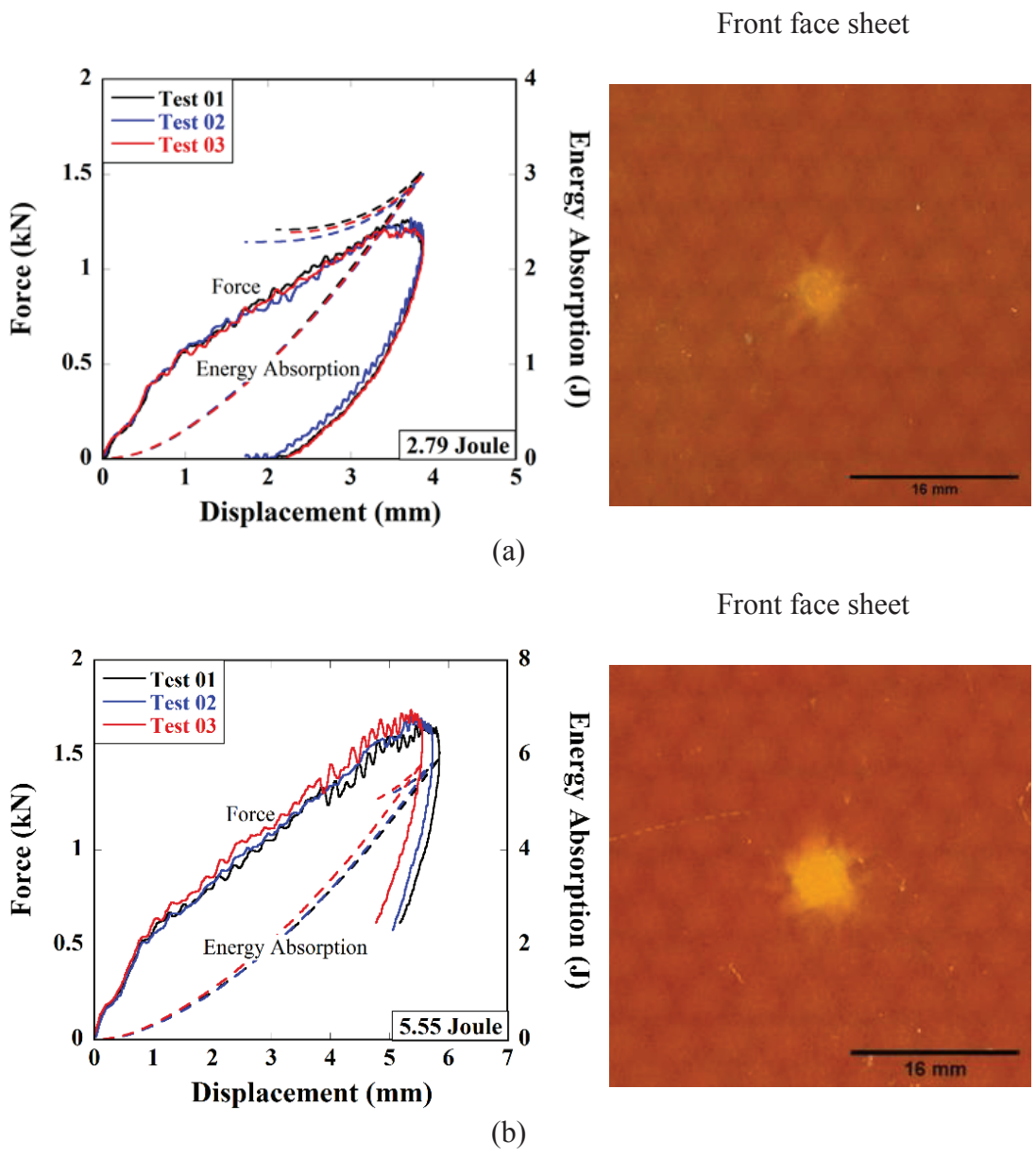
Figure 3.6. Force and energy absorption curves and the front face indentation deformation pictures of the coupons tested at (a) 2.8 J and (b) 5.5 J
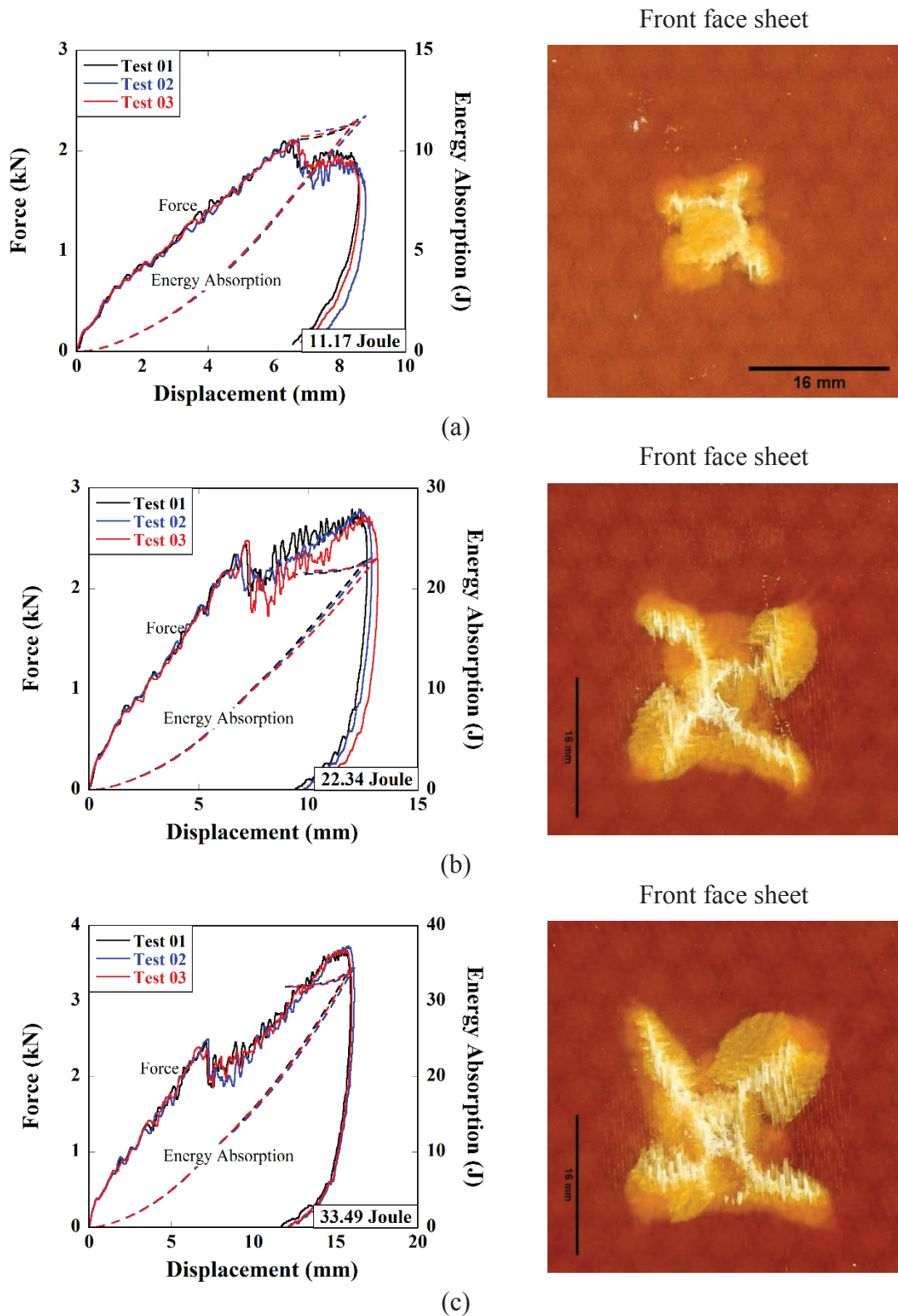
Figure 3.7. Force and energy absorption curves and the front face indentation
deformation pictures of the coupons tested at (a) 11 J, (b) 22.5 J, and (c)
33.5 J
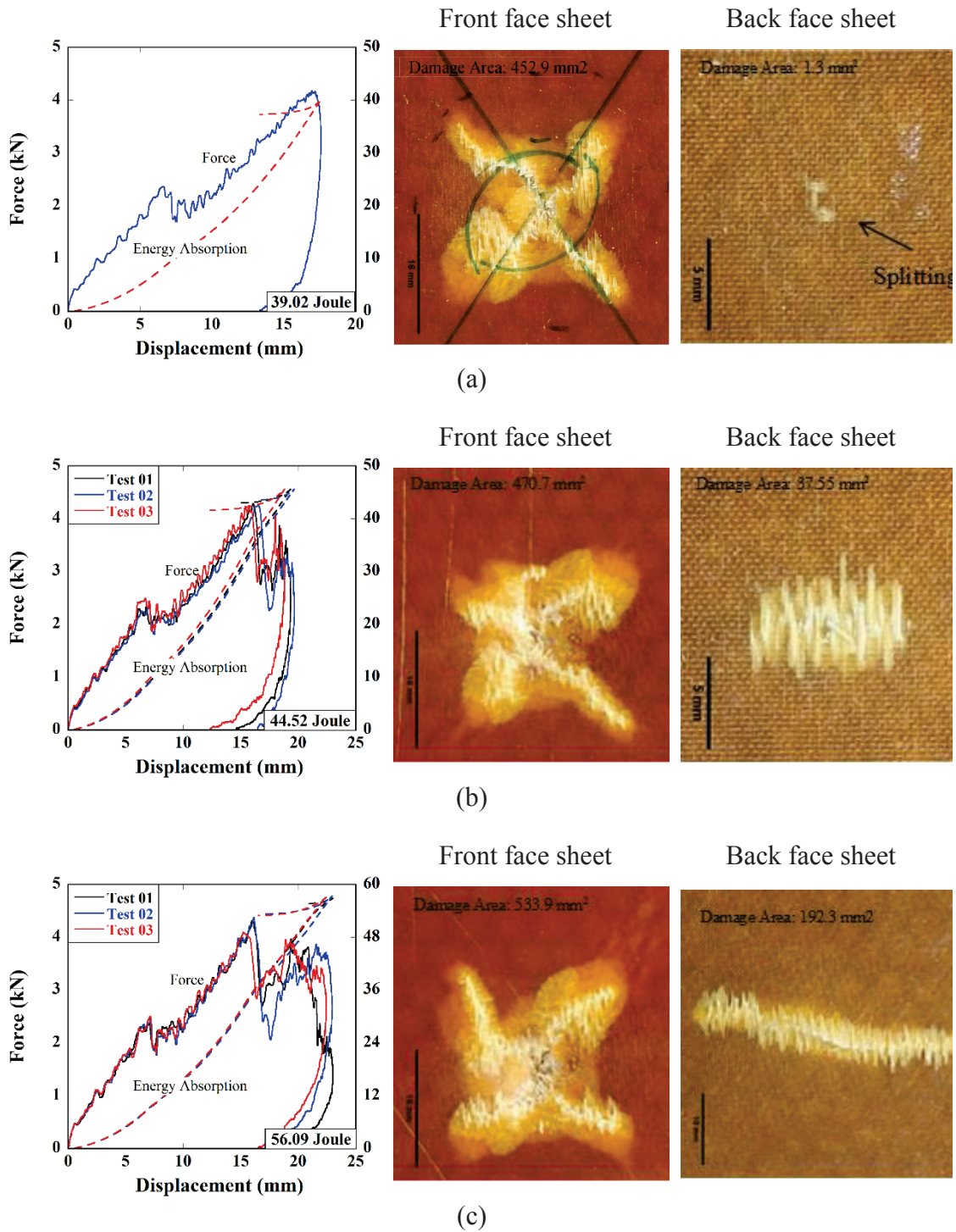
Figure 3.8. Force and energy absorption curves and the front face indentation deformation pictures of the coupons tested at (a) 39, (b) 44.5 J, (c) 56 J, and (d) 67 J

(cont. on next page)

Front face sheet   Back face sheet

(d)

Figure 3.8. (cont.)

Before   Contact   After

(a)

(b)

(c)
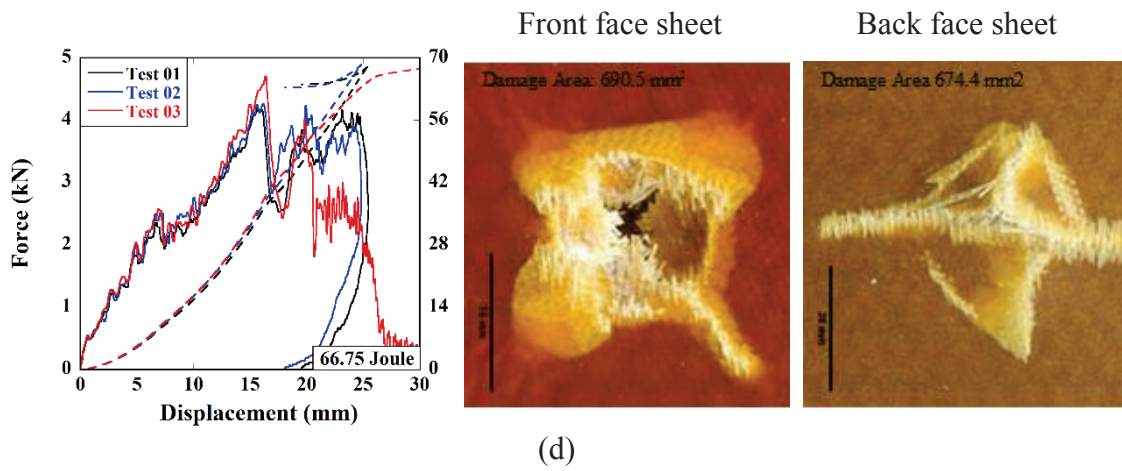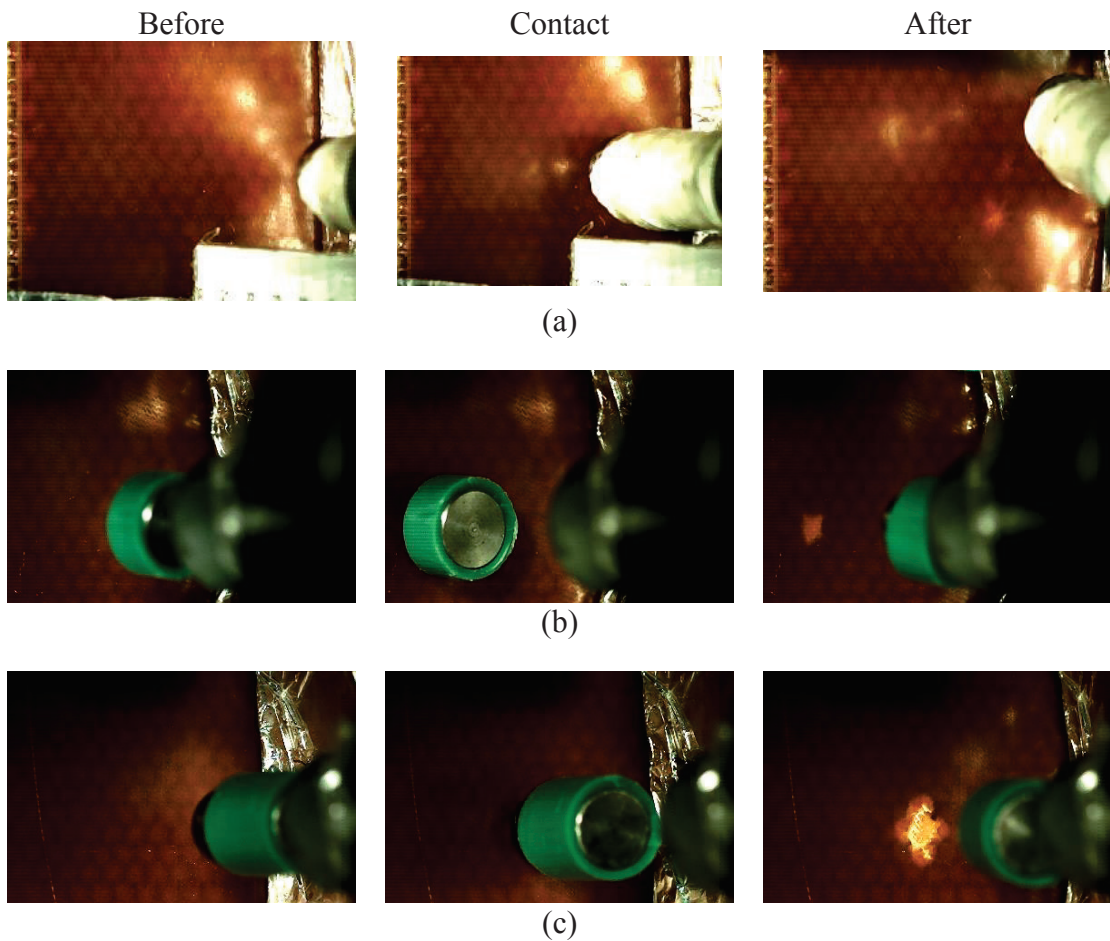
Figure 3.9. The pictures of high-velocity impact tests before, at contact and after the impact at (a) 2.8 J (14.5 ms^{-1}), (b) 5.5 J (20.5 ms^{-1}), (c) 11 J (19.5 ms^{-1}) (d) 11 J (29.5 ms^{-1}) and (e) 22.5 J (28 ms^{-1}), and (f) 33.5J (28 ms^{-1})

(cont. on next page)

49

(d)

(e)

(f)
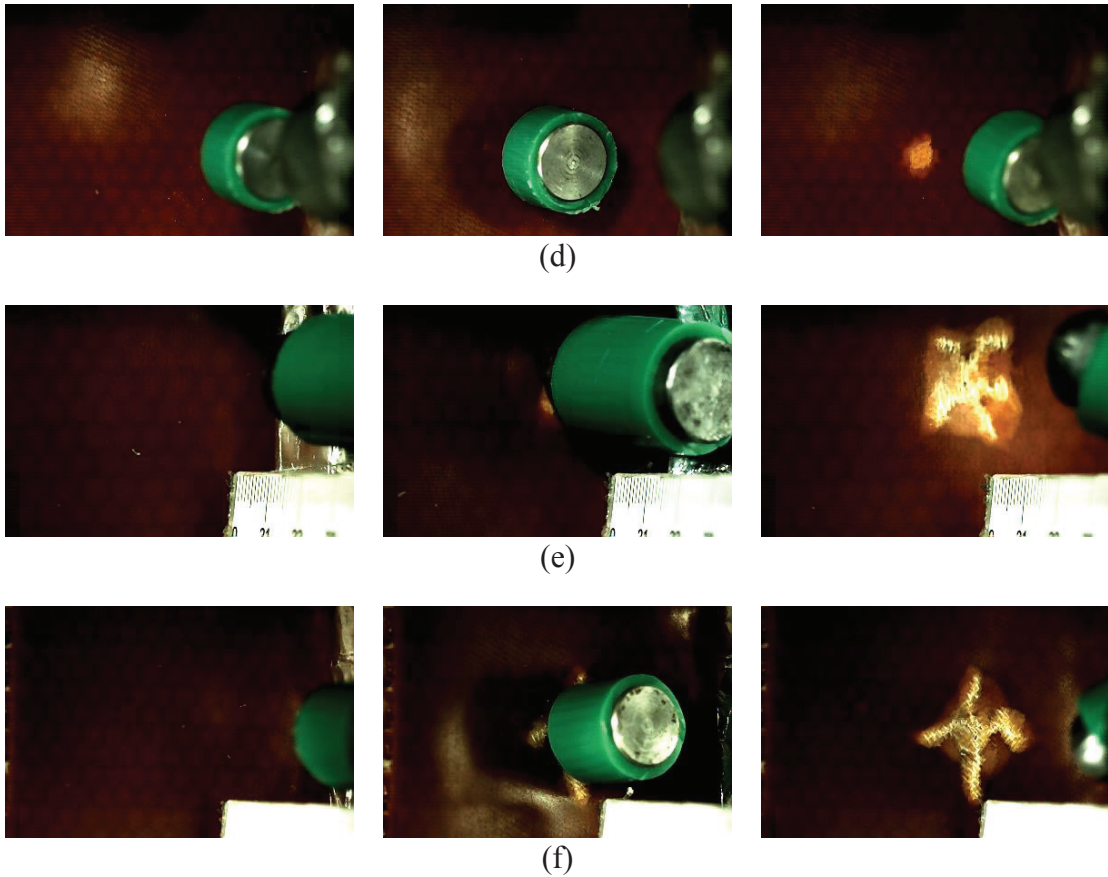
Figure 3.9. (cont.)

3.3. Force and Energy Absorption Analysis

The variations of F_1 and F_{max} and E_1 and E_{max} with the impact energy are shown in Figures 3.10a and 3.10b, respectively. Except for the F_1 and E_1 values of the coupons tested at 11 J are slightly lower than the tests at higher energies, the values of F_1 and E_1 do not change significantly at increasing impact energies in the LVI tests, as seen in Figures 3.10a and 3.10b. On the other side, the F_{max} and E_{max} values increase linearly until about 40 J (the back face sheet penetration); thereafter, they remain almost constant at increasing impact energies (Figures 3.10a and 3.10b). The LVI test mean values of F_1, F_{max}, E_1 and E_{max} are further tabulated in Table 3.1. The mean values of F_{max} and E_{max} are calculated after about 40 J in this table. The mean values of E_1 and E_{max} are 10 (7.5 J-10 J) and 33 J (32.5-39 J), respectively. Also, the LVI test values of F_1, F_{max}, E_1 and E_{max} are higher than those of the quasi-static indentation test, as seen in Figures 3.10a and 3.10b.

Note that the values of F_1 and E_1 depend on the penetration of the front face sheet, while the values of F_{max} and E_{max} are controlled by the core shear. Furthermore, the mean slope of the force-displacement curves of the LVI tests in the elastic region is 0.92, and this value decreases to 0.64 in the quasi-static indentation test. This is due to the high-strain rate effect on the face sheet deformation and bending behavior of the sandwich structure.
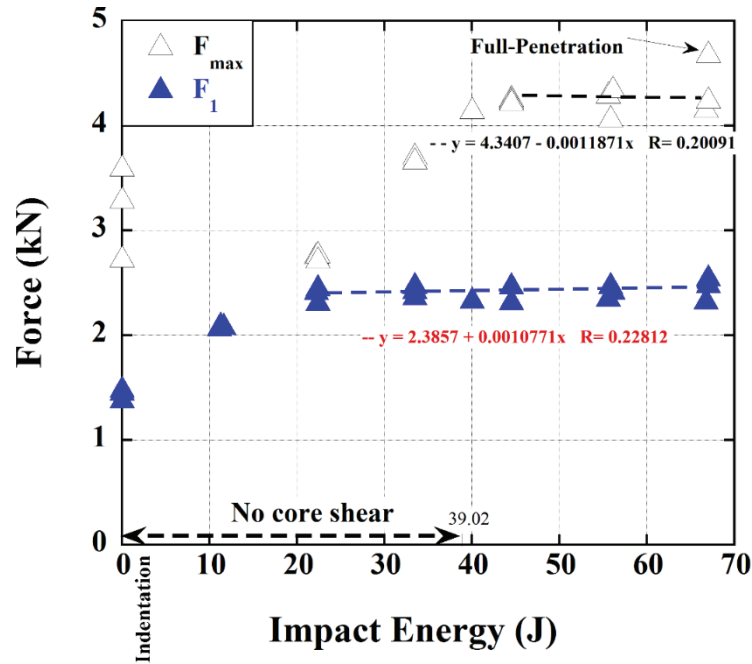
(a)
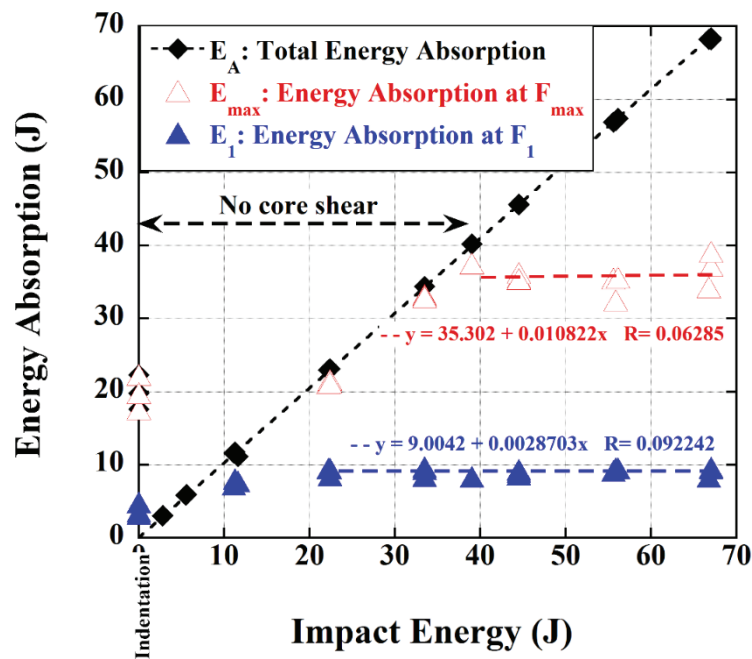
(b)

Figure 3.10. (a) F_1 and F_{max} and (b) E_1 and E_{max} versus impact energy

Table 3.1. The mean F1, Fmax,E1 and Emax values of the LVI tests

	F_1	F_{max}	E_1	E_{max}
Minimum	2	4	7.5	32.5
Maximum	2.5	4.5	9.5	39
Average	2.5	4.5	9.5	33
Std. Deviation	0.14	0.17	0.71	5.88
CV, %	6	4	7.5	18

3.4. Compression after Impact

The residual compressive strength versus strain curves of the intact and the LVI and quasi-static indentation force tested coupons are shown in Figures 3.11a-3.11j at different impact energy levels. The maximum stresses in this curve are taken as the CAI strengths. As noted in the same figures, the in-plane strength of the intact sandwich (~50 MPa) is inherently higher than those of the damaged coupons. As the impact energy increases, the CAI strength of sandwiches decreases, while a higher rate of the strength reduction in the strength is seen until about 10 J, at which the front face sheet is started to be penetrated by the indenter. It is also noted that the fully-penetrated quasi-static indentation test sandwiches show higher CAI strengths than the fully-penetrated LVI test sandwiches (Figures 3.11i and 3.11j). Residual strength is also seen after full penetration, and the penetrated sandwiches continue to provide some resistance to the compression loading [67, 68].

Figures 3.12a-3.12e show the CAI stress-strain curves of the LVI and HVI tested sandwiches coupons at similar impact energy levels. The impact velocity is seen not to significantly affect the CAI strength values of the tested coupons, except the HVI tested coupon shows a slightly higher mean CAI strength at 5.5 J (Figure 3.12b). But at increasing impact energies, both LVI and HVI tests result in almost similar CAI strength values with the studied velocity range as seen in Figures 3.12c-3.12e.
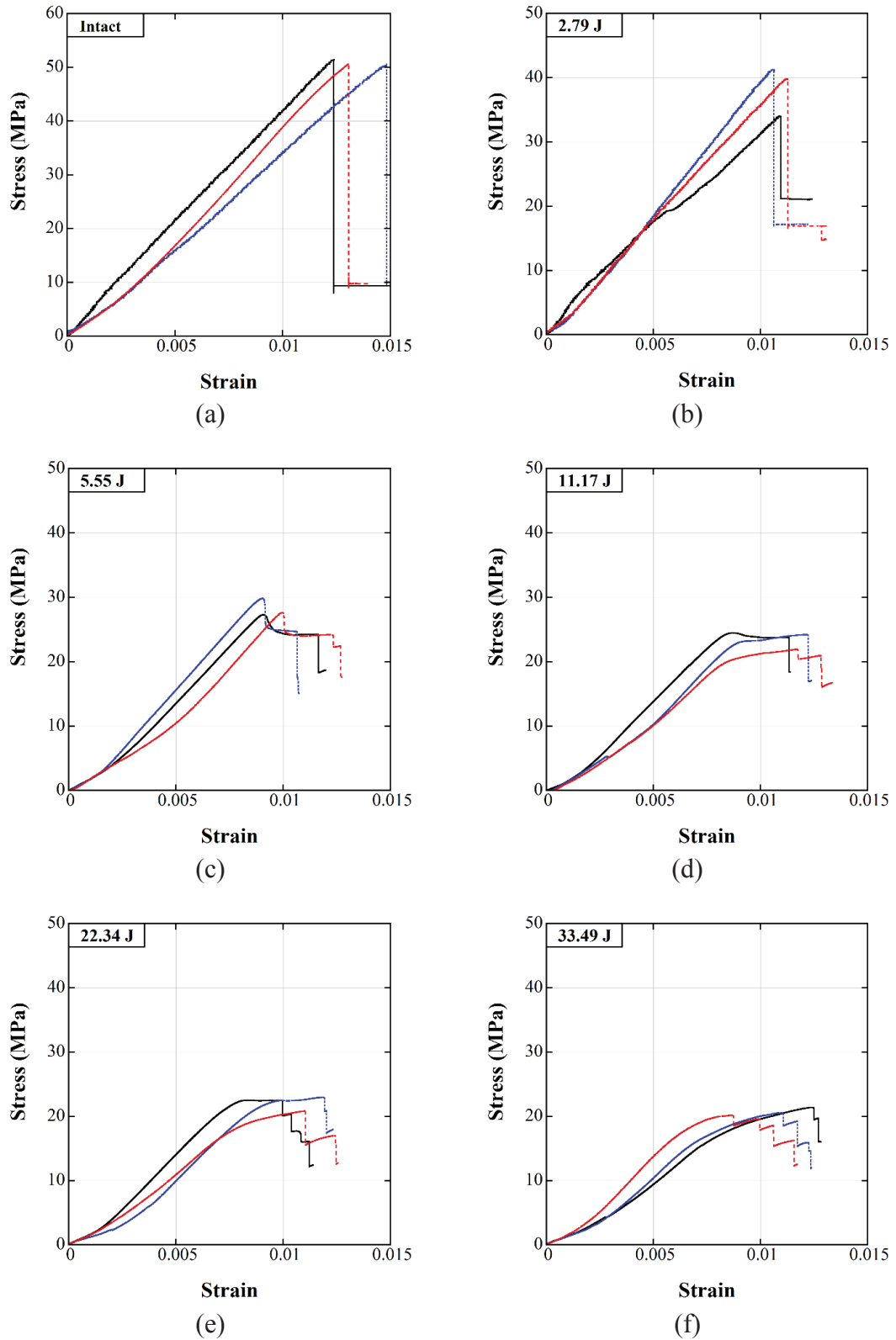
Figure 3.11. Stress-strain curves of the CAI tests of coupons (a) intact and (b) 2.8, (c) 5.5, (d) 11, (e) 22.5, (f) 33.5, (g) 44.5, (h) 56, (i) 67 J, and (j) indentation

(cont. on next page)
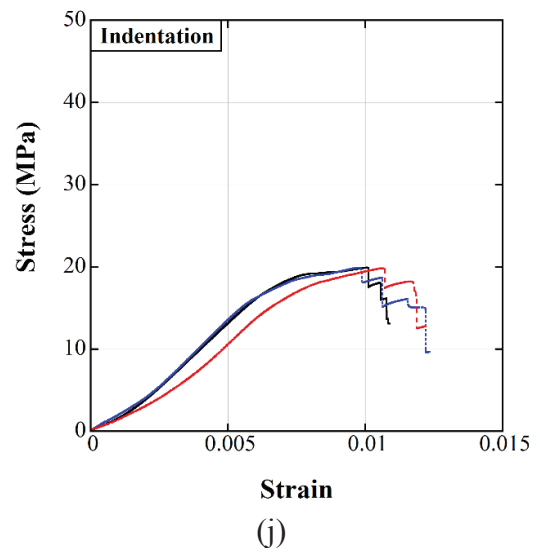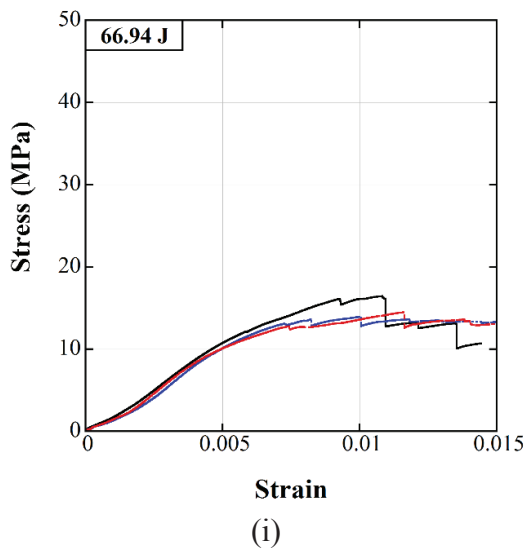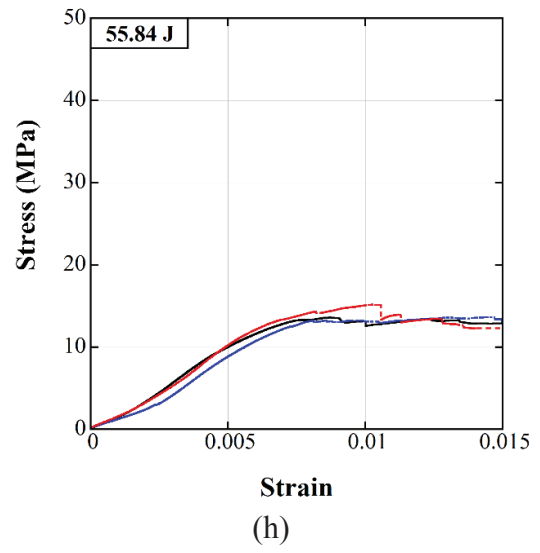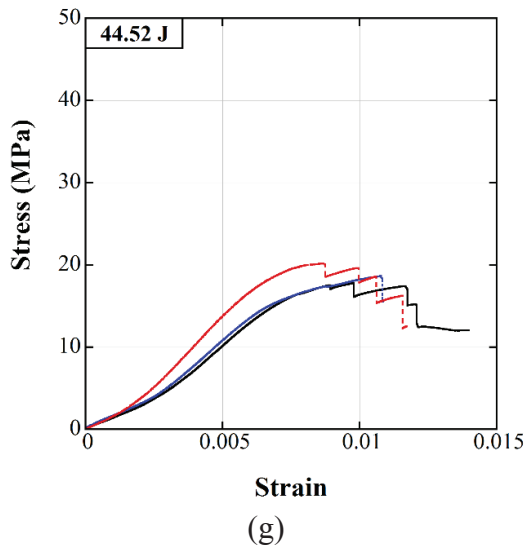
Figure 3.11. (cont.)
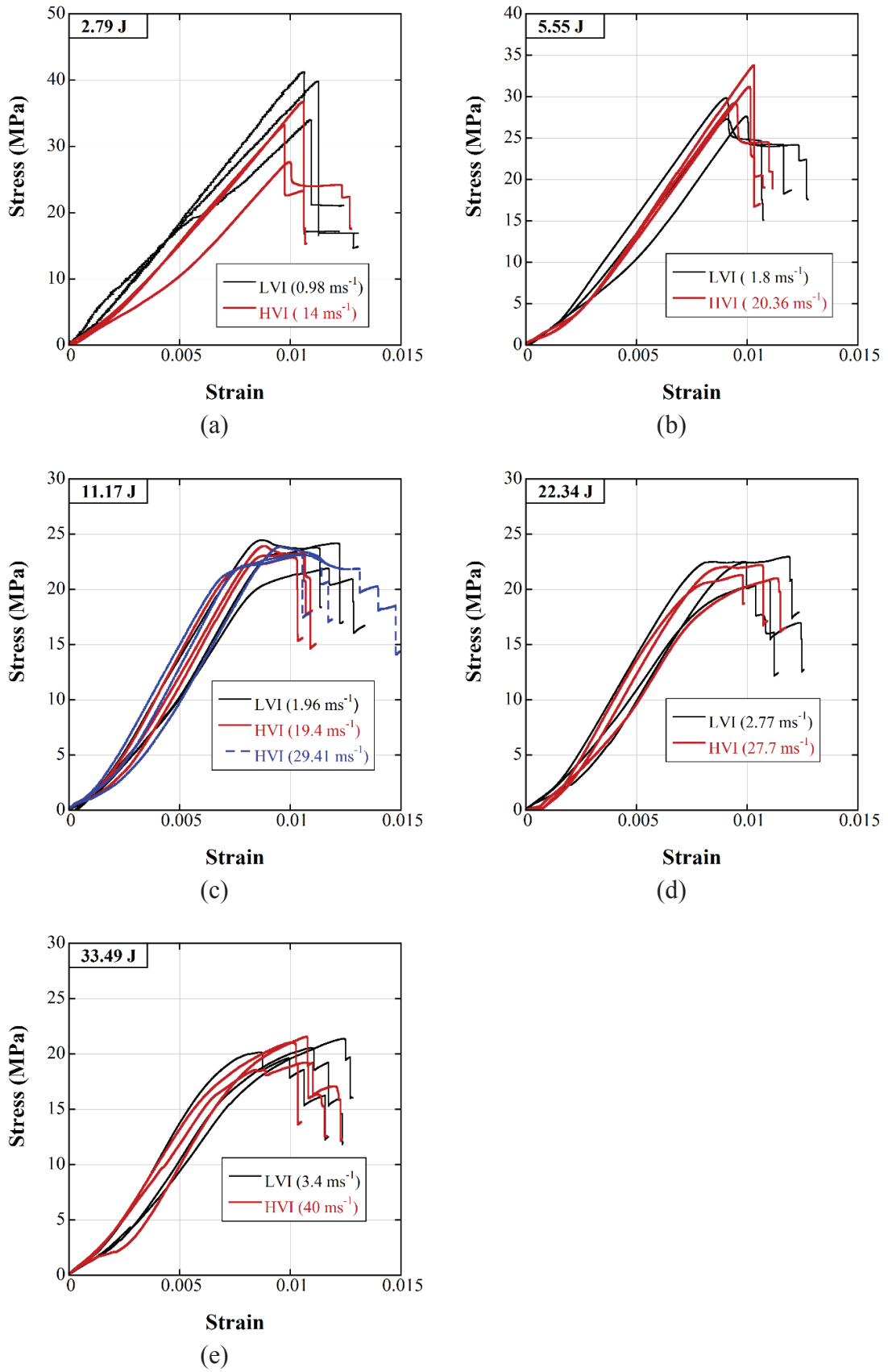
Figure 3.12. Stress-strain curves of the CAI tests of LVI and HVI test coupons (a) 2.8, (b) 5.5, (c) 11, (d) 22.5, and (e) 33.5 J

3.5. Damage Tolerances

The damage tolerances of the tested coupons are shown in Figure 3.13a as the normalized residual strength and residual strength versus impact energy. Figures 4.13b and 13c show the variations of the depth of dent and planar damage area with impact energy, respectively. Two characteristics are seen in Figure 3.13a. First, until about the front face sheet is started to be penetrated, 10 J, a catastrophic reduction of 60% is observed in the residual strength. The damage tolerance almost remains constant after the front face sheet penetration. Second, above 44.5 J, the flexural waves dominate, and global core shear is seen. The global shear plays a more role than full-penetration on the damage tolerance. A critical value of 10 J may be categorized as BVID. Above 11 J energy levels, damage tolerance behavior does not change due to the penetration of the front face sheet. Although no perforation is observed in the coupons subjected to 11 J impact at 30 ms^{-1}, their damage tolerance is similar to that of lower velocity impact tests (Figure 3.13a). Although the damage area does not decrease too much, residual strength increases at 5.5 J in the HVI test. At this energy level, the sandwich coupons subjected to HVI has more damage tolerances than the coupons subjected to low-velocity impact. But the same behavior is not observed at 2.8 J. Despite the damage area decreases slightly, there is a remarkable decreased in the residual strength at 2.8 J in the HVI test. While there is no remarkable growth in the damage area and the depth of dent until about 10 J, at which the front face penetration starts, the penetration of the front face sheet causes a sharp increase in the depth of dent and damaged area. The planar damage area on the front face sheet and residual dent increase with an increase in the impact energy until 39 J. When the impact energy is higher than 39 J, the planar damage area and residual dent slightly increase since the global core shear occurs. The planar damage area enlarges proportionally with an increase in the residual dent. For full-penetration, indentation force and low-velocity impact generated approximately the same damage area (Figure 3.13b).
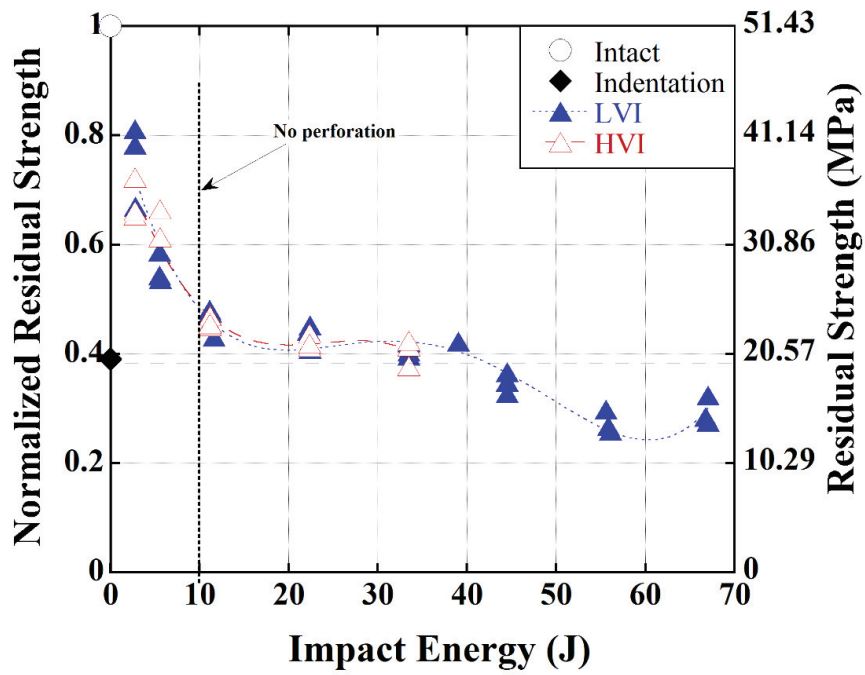
(a)
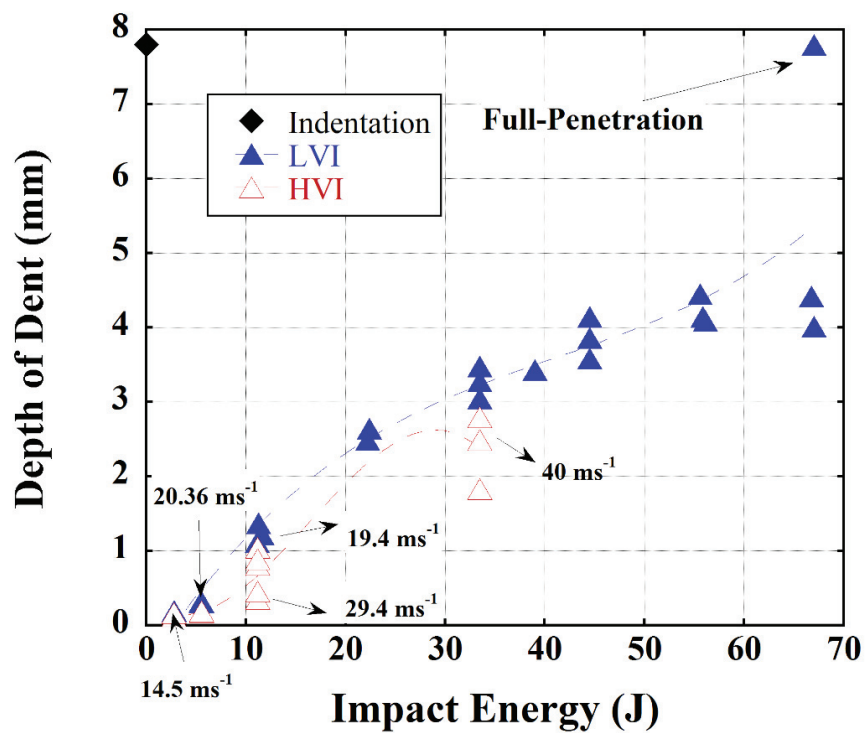
(b)

Figure 3.13. (a) Residual strength and normalized residual strength, (b) planar
damage and the (c) depth of dent versus impact energy

(cont. on next page)
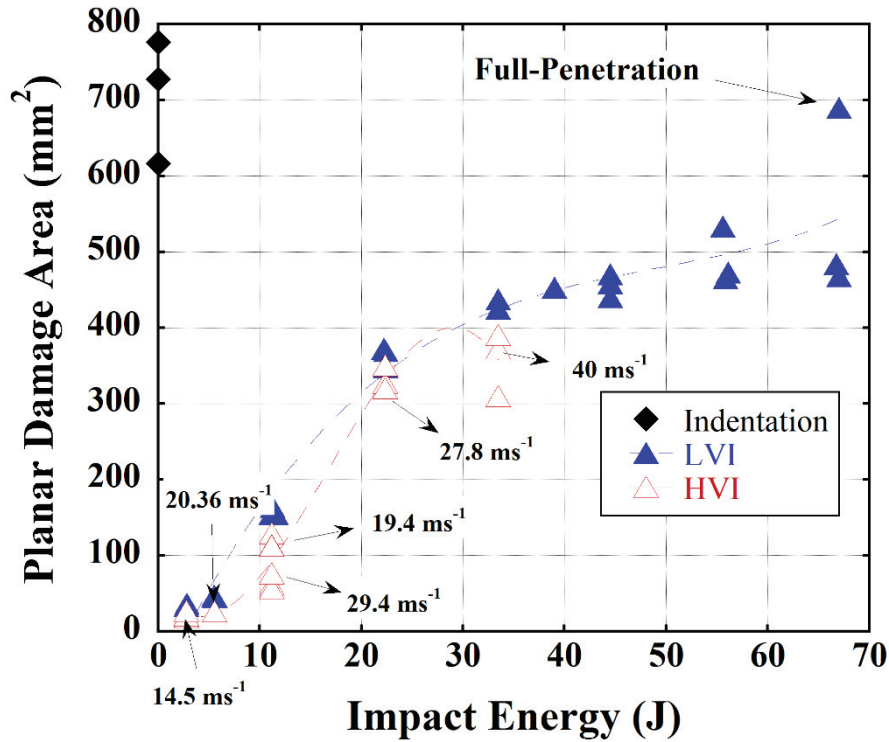
(c)

Figure 3.13. (cont.)

3.6. Damage Analysis

The impact damage of sandwich coupons is categorized in terms of the planar damage area and the residual dent, as shown in Figures 3.14a and 314b. The sandwich front face sheet failure modes exposed to quasi-static indentation force and LVI tests at 67 J are shown in Figures 3.15a and 3.16a, respectively. The sandwich coupons have the combined large cracks with fiber breakage and residual dent/indentation having sizes similar to the indenter diameter. The cracking and the delamination in the vicinity of indentation propagates cross-shaped through weaving fiber direction. The back face sheet's damage mode is dominated by matrix cracking, and fiber breakage propagates through weave directions as a tensile failure. The fiber splitting due to matrix failure is also seen.
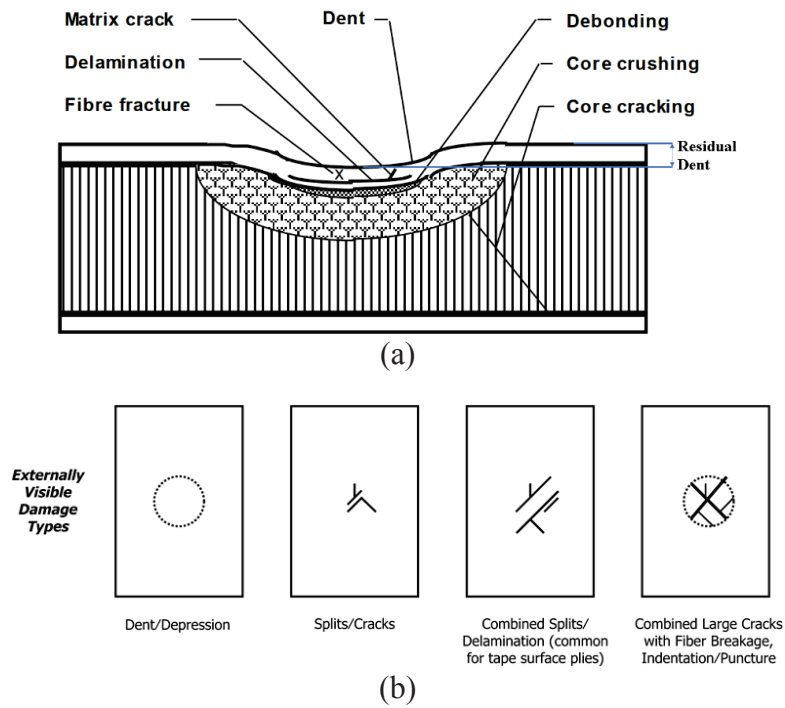
Figure 3.14. (a) The damage parameters of the sandwich coupon[65] and (b) ASTM D7136 / D7136M – 20 damage modes of the composite sheet
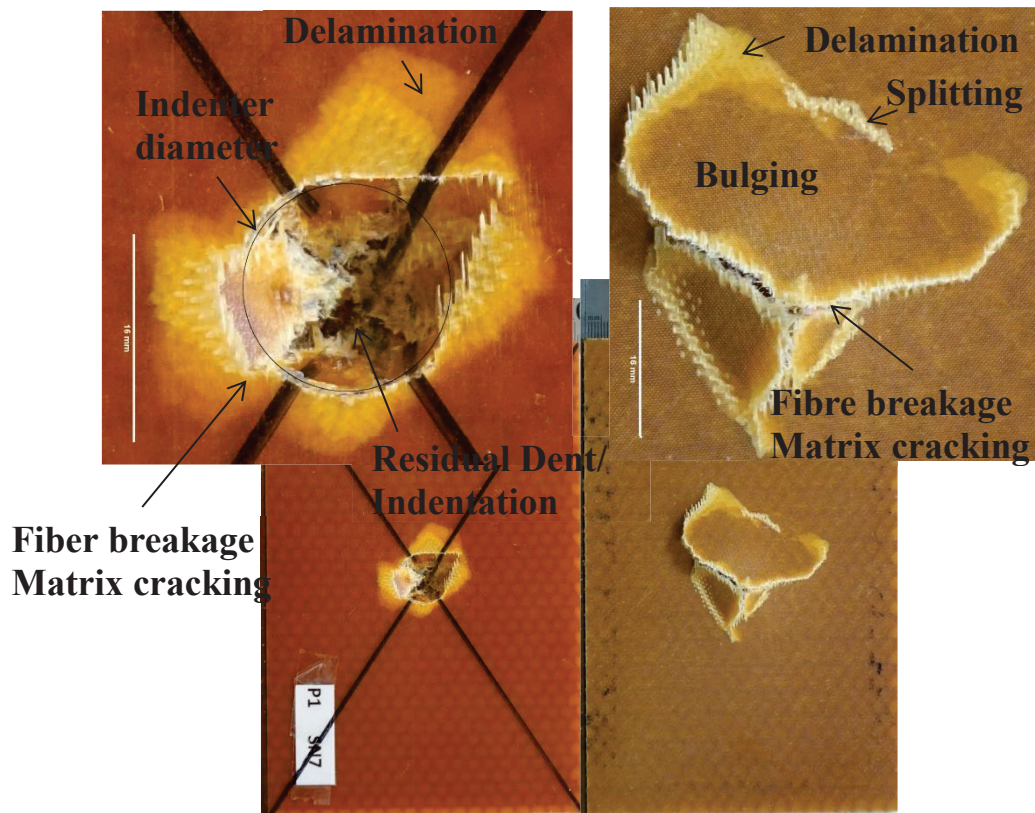
Figure 3.15. Damages on the front and the back face sheets of the sandwich coupons exposed to indentation
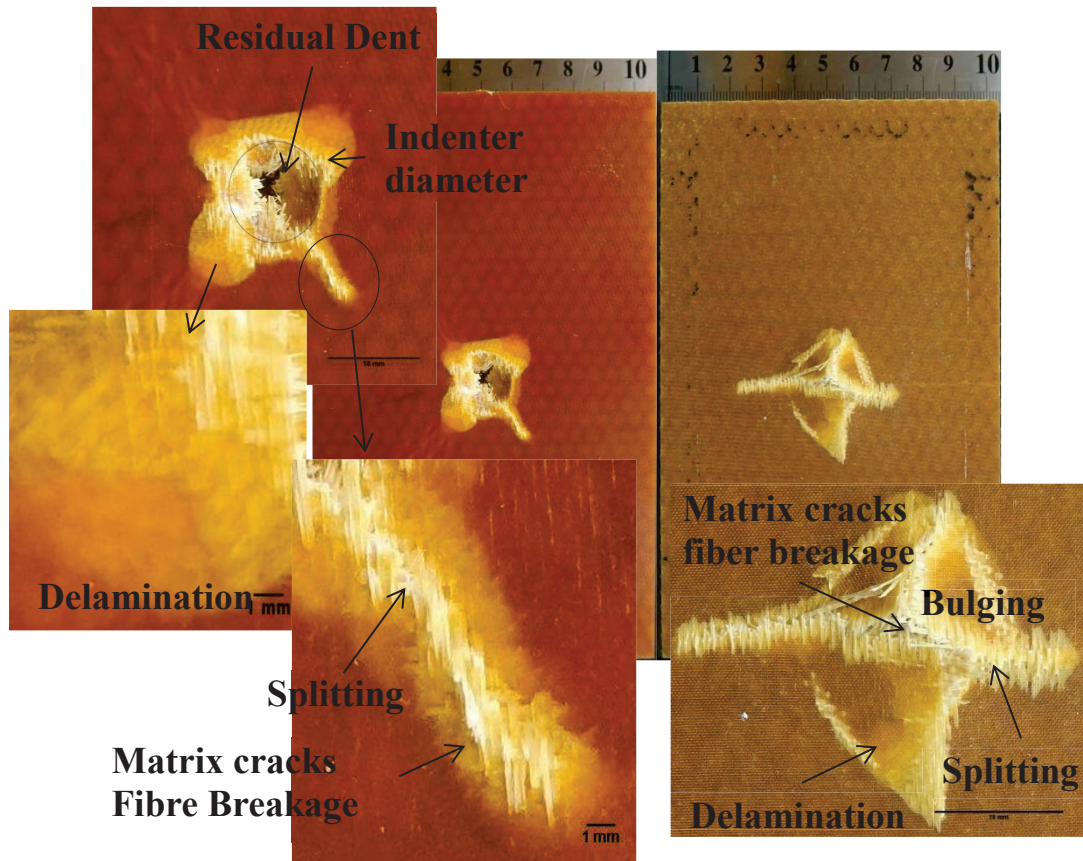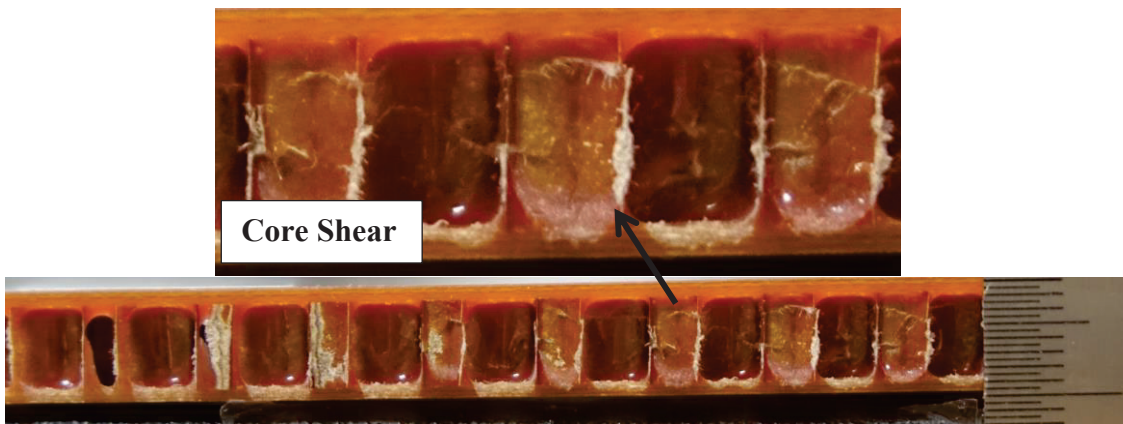
Figure 3.16. (a) Damages of the sandwich coupon presented to the full-penetration with 67 J and (b) the core shear through the length

The damages modes of the coupons are tabulated in Table 3.2. The front face sheet dominant damage mode is determined to be the combined large cracks with fiber breakage and indentation. The back face sheets have depression until 39 J, after which the fiber splitting and cracking occurs. The dominant damage mode of the back face sheet is the

splits/cracks and local depression. High-velocity impact events generate smaller planar damage area and residual depth, as shown in Figure 3.17c. As impact velocity increased, the damage area is localized. This is caused by the laminate face sheet strain rate sensitivity deformation behavior.

Table 3.2. The damage modes of coupons

Impact Energy	#	Damage Mode	
		Front Face Sheet	Back Face Sheet
Indentation		Combined large cracks with fiber breakage, indentation	Split Cracks/Delamination
2.8 J	All	Dent/Depression	-
5.5 J	All	Dent/Depression	-
11 J	DW and 19.40 ms^{-1}	Combined large cracks with fiber breakage, indentation	Depression
	29.41 ms^{-1}	Splits/Cracks	-
22.5 J	All	Combined large cracks with fiber breakage, indentation	Depression
33.5 J	All	Combined large cracks with fiber breakage, indentation	Depression
39 J	All	Combined large cracks with fiber breakage, indentation	Splits/Cracks
44.5 J	Test 01 Test 02	Combined large cracks with fiber breakage, indentation	Splits/Cracks
	Test 03	Combined large cracks with fiber breakage, indentation	Depression
56 J	Test 01	Combined large cracks with fiber breakage, indentation	Combined large cracks/ splits with fibre breakage
	Test 02 Test 03	Combined large cracks with fiber breakage, indentation	Depression
67 J	Test 01 Test 02	Combined large cracks with fiber breakage, indentation	Splits/Cracks
	Test 03	Combined large cracks with fiber breakage, indentation	Combined large cracks with fibre breakage, bulging, splits

(a)　　　　　　　　(b)　　　　　　　　(c)
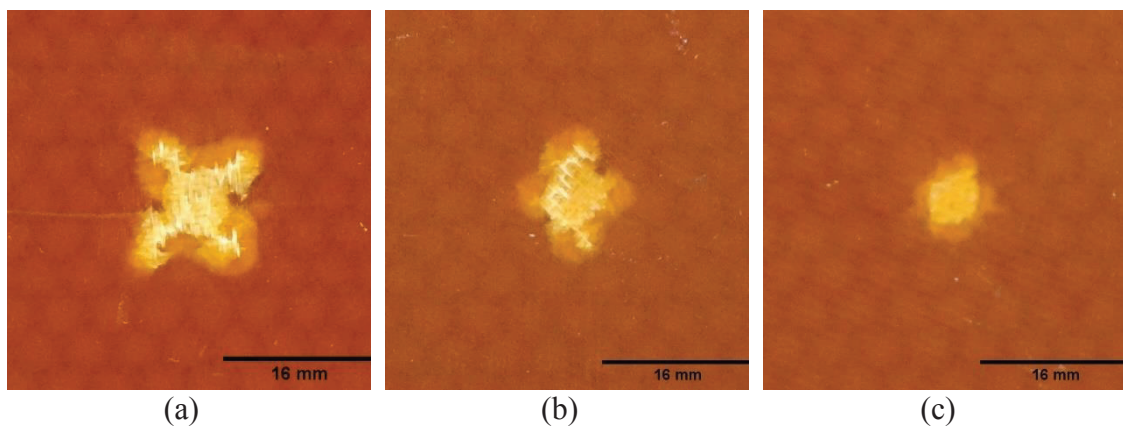
Figure 3.17. The front face sheets of the coupons subjected to 11 J under variety velocity impact (a) 2 ms^{-1} (b) 20 ms^{-1}, and (c) 30 ms^{-1}

The NRS versus planar damage area curve of the tested coupons is shown in Figure 3.18. The curve can be divided into three regions, as depicted in the same figure. The first region consists of residual depths smaller than 1 mm. Here, NRS is about 0.8, and planar damage is approximately 50 mm^2. Thus, the region is called BVID. The damage area between 50-400 m^2 is identified as the VID range where the perforation occurs in the front face sheet. In this region, the structure may need to be repaired due to catastrophic destruction. The damage area between 400 and 800 m^2 where full-penetration and core shear generate occur is categorized as discrete source damage. The structure with this damage may need to be replaced or repaired immediately.
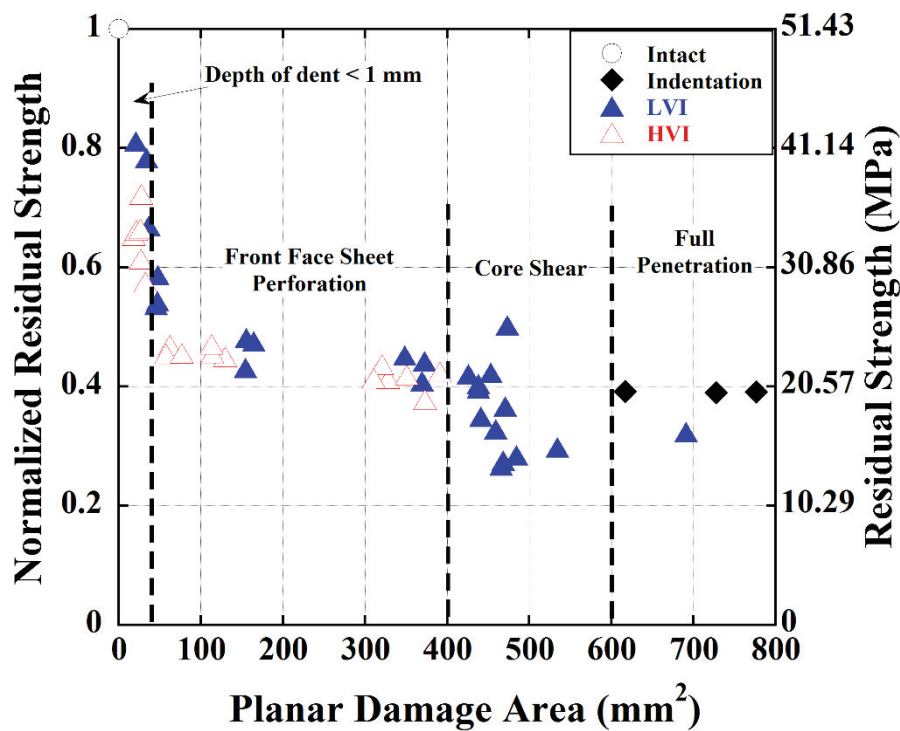
Figure 3.18. NRS versus Planar Damage Area

Figure 3.19 represents the potential failure modes of a sandwich structure subjected to CAI tests. The failure modes occur mainly at the upper or lower of the center of the coupons since the non-uniform distribution of load at the upper or lower center results in load concentration[32]. Face wrinkling failure is caused by the compressive modulus of the facing skin and/or the core compression strength not being high enough. Panel buckling and shear crimping occur when the core thickness and/or shear modulus

are not enough. In face dimpling, the core cell size is not small enough for the chosen face sheet[10]. The damage modes of the tested intact sandwich coupons are the fiber splitting, matrix cracking and core shear in the buckling zone, and face sheet/core debonding took place at the center of coupons, as shown in Figure 3.20. The splits/cracks propagate from both edges to center. This may be because of the face wrinkling, core shear, and edge effect. The local buckling occurs in the center of the coupons due to damage area between 2.8 and 33.5 J, as shown in Figure 3.21. The splits/cracks propagate from two sides or one side to impact damage area. Since the sandwich coupons had face sheet/core debonding and the global core shear, general buckling occurred between 44.5 and 67 J, as shown in Figure 3.22. And the splits/cracks initiated at the load side, and the splits/cracks move to the impact damage area.
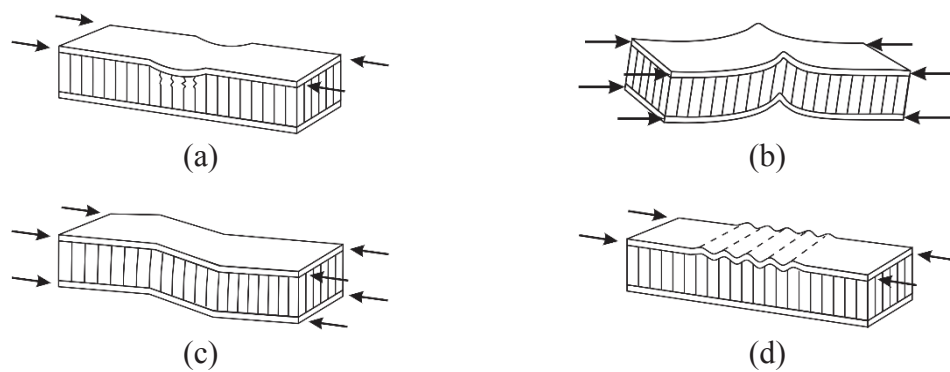
Figure 3.19. (a) Face wrinkling[10], (b) panel buckling[10], (c) shear crimping[10], and (d) face dimpling (intra cell buckling)[10]

Front Face Sheet   Back Face Sheet

Face sheet/core
debonding

Splits, cracks, and
fiber breakage

Buckling

Delamination

Buckling zone

Splits, cracks, fiber breakage
and delamination

Intact Coupon Test 02
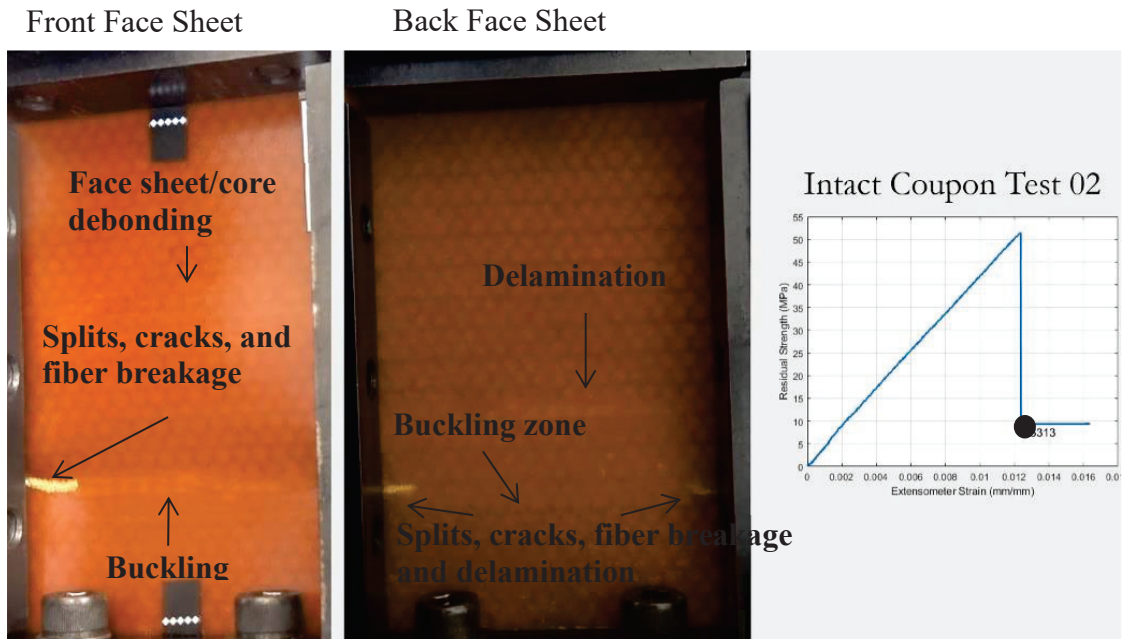
Figure 3.20. Failure moment of an intact coupon during CAI testing

33.49 J Test 01
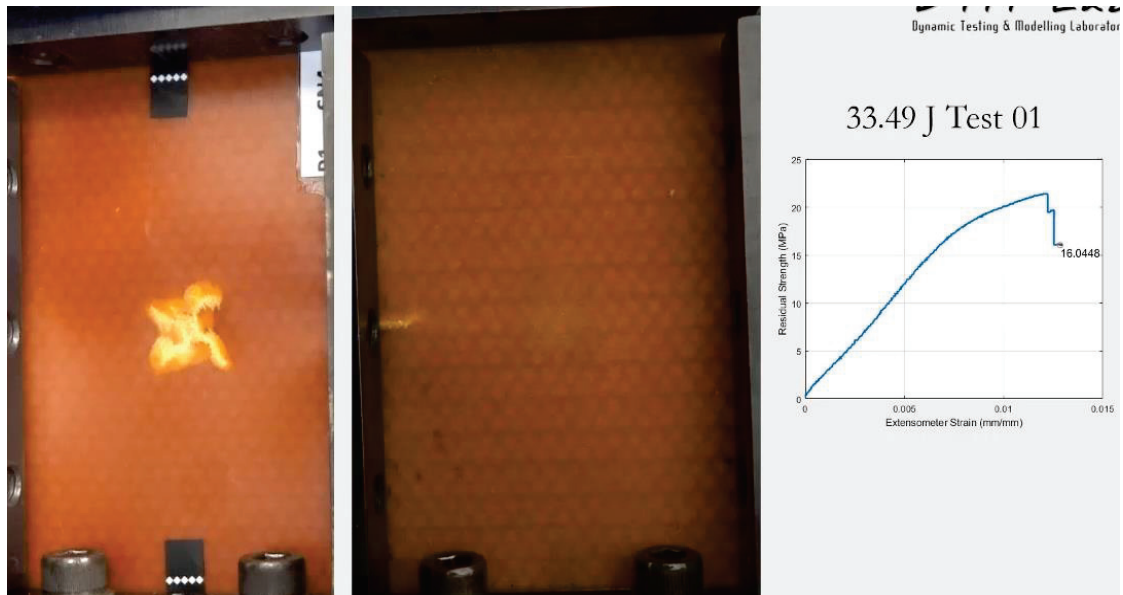
Figure 3.21. The CAI test of the a coupon subjected to 33.5 J
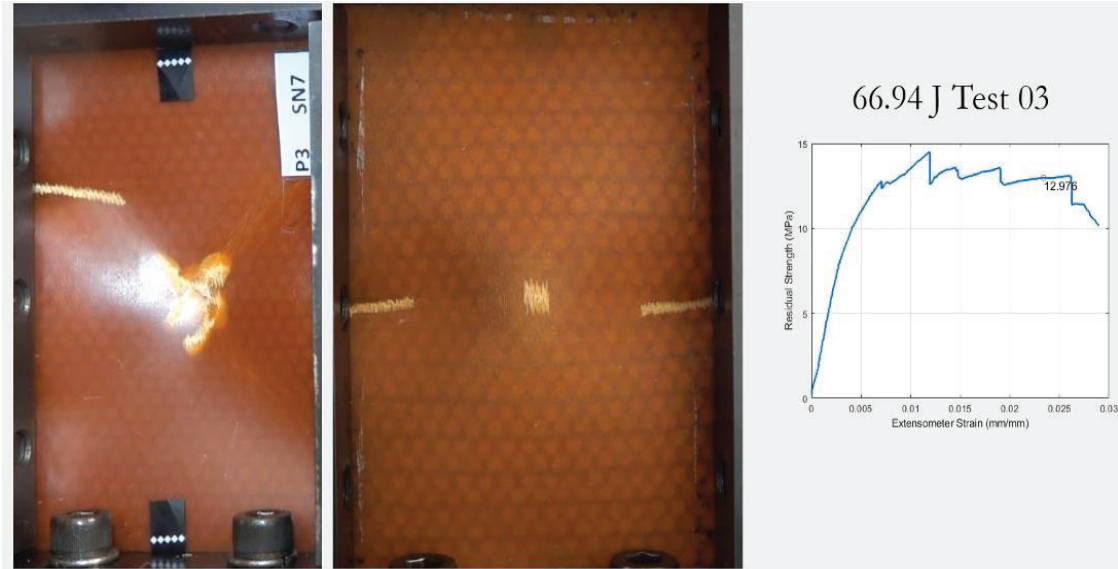
Figure 3.22. The CAI test of the a coupon subjected to 67 J

3.7. Effect of Velocity

The variations of F_1 and F_{max} with velocity and E_1 and E_{max} with impact energy are shown in Figures 3.23a and b, respectively. The effect of strain rate or velocity on the strength values of composites is usually expressed by a logarithmic relation between strength and strain rate (or velocity) as [86]

$$\sigma(\dot{\varepsilon}) = \sigma(\dot{\varepsilon}_o)[1 + cln\left(\frac{\dot{\varepsilon}}{\dot{\varepsilon}_o}\right)] \tag{3.1}$$

where, $\sigma(\dot{\varepsilon})$ is the strength at the strain rate of $\dot{\varepsilon}$, $\dot{\varepsilon}_o$ is the reference strain rate, $\sigma(\dot{\varepsilon}_o)$ is the strength at the reference strain rate, and c is the strain rate sensitivity parameter. The F_1 and F_{max} values are fitted with Eqn. 3.1 as function velocity and the fitted c parameters are shown in Figure 3.23a. The determined c values in Figure 3.23a, 0.034 and 0.021, are very much comparable with the ones reported for similar Glass fiber/epoxy composites, 0.02[87] and 0.03[88]. The E_1 and E_{max} values also show similar logarithmic relations with the impact energy, as shown in Figure 3.23b.

On the other side, cellular materials, including honeycombs, show a strain rate dependent crushing stress which may have an effect on the impact response of the studied sandwich coupons. The rate sensitivity of the studied core may be due to strain rate

sensitivity of cell wall material and micro-inertia[89, 90]. The effect of strain rate sensitivity of the cell wall material on the dynamic crushing stress was numerically shown negligible for low-density structures[91, 92], which is also valid for the studied Nomex core (48 kgm^{-3}). First shown by Calladine and English[93], the structures deforming through bending mode under compressive loads exhibit velocity-dependent bending stress, known as inertia. Micro-inertia is effective in cellular structures when the cells are collectively deformed by a mechanism known as cell-wall bending (folding). The increased deformation forces of aluminum honeycombs [94], foams [95] and corrugated cores [96-98] were reported due to micro-inertia. The micro-inertia based stress increment ($\Delta\sigma_{cr}$) with increasing velocity (v) is estimated using the following relation [99]

$$\Delta\sigma_{cr} = \frac{\rho_o}{\varepsilon_d} v^2$$

(3.2)

where, ρ_o and ε_d are the density and densification strain, respectively.
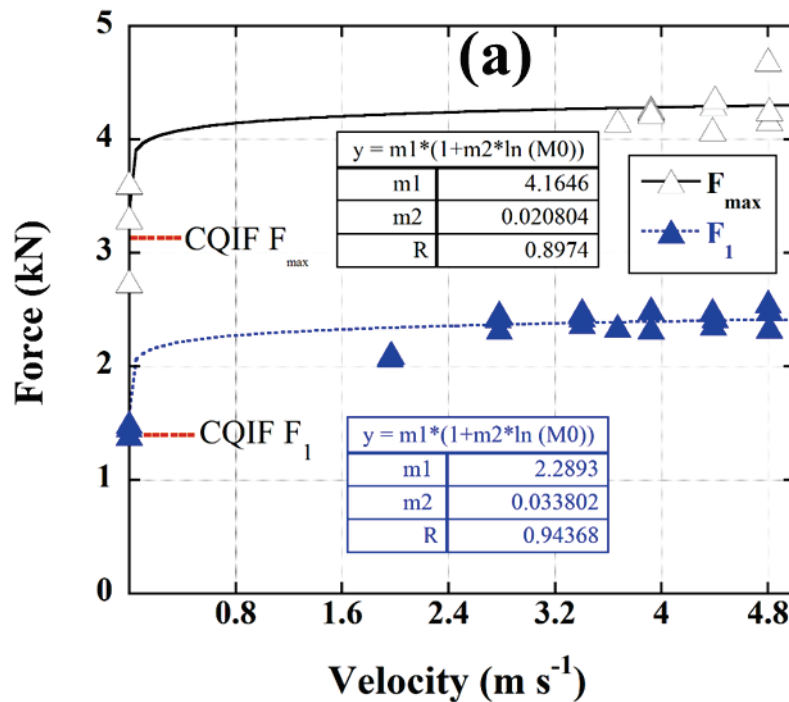
Figure 3.23. The variations of (a) F_1 and F_{max} with velocity and (b) E_1 and E_{max} with impact energy

(cont. on next page)
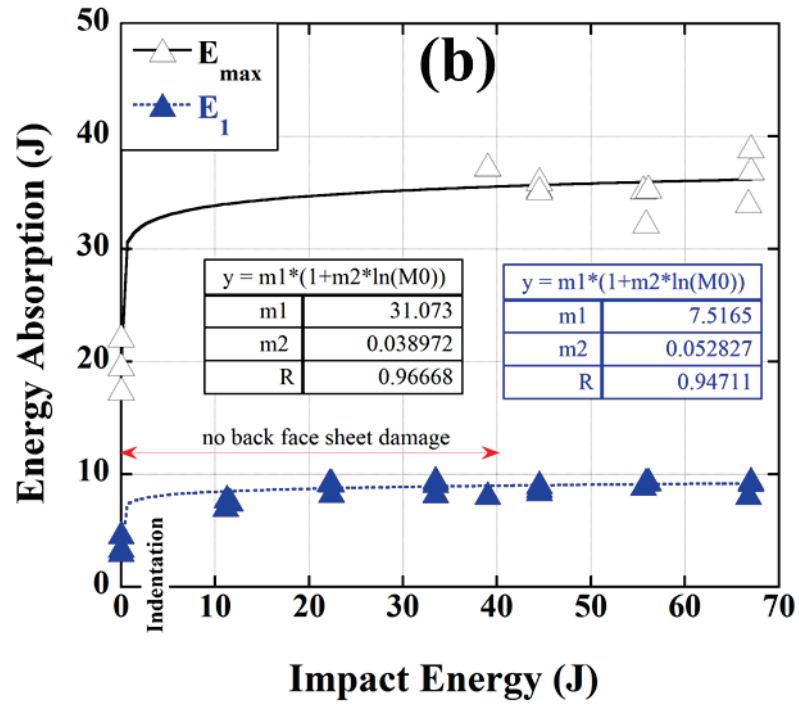
(b)

Figure 3.23. (cont.)

The stress increment of the studied core is calculated ~0.4% at 10 ms^{-1}, ~5% at 40 ms^{-1} and ~31% at 100 ms^{-1} by taking crushing stress of 2.2 MPa, a density of 48 kgm^{-1} and a densification strain of 0.7. These calculations reveal a negligible contribution of the core crushing to increased impact forces of the studies coupons in the LVI tests, as well as in the HVI tests. The inertial effect may, however, be effective when the impact velocity is much over 40 ms^{-1}. Therefore, the detected increase in the impact loads and the logarithmic relation between absorbed energy and impact energy are merely due to the increased fracture strength of composite face sheets at increasing impact velocities in the LVI tests.

CHAPTER 4

CONCLUSION

The quasi-static indentation, low-velocity impact and high-velocity impact response, and damage tolerances of an E-glass fiber (7781GL) reinforced epoxy face-sheets, and the Nomex honeycomb core sandwich was determined experimentally. The composite face sheets had a layup of $(0/45/90/-45)_s$ with a thickness of 0.88 mm. The hexagonal cell honeycomb core was made of phenolic resin-impregnated aramid paper Nomex with a core depth of 6 mm, the cell wall thickness of 0.1 mm, cell diameter of 5 mm and a density of 48 kg m^{-3}. The quasi-static indentation, low-velocity impact and high-velocity impact tests were performed sequentially using a universal test machine, a Drop-weight tester and a modified Split-Hopkinson Pressure Bar (SHPB) test system using the same indenter/impactor, a 16 mm-hemispherical tip indenter. The quasi-static indentation and low-velocity impact tests were in accord with the ASTM D6264 / D6264M - 17: *Standard Test Method for Measuring the Damage Resistance of a Fiber-Reinforced Polymer-Matrix Composite to a Concentrated Quasi-Static Indentation Force* and the ASTM D7136 / D7136M - 20: *Standard Test Method for Measuring the Damage Resistance of a Fiber-Reinforced Polymer Matrix Composite to a Drop-Weight Impact Event*, respectively. The damage in the sandwiches was determined by following the ASTM D7766 / D7766M - 16: *Standard practice for damage resistance testing of sandwich constructions*. The damage tolerances of the tested coupons were through the Compressive After Impact (CAI) residual strength after face-on impact based on the ASTM D7137 / D7137M - 17: *Standard Test Method for Compressive Residual Strength Properties of Damaged Polymer Matrix Composite Plates.* In the high-velocity impact tests, the impactor inserted inside the gas gun barrel of the SHPB and fired axially to the sandwich coupons. high-velocity impact tests were performed at the same energy levels with the low-velocity impact tests but at higher velocities between 20-40 ms^{-1}.

In the quasi-static indentation tests, the damage on the front face sheet started at 3.5-45 J and completely penetrated by the intender at 18-22.5 J. Typical damage formed at the front and back face sheet included fiber and matric fracture and delamination. In LVI tests, the front face sheet damage started at 7.5-10 J and completely penetrated at

32.5-39 J with the same damage modes of the front and back face sheet with the quasi-static indentation tests. The increased impact forces and energy absorptions of low-velocity impact test coupons were ascribed to the strain rate sensitivity of the composite face sheet. In accord with this, the fully penetrated quasi-static indentation test sandwiches showed higher CAI strength values than the fully-penetrated LVI test sandwiches. A comparison of the CAI stress-strain curves of the low-velocity impact and high-velocity impact tested sandwiches coupons at similar impact energy levels showed that the impact velocity was not significantly affected the CAI strength values of the tested coupons, except the high-velocity impact tested coupon showed a slightly higher mean CAI strength at 5.5 J. But at increasing impact energies, both low-velocity impact and high-velocity impact tests resulted in almost similar CAI strength values with the studied velocity range.

Two characteristics of energy levels were further identified in the residual strength-impact energy behavior of the tested sandwiches. Until about the front face sheet started to be penetrated by the impactor at about 10 J, a catastrophic reduction of 60% occurred in the residual strength. Second, above 44.5 J, the flexural waves became dominant, and a global core shear was observed. For the tested sandwiches, barely visible impact damage (BVID) was identified below about 10 J with a depth of dent was less than 1 mm, the damage area was less than 50 mm^2 and an normalized residual strength (NRS) value was about 0.8. The damage area between 50-400 mm^2 was identified as the visible impact damage (VID) range where the front face sheet perforation occurred between 10-39 J. The damage area between 400 and 800 mm^2 was categorized as discrete source damage where the full-penetration and core shear of the coupons occurred above about 40 J.

REFERENCES

1.   Statistical pocketbook. 4.11.2020 ed.; Directorate-General for Mobility and Transport, Publications Office of the European Union. https://op.europa.eu/en/publication-detail/-/publication/da0cd68e-1fdd-11eb-b57e-01aa75ed71a1/language-en/format-PDF/source-search (accessed 21.3.2021).

2.   Zinno, A.; Prota, A.; Di Maio, E.; Bakis, C. E., Experimental characterization of phenolic-impregnated honeycomb sandwich structures for transportation vehicles. Compos. Struct. 2011, 93 (11), 2910-2924.

3.   Ashby, M. F., Chapter 4 - Material Property Charts. In Materials Selection in Mechanical Design (Fourth Edition), Ashby, M. F., Ed. Butterworth-Heinemann: Oxford, 2011; pp 57-96.

4.   Ahmad, S.; Zhang, J.; Feng, P.; Yu, D.; Wu, Z.; Ke, M., Processing technologies for Nomex honeycomb composites (NHCs): A critical review. Compos. Struct. 2020, 250, 112545.

5.   Wang, R.-M.; Zheng, S.-R.; Zheng, Y.-P., 10 - High frequency dielectric properties of composites and radome. In Polymer Matrix Composites and Technology, Wang, R.-M.; Zheng, S.-R.; Zheng, Y.-P., Eds. Woodhead Publishing: 2011; pp 487-548.

6.   Ashby, M. F., Materials Selection in Mechanical Design. Elsevier Ltd: 2011.
7.   ASTM D7136 / D7136M - 20, Standard Test Method for Measuring the Damage Resistance of a Fiber-Reinforced Polymer Matrix Composite to a Drop-Weight Impact Event. ASTM International, West Conshohocken, PA, 2020, www.astm.org.

8.   Ashby, M. F., Chapter 6 - Case Studies: Materials Selection. In Materials Selection in Mechanical Design (Fourth Edition), Ashby, M. F., Ed. Butterworth-Heinemann: Oxford, 2011; pp 125-195.

9.   Bitzer, T., Sandwich design. In Honeycomb Technology: Materials, Design, Manufacturing, Applications and Testing, Springer Netherlands: Dordrecht, 1997; pp 43-69.

10.   Hexcel, C. HexWeb TM Honeycomb Sandwich Design Technology 2004. https://www.hexcel.com/user_area/content_media/raw/Honeycomb_Sandwich_Design_Technology.pdf.

11.   Carlsson, L. A.; Kardomateas, G. A., Introduction. In Structural and Failure Mechanics of Sandwich Composites, Springer Netherlands: Dordrecht, 2011; pp 1-17.

12.   Carlsson, L. A.; Kardomateas, G. A., Structural and Failure Mechanics of Sandwich Composites. Springer Netherlands: Dordrecht, 2011.

13.   Wang, Z., Recent advances in novel metallic honeycomb structure. Composites Part B: Engineering 2019, 166, 731-741.

14.   Bitzer, T., Introduction. In Honeycomb Technology: Materials, Design, Manufacturing, Applications and Testing, Springer Netherlands: Dordrecht, 1997; pp 1-9.

15.   Gibson, L. J.; Ashby, M. F., Cellular solids: structure and properties. Cambridge university press: 1999.

16.   Foo, C. C.; Chai, G. B.; Seah, L. K., Mechanical properties of Nomex material and Nomex honeycomb structure. Compos. Struct. 2007, 80 (4), 588-594.

17.   Karakoç, A.; Freund, J., Experimental studies on mechanical properties of cellular structures using Nomex® honeycomb cores. Compos. Struct. 2012, 94 (6), 2017-2024.

18.   Roy, R.; Park, S.-J.; Kweon, J.-H.; Choi, J.-H., Characterization of Nomex honeycomb core constituent material mechanical properties. Compos. Struct. 2014, 117, 255-266.

19.   Xie, S.; Feng, Z.; Zhou, H.; Wang, D.; Ma, W., In-plane and out-of-plane compressive mechanical properties of Nomex honeycombs and their prediction. Journal of the Brazilian Society of Mechanical Sciences and Engineering 2020, 42 (9), 460.

20.   Liu, L.; Meng, P.; Wang, H.; Guan, Z., The flatwise compressive properties of Nomex honeycomb core with debonding imperfections in the double cell wall. Composites Part B: Engineering 2015, 76, 122-132.

21.   Liu, L.; Wang, H.; Guan, Z., Experimental and numerical study on the mechanical response of Nomex honeycomb core under transverse loading. Compos. Struct. 2015, 121, 304-314.

22.   Zhou, Z.; Wang, Z.; Zhao, L.; Shu, X., Experimental investigation on the yield behavior of Nomex honeycombs under combined shear-compression. Latin American Journal of Solids and Structures 2012, 9, 515-530.

23.   Zhang, Y. W.; Liu, T.; Tizani, W., Experimental and numerical analysis of dynamic compressive response of Nomex honeycombs. Compos. Pt. B-Eng. 2018, 148, 27-39.

24.   Rodriguez-Ramirez, J. d. D.; Castanie, B.; Bouvet, C., Experimental and numerical analysis of the shear nonlinear behaviour of Nomex honeycomb core: Application to insert sizing. Compos. Struct. 2018, 193, 121-139.

25.   Bitzer, T., Honeycomb processes. In Honeycomb Technology: Materials, Design, Manufacturing, Applications and Testing, Springer Netherlands: Dordrecht, 1997; pp 70-79.

26.   Scherble, J.; Jahn, T. In New Rohacellê Development For Resin Infusion Processes, Dordrecht, Springer Netherlands: Dordrecht, 2005; pp 753-761.

27.   Rapp, R. A.; Ackermann, J. F.; Gleason, G. R.; Tanino, K. M., Composite panel and method of manufacturing the same. Google Patents: 2015.

28.   Xue, X.; Zhang, C.; Chen, W.; Wu, M.; Zhao, J., Study on the impact resistance of honeycomb sandwich structures under low-velocity/heavy mass. Compos. Struct. 2019, 226, 111223.

29.   Olsson, R., Methodology for predicting the residual strength of impacted sandwich panels. FFA TN 1999, 8.

30.   Vijaya Ramnath, B.; Alagarraja, K.; Elanchezhian, C., Review on Sandwich Composite and their Applications. Materials Today: Proceedings 2019, 16, 859-864.

31.   He, W.; Yao, L.; Meng, X.; Sun, G.; Xie, D.; Liu, J., Effect of structural parameters on low-velocity impact behavior of aluminum honeycomb sandwich structures with CFRP face sheets. Thin-Walled Structures 2019, 137, 411-432.

32.   Bai, R. X.; Guo, J. J.; Lei, Z. K.; Liu, D.; Ma, Y.; Yan, C., Compression after impact behavior of composite foam-core sandwich panels. Compos. Struct. 2019, 225.

33.   Aryal, B.; Morozov, E. V.; Wang, H.; Shankar, K.; Hazell, P. J.; Escobedo-Diaz, J. P., Effects of impact energy, velocity, and impactor mass on the damage induced in composite laminates and sandwich panels. Compos. Struct. 2019, 226, 111284.

34.   Zhang, T. T.; Yan, Y.; Li, J. F., Experiments and numerical simulations of low-velocity impact of sandwich composite panels. Polym. Compos. 2017, 38 (4), 646-656.

35.   Zhang, D.; Fei, Q.; Zhang, P., Drop-weight impact behavior of honeycomb sandwich panels under a spherical impactor. Compos. Struct. 2017, 168, 633-645.

36.   Suresh Kumar, C.; Arumugam, V.; Santulli, C., Characterization of indentation damage resistance of hybrid composite laminates using acoustic emission monitoring. Composites Part B: Engineering 2017, 111, 165-178.

37.   ASTM D6264 / D6264M - 17, Standard Test Method for Measuring the Damage Resistance of a Fiber-Reinforced Polymer-Matrix Composite to a Concentrated Quasi-Static Indentation Force. ASTM International, West Conshohocken, PA, 2017, www.astm.org.

38.   ASTM D7766 / D7766M - 16, Standard Practice for Damage Resistance Testing of Sandwich Constructions. ASTM International, West Conshohocken, PA, 2016, www.astm.org.

39.   ASTM D7137 / D7137M - 17, Standard Test Method for Compressive Residual Strength Properties of Damaged Polymer Matrix Composite Plates. ASTM International, West Conshohocken, PA, 2017, www.astm.org.

40.   ASTM D6641 / D6641M - 16e2, Standard Test Method for Compressive Properties of Polymer Matrix Composite Materials Using a Combined Loading Compression (CLC) Test Fixture. ASTM International, West Conshohocken, PA, 2016, www.astm.org.

41.   Shah, S. Z. H.; Karuppanan, S.; Megat-Yusoff, P. S. M.; Sajid, Z., Impact resistance and damage tolerance of fiber reinforced composites. Compos. Struct. 2019, 217, 100-121.

42.   Composite Materials, H., Composite Materials Handbook, Volume 3 - Polymer Matrix Composites - Materials Usage, Design, and Analysis. SAE International on behalf of CMH-17, a division of Wichita State University: 2015.

43.   Gao, S.-L.; Kim, J.-K., Cooling rate influences in carbon fibre/PEEK composites. Part III: impact damage performance. Composites Part A: Applied Science and Manufacturing 2001, 32 (6), 775-785.

44.   Vieille, B.; Casado, V. M.; Bouvet, C., Influence of matrix toughness and ductility on the compression-after-impact behavior of woven-ply thermoplastic- and thermosetting-composites: A comparative study. Compos. Struct. 2014, 110, 207-218.

45.   Tan, K. T.; Watanabe, N.; Iwahori, Y., Impact Damage Resistance, Response, and Mechanisms of Laminated Composites Reinforced by Through-Thickness Stitching. International Journal of Damage Mechanics 2012, 21 (1), 51-80.

46.   Chen, F.; Hodgkinson, J. M., Impact behaviour of composites with different fibre architecture. Proceedings of the Institution of Mechanical Engineers, Part G: Journal of Aerospace Engineering 2009, 223 (7), 1009-1017.

47.   Seltzer, R.; González, C.; Muñoz, R.; Llorca, J.; Blanco-Varela, T., X-ray microtomography analysis of the damage micromechanisms in 3D woven composites

under low-velocity impact. Composites Part A: Applied Science and Manufacturing 2013, 45, 49-60.

48.   Bandaru, A. K.; Sachan, Y.; Ahmad, S.; Alagirusamy, R.; Bhatnagar, N., On the mechanical response of 2D plain woven and 3D angle-interlock fabrics. 2017.

49.   Sanchez-Saez, S.; Barbero, E.; Zaera, R.; Navarro, C., Compression after impact of thin composite laminates. Compos. Sci. Technol. 2005, 65 (13), 1911-1919.

50.   Singh, K. K.; Singh, N. K.; Jha, R., Analysis of symmetric and asymmetric glass fiber reinforced plastic laminates subjected to low-velocity impact. J. Compos Mater. 2016, 50 (14), 1853-1863.

51.   Choi, H. Y.; Wang, H. S.; Chang, F.-K., Effect of Laminate Configuration and Impactor's Mass on the Initial Impact Damage of Graphite/Epoxy Composite Plates Due to Line-Loading Impact. J. Compos Mater. 1992, 26 (6), 804-827.

52.   Olsson, R., Mass criterion for wave controlled impact response of composite plates. Composites Part A: Applied Science and Manufacturing 2000, 31 (8), 879-887.

53.   Cantwell, W. J.; Morton, J., Comparison of the low and high velocity impact response of cfrp. Composites 1989, 20 (6), 545-551.

54.   Kim, C. G.; Jun, E. J., Impact Resistance of Composite Laminated Sandwich Plates. 1992, 26 (15), 2247-2261.

55.   Minguet, P. J.; Amer Inst, A.; Astronaut, A Model For Predicting The Behavior Of Impact-Damaged Minimum Gauge Sandwich Panels Under Compression. Amer Inst Aeronautics & Astronautics: Washington, 1991; p 1112-1122.

56.   Bernard, M. L.; Lagace, P. A., Impact Resistance of Composite Sandwich Plates. 1989, 8 (5), 432-445.

57.   Aminanda, Y.; Castanie, B.; Barrau, J. J.; Thevenet, P., Experimental and numerical study of compression after impact of sandwich structures with metallic skins. Compos. Sci. Technol. 2009, 69 (1), 50-59.

58.   Wang, H.; Ramakrishnan, K. R.; Shankar, K., Experimental study of the medium velocity impact response of sandwich panels with different cores. Materials & Design 2016, 99, 68-82.

59.   Xie, S.; Jing, K.; Zhou, H.; Liu, X., Mechanical properties of Nomex honeycomb sandwich panels under dynamic impact. Compos. Struct. 2020, 235, 111814.

60.   Chen, Y.; Hou, S. J.; Fu, K. K.; Han, X.; Ye, L., Low-velocity impact response of composite sandwich structures: Modelling and experiment. Compos. Struct. 2017, 168, 322-334.

61.   Zhang, T. T.; Yan, Y.; Li, J. F.; Luo, H. B., Low-velocity impact of honeycomb sandwich composite plates. J. Reinf. Plast. Compos. 2016, 35 (1), 8-32.

62.   Hasseldine, B. P. J.; Zehnder, A. T.; Keating, B. D.; Singh, A. K.; Davidson, B. D., Compressive strength of aluminum honeycomb core sandwich panels with thick carbon-epoxy facesheets subjected to barely visible indentation damage. J. Compos Mater. 2016, 50 (3), 387-402.

63.   Yang, B.; Wang, Z. Q.; Zhou, L. M.; Zhang, J. F.; Tong, L. L.; Liang, W. Y., Study on the low-velocity impact response and CAI behavior of foam-filled sandwich panels with hybrid facesheet. Compos. Struct. 2015, 132, 1129-1140.

64.   Wang, J.; Chen, B. X.; Wang, H.; Waas, A. M., Experimental study on the compression-after-impact behavior of foam-core sandwich panels. J. Sandw. Struct. Mater. 2015, 17 (4), 446-465.

65.   James, C. T.; Cunningham, P. R.; Watson, A., Experimental and numerical investigation of the effect of asymmetry on the residual strength of a composite sandwich panel. J. Sandw. Struct. Mater. 2015, 17 (4), 417-445.

66.   Ivañez, I.; Moure, M. M.; Garcia-Castillo, S. K.; Sanchez-Saez, S., The oblique impact response of composite sandwich plates. Compos. Struct. 2015, 133, 1127-1136.

67.   Akatay, A.; Bora, M. O.; Coban, O.; Fidan, S.; Tuna, V., The influence of low velocity repeated impacts on residual compressive properties of honeycomb sandwich structures. Compos. Struct. 2015, 125, 425-433.

68.   McQuigg, T. D.; Kapania, R. K.; Scotti, S. J.; Walker, S. P., Compression After Impact Experiments on Thin Face Sheet Honeycomb Core Sandwich Panels. J. Spacecr. Rockets 2014, 51 (1), 253-266.

69.   Gordon, S.; Boukhili, R.; Merah, N., Impact behavior and finite element prediction of the compression after impact strength of foam/vinylester-glass composite sandwiches. J. Sandw. Struct. Mater. 2014, 16 (5), 551-574.

70.   Gilioli, A.; Sbarufatti, C.; Manes, A.; Giglio, M., Compression after impact test (CAI) on NOMEX (TM) honeycomb sandwich panels with thin aluminum skins. Compos. Pt. B-Eng. 2014, 67, 313-325.

71.   Czabaj, M. W.; Zehnder, A. T.; Davidson, B. D.; Singh, A. K., Compressive strength of honeycomb-stiffened graphite/epoxy sandwich panels with barely-visible indentation damage. J. Compos Mater. 2014, 48 (20), 2455-2471.

72.   Zhang, G. Q.; Wang, B.; Ma, L.; Xiong, J.; Yang, J. S.; Wu, L. Z., The residual compressive strength of impact-damaged sandwich structures with pyramidal truss cores. Compos. Struct. 2013, 105, 188-198.

73.   Nettles, A., Normalizing impact energy by face sheet thickness for composite sandwich structure compression after impact testing. J. Sandw. Struct. Mater. 2013, 15 (3), 340-358.

74.   Feng, D.; Aymerich, F., Damage prediction in composite sandwich panels subjected to low-velocity impact. Composites Part A: Applied Science and Manufacturing 2013, 52, 12-22.

75.   Cho, J. U.; Choi, H. K.; Lee, S.; Cho, C.; Han, M. S., Experimental study of the impact characteristics of sandwich composites with aluminum honeycomb cores. Int. J. Automot. Technol. 2013, 14 (3), 415-421.

76.   Tan, C. Y.; Akil, H. M., Impact response of fiber metal laminate sandwich composite structure with polypropylene honeycomb core. Composites Part B: Engineering 2012, 43 (3), 1433-1438.

77.   Ma, J.; Yan, Y.; Liu, Y. J.; Yang, L., Compression strength of stitched foam-core sandwich composites with impact induced damage. J. Reinf. Plast. Compos. 2012, 31 (18), 1236-1246.

78.   Klaus, M.; Reimerdes, H. G.; Gupta, N. K., Experimental and numerical investigations of residual strength after impact of sandwich panels. Int. J. Impact Eng. 2012, 44, 50-58.

79.   Zhu, S.; Chai, G. B., Effect of adhesive in sandwich panels subjected to low-velocity impact. Proceedings of the Institution of Mechanical Engineers, Part L: Journal of Materials: Design and Applications 2011, 225 (3), 171-181.

80.   Sawal, N.; Akil, H. M., Effect of Core Thicknesses on Impact Performance of Thermoplastic Honeycomb Core Sandwich Structure Under Low-Velocity Impact Loading. Key Eng Mater 2011, 471-472, 461-465.

81.   ASTM, D7136/D7136M − 15 Standard Test Method for Measuring the Damage Resistance of a Fiber-Reinforced Polymer Matrix Composite to a Drop-Weight Impact Event. 2015.

82.   Lin, C.; Fatt, M. S. H., Perforation of Composite Plates and Sandwich Panels under Quasi-static and Projectile Loading. J. Compos Mater. 2006, 40 (20), 1801-1840.

83.   Keshavanarayana, S. R. The static indentation behavior of composite sandwich panels with thin quasi-isotropic skins. 2001.

84.   Raju, K. S.; Smith, B. L.; Tomblin, J. S.; Liew, K. H.; Guarddon, J. C., Impact Damage Resistance and Tolerance of Honeycomb Core Sandwich Panels. J. Compos Mater. 2008, 42 (4), 385-412.

85.   Chai, G. B.; Zhu, S., A review of low-velocity impact on sandwich structures. Proceedings of the Institution of Mechanical Engineers, Part L: Journal of Materials: Design and Applications 2011, 225 (4), 207-230.

86.   Meyers, A. M., Dynamic Behavior of Materials. John Wiley & Sons, Inc: New York, USA, 1994.

87.   Tasdemirci, A.; Kara, A.; Turan, A. K.; Tunusoglu, G.; Guden, M.; Hall, I. W., Experimental and Numerical Investigation of High Strain Rate Mechanical Behavior of a 0/45/90/-45 Quadriaxial E-Glass/Polyester Composite. In 11th International Conference on the Mechanical Behavior of Materials, Guagliano, M.; Vergani, L., Eds. Elsevier Science Bv: Amsterdam, 2011; Vol. 10, pp 3068-3073.

88.   Gama, B. Z. A progressive composite damage model for unidirectional and woven fabric composites-UD-CCM Updates on MAT162 User Manual Version 17A-2017; University of Delaware Center for Composite Materials: 2017.

89.   Liu, Y. D.; Yu, J. L.; Zheng, Z. J.; Li, J. R., A numerical study on the rate sensitivity of cellular metals. Int. J. Solids Struct. 2009, 46 (22-23), 3988-3998.

90.   Zhao, H.; Elnasri, I.; Li, H. J., The mechanism of strength enhancement under impact loading of cellular materials. Advanced Engineering Materials 2006, 8 (9), 877-883.

91.   Myers, K.; Katona, B.; Cortes, P.; Orbulov, I. N., Quasi-static and high strain rate response of aluminum matrix syntactic foams under compression. Compos. Pt. A-Appl. Sci. Manuf. 2015, 79, 82-91.

92.   Zhang, J.; Zhao, G. P.; Lu, T. J.; He, S. Y., Strain Rate Behavior of Closed-Cell Al-Si-Ti Foams: Experiment and Numerical Modeling. Mech. Adv. Mater. Struct. 2015, 22 (7), 556-563.

93.   Calladine, C. R.; English, R. W., Strain-Rate And Inertia Effects In The Collapse Of 2 Types Of Energy-Absorbing Structure. Int. J. Mech. Sci. 1984, 26 (11-1), 689-&.

94.   Zhao, H.; Elnasri, I.; Abdennadher, S., An experimental study on the behaviour under impact loading of metallic cellular materials. Int. J. Mech. Sci. 2005, 47 (4-5), 757-774.

95.   Paul, A.; Ramamurty, U., Strain rate sensitivity of a closed-cell aluminum foam. Mater. Sci. Eng. A-Struct. Mater. Prop. Microstruct. Process. 2000, 281 (1-2), 1-7.

96.   Guden, M.; Canbaz, I., The effect of cell wall material strain and strain-rate hardening behaviour on the dynamic crush response of an aluminium multi-layered corrugated core. Int. J. Crashworthiness 2021, 26 (1), 38-52.

97.   Sankaya, M.; Tasdemirci, A.; Guden, M., Dynamic crushing behavior of a multilayer thin-walled aluminum corrugated core: The effect of velocity and imperfection. Thin-Walled Structures 2018, 132, 332-349.

98.   Odaci, I. K.; Kilicaslan, C.; Tasdemirci, A.; Guden, M., Projectile impact testing of glass fiber-reinforced composite and layered corrugated aluminium and aluminium foam core sandwich panels: a comparative study. Int. J. Crashworthiness 2012, 17 (5), 508-518.

99.   Reid, S. R.; Peng, C., Dynamic uniaxial crushing of wood. Int. J. Impact Eng. 1997, 19 (5-6), 531-570.